UNIVERSITÀ DEGLI STUDI DI TRIESTE

UNIVERSITÀ DEGLI STUDI DI TRIESTE

XXXIV CICLO DEL DOTTORATO DI RICERCA IN
INGEGNERIA INDUSTRIALE E DELL'INFORMAZIONE

Design and analysis of innovative concentrated windings for SPM machines

Settore scientifico-disciplinare:
ING–IND/32
CONVERTITORI, MACCHINE E AZIONAMENTI ELETTRICI

DOTTORANDO
Cesare Ciriani

COORDINATORE E SUPERVISORE DI TESI
PROF. Alberto Tessarolo

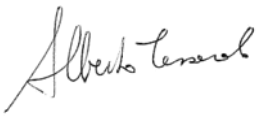

ANNO ACCADEMICO 2020/2021

Contents

Introduction

The use of permanent magnet synchronous machines (PMSMs) is becoming more popular [1] thanks to their compactness, high torque density and increased flux weakening performance [2]. Other advantages can be gained by equipping PMSM with concentrated winding in the stator. In fact, using concentrated winding can be beneficial regarding easy manufacturing and consequently lower production costs, modularity [3] and fault tolerance. More particularly, short end-windings are a strong benefit in terms of copper saving and lead to less joule losses.

However, a well-known drawback of FSCW is the presence of large magneto-motive force space harmonics in the airgap. This harmonic content causes eddy current losses in the permanent magnets placed on the surface of the rotor. For this reason, these magnets can be demagnetized due to overheating [4] [5]. Furthermore, spatial harmonics can decrease the performances of the electrical machines in terms of torque ripple and unbalanced magnetic pull.

Another weakness of concentrated winding is a feasibility rule that imposes a constraint on the design of the machine. As it can be found in the literature [6], some numbers of slots and number of poles combinations are not feasible for the winding to be symmetrical. This limits the degree of freedom of the designer's choices. Furthermore, regardless of the feasibility, the slot-pole combinations are proven to have direct effect on machines performance in various aspects such as winding factor [7] [8], radial forces and vibration behavior [9]-[11], cogging torque [12] [13], flux-weakening capability [14] and leakage inductances [15].

Various provisions have been proposed in the literature to reduce FSCW MMF harmonics such as combined star-delta connections among the coils of a phase and use of multi-phase configurations [22]; the most common and promising countermeasure is, however, the adoption of multi-layer arrangements in which more coils, belonging to different phases, are wound around the same tooth [16], [23]-[29].

A four-layer winding with two identical coils wound on the same tooth is a possible implementation of this arrangement [23]-[25]. It is possible to reduce or even cancel MMF subharmonics by properly assigning phases to tooth coils. However, it has been known since 2004 that using unequal coils with various numbers of turns can produce even better results in a multilayer FSCW [26] [29]. Mostly based on a case-by-case reasoning and through the star-of-slot method [16] it has been proven that suitably selecting the number of turns of the various tooth coils can result in the cancellation of a given MMF harmonic or subharmonic at the expense of a reduction in the MMF fundamental magnitude [27]-[29]. Nevertheless, the question is left unanswered as to whether the proposed solution, identified as "optimal", can be actually further improved through some different arrangement of the tooth coils and a different selection of their number of turns.

One of the goals of this thesis is to prove that, contrary to the common belief, a perfectly symmetrical FSCW can be obtained even with pole-slot combinations that do not respect the feasibility rule previously mentioned. In fact, all the available degrees of freedom on the choices of slots poles combination under some specifications, as will be explained in Chapter 6, are not sufficient. Another target is to reduce the harmful effect of the rich space harmonic content of FSCW in terms of losses in the magnets.

These goals can be achieved on condition that a multi-layer winding arrangement is used [16], which means using even more than one coil per tooth, belonging to different phases.

In this thesis, the multilayer winding arrangement will be described in more detail. Then, the development of systematic automated analytical method aimed at the optimization of the multilayer FSCW SPM machines will be presented. The winding optimization approach is based on quadratic programming, which can be solved using computationally efficient algorithms, under some constraints

and objective functions depending on the goal of the optimization [17].

This thesis is composed of a first chapter including definitions on multilayer fractional slot concentrated winding, a mathematical definition of air gap MMF harmonic computation and analytical computation of magnet losses produced by eddy currents induced by concentrated winding air gap MMF harmonic content. The second chapter addresses the definition of the optimization problem: objective function and constraints, limits and results [18]. The third chapter describes an evolution of star of slots method, while in the following chapters optimization approach is introduced to design unconventional machines (slots poles combinations that do not respect the feasibility rule) [19]. The method is validated by comparison with finite element simulations and based on experimental results collected on two different prototypes (three and six-phase machines).

1. Multi-layer Fractional-slot concentrated windings

The use of fractional-slot concentrated windings (FSCW) in the design of permanent magnet synchronous machines is growing in popularity due to a number of benefits, including improved manufacturability and modularity, increased flux weakening performance, fault tolerance features [20], shorter end-coil and overall axial length [21]. The occurrence of significant magneto-motive force (MMF) space harmonics (particularly subharmonics), which generate eddy-current losses in the rotor, with possible overheating and demagnetization concerns, is a well-known disadvantage of FSCWs.

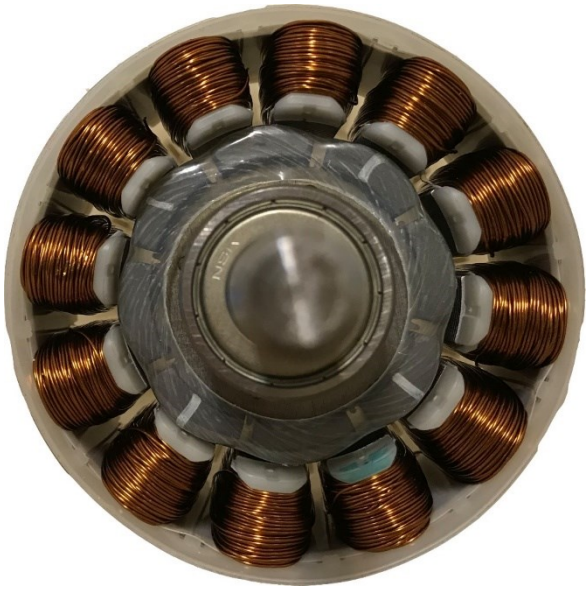

Fig. 1 Structure of a dual - layer concentrated winding

1.1. Multilayer FSCW model

This thesis introduces a new general, systematic and fully automated approach to optimizing a multi-phase multilayer FSCW for a surface-mounted permanent magnet (SPM) machine, based on two arbitrarily weighted objectives: maximization of the MMF fundamental on one side and minimization of total rotor losses (not a specific MMF harmonic) on the other. Constraints are imposed to guarantee that the winding is feasible using (non-overlapping) tooth coils [20]. The problem is expressed as a dual-objective quadratic programming problem with linear constraints, which can be solved quickly using known computationally efficient algorithms[30].

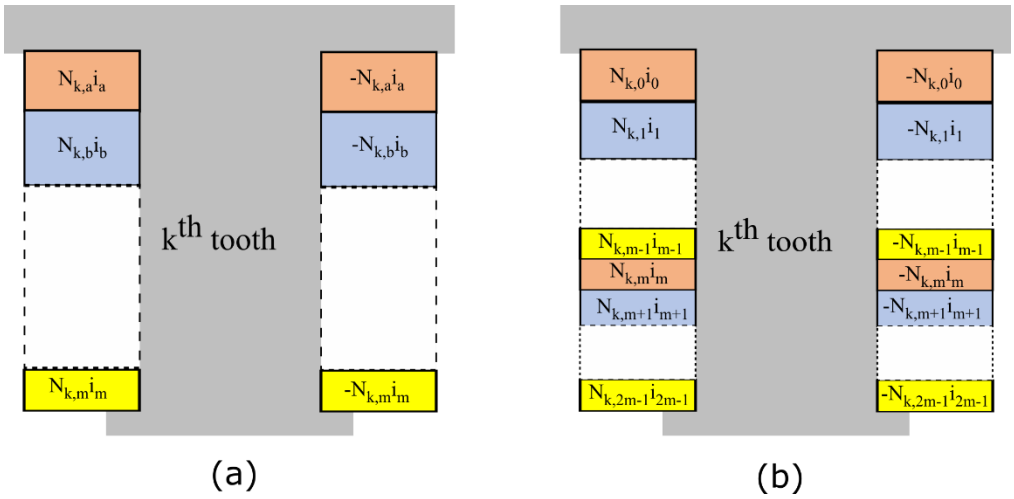

Fig. 2 (a) Phase sub-coils wound on the k^{th} turn are relevant amperturns; (b) Equivalent configuration with 2m sub-coils per tooth.

Each of the Z stator teeth in a multilayer FSCW machine is assumed to have the structure shown in Fig. 2(a). Having m number of phases, m coils are wound around it in general, one for each of the m phases. The numbers of turns $N_{k,a}$, $N_{k,b}$, …,$N_{k,m}$ of the m coils must be taken positive or negative depending on the direction of the relevant currents i_a, i_b, …, i_m, assuming a conventional positive direction for the current (e.g., positive if entering the page, negative otherwise). Hence, calling N_0 the total number of turns which can be wound around a tooth, the following constraint must hold:

$$|N_{k,a}| + |N_{k,b}| + |N_{k,c}| + \cdots + |N_{k,m}| \leq N_0 \qquad (1\text{-}1)$$

and the total amperturns flowing around the kth tooth are

$$N_{k,a}i_a + N_{k,b}i_b + N_{k,c}i_c + \cdots + N_{k,m}i_m \qquad (1\text{-}2)$$

Regardless of the objective function, the FSCW optimal design implies determining the number of turns $N_{k,a}$, $N_{k,b}$,..., $N_{k,m}$ (design variables) for any k=0, 1, ..., Z–1 under suitable constraints, including (1-1).

The optimization approach proposed in this thesis, based on quadratic programming, can be applied if the objective function is a linear or quadratic function of the design variables [30]. Moreover, it requires the constraints to be linear equalities or inequalities. Therefore, (1-1) is unfit as a constraint due to its intrinsic non-linear nature with respect to the design variables $N_{k,a}$, $N_{k,b}$,..., $N_{k,m}$. To get round the problem, it is convenient to introduce a system of fictitious "sub-currents". For example, in the three-phase case, they will be i_0, i_1, i_3, i_4, i_5, whose phasors are shown in Fig. 3 together with the phasors of the physical currents i_a, i_b and i_c.

It is easily seen that

$$i_a = i_0 = -i_3 \; ; \; i_b = i_2 = -i_5 \; ; \; i_c = i_4 = -i_1. \qquad (1\text{-}3)$$

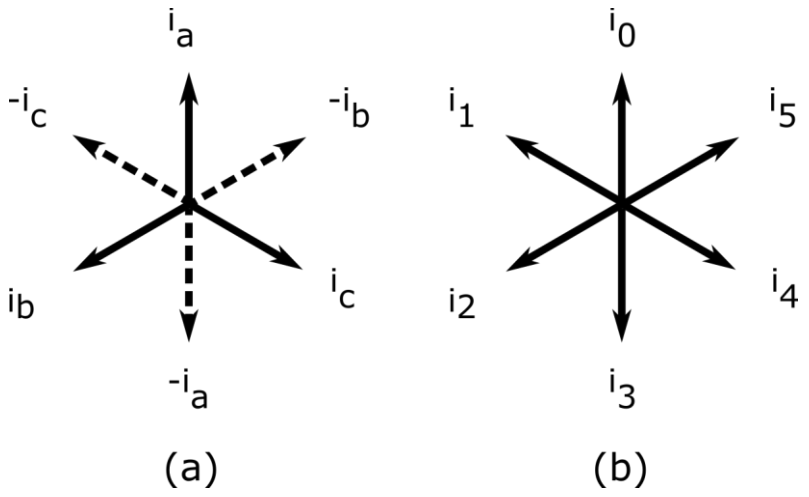

Fig. 3 Three phases case (a) Phase current phasors. (b) Equivalent sub-phase phasors.

With such a choice, each phase coil wound on the k^{th} tooth can be split into a couple of "sub-coils" having the same overall number of turns, as shown in Fig. 2(b). As a result, six sub-coils are wound around the tooth, each composed of $N_{k,j} \geq 0$ turns with $j = 0, 1, \ldots, 5$, such that

$$N_{k,0} + N_{k,1} + N_{k,2} + N_{k,3} + \cdots + N_{k,2m-1} \leq N_0$$

(1-4)

The amperturns flowing around the k^{th} tooth are now:

$$N_{k,0} i_0 + N_{k,1} i_1 + N_{k,2} i_2 + N_{k,3} i_3 + \cdots + N_{k,2m-1} i_{2m-1}$$

(1-5)

For the configurations depicted in Fig. 2 (a) e (b) to be equivalent in terms of air-gap MMF, we must impose that (1-2) and (1-5) be equal.

Based on (1-3) , this happens if (e.g., in the three-phase case):

$$N_{k,a} = N_{k,0} - N_{k,3} \;\; ; \; N_{k,b} = N_{k,2} - N_{k,5} \; ; \; N_{k,c} = N_{k,4} - N_{k,1}$$

(1-6)

The model assumed in the rest of this thesis is therefore that shown in Fig. 2 (b), which is equivalent to the physical configuration Fig. 2 (a), under the assumption (1-6). Accordingly, the design variables will be the positive or null quantities $N_{k,j}$ subject to the linear constraint (1-4). Taking the phase "a" (or sub-phase "0") as a reference, the currents flowing in the $2m$ sub-coils of each tooth will be (for a generic number of phases):

$$i_j(t) = I_0 \cos\left(\omega t - \frac{\pi}{m} j \right)$$

(1-7)

where I_0 and f are the phase current amplitude and frequency, $\omega = 2\pi f$ and $j = 0, 1, \ldots, m$.

1.2. Air-gap MMF harmonic computation

In order to optimize the FSCW design with respect to its space harmonic content, it is necessary to derive an explicit expression for the air-gap MMF harmonics as functions of the design variables identified in the previous subsection, i.e. the numbers of turns $N_{k,j}$.

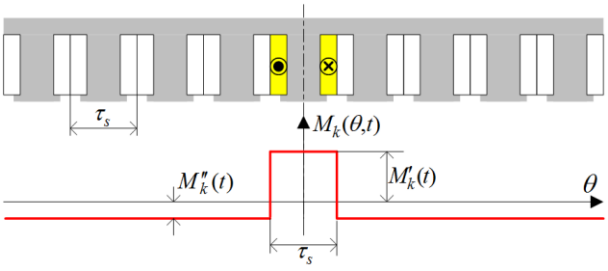

Fig. 4 Air-gap MMF produced by the kth wound tooth energized with a total current $i_k(t)$.

The air-gap MMF due to the entire winding can be computed by summing the contributions of each tooth in the hypothesis of unsaturated stator and rotor cores. For the k^{th} tooth, the air-gap MMF $M_k(\theta, t)$ due to its amperturns (1-5) has the waveform shown in Fig. 4, where $\tau_s=2\pi/Z$ and [31]:

$$M'_k(t) = \frac{Z-1}{Z} \sum_{j=0..2m-1} N_{k,j} i_j(t)$$

$$M''_k(t) = \frac{-1}{Z} \sum_{j=0..2m-1} N_{k,j} i_j(t) \qquad (1\text{-}8)$$

Using Fourier series, the expression for $M_k(\theta, t)$ is

$$M_k(\theta,t) = \left(\sum_{j=0..2m-1} N_{k,j} i_k(t) \right) \left(\sum_{n=1..\infty} a_n \cos(n\theta) \right) \qquad (1\text{-}9)$$

where $a_n = \frac{2}{\pi}\frac{1}{n}(-1)^n \sin\left(\frac{\pi n(Z-1)}{Z}\right)$.

(1-10)

Summing over all the teeth (displaced by $2\pi/Z$ apart) and substituting (1-8), the total air-gap MMF is:

$$M(\theta,t) = \sum_{k=0..Z-1} M_k(\theta - k\frac{2\pi}{Z}, t) =$$

$$= \sum_{k=0..Z-1}\sum_{j=0..2m-1}\sum_{n=1..\infty} a_n N_{k,j} I_0 \cos\left(\omega t - j\tfrac{\pi}{m}\right)\cos\left(n\theta - nk\tfrac{2\pi}{Z}\right)$$

(1-11)

Equation (1-11) can be manipulated using the identity

$$\cos\left(\omega t - j\frac{\pi}{m}\right)\cos\left(n\theta - nk\frac{2\pi}{Z}\right) = Re\left\{e^{i\left(\omega t - j\frac{\pi}{m}\right)}\frac{1}{2}\left[e^{i\left(n\theta - nk\frac{2\pi}{Z}\right)} + e^{-i\left(n\theta - nk\frac{2\pi}{Z}\right)}\right]\right\}$$

(1-12)

and, after few passages, can be put in the following form:

$$M(\theta,t) = \mathrm{Re}\left\{\sum_{n=1..\infty}\left[m_n^- e^{i(\omega t - n\theta)} + m_n^+ e^{i(\omega t + n\theta)}\right]\right\}$$

(1-13)

$$= \mathrm{Re}\left\{\sum_{n=1..\infty}\left[\left|m_n^-\right| e^{i\left(\omega t - n\theta + \arg\left(m_n^-\right)\right)} + \left|m_n^+\right| e^{i\left(\omega t + n\theta + \arg\left(m_n^+\right)\right)}\right]\right\}$$

$$= \sum_{n=1..\infty}\left[\left|m_n^-\right|\cos\left[\omega t - n\theta + \arg\left(m_n^-\right)\right] + \left|m_n^+\right|\cos\left[\omega t + n\theta + \arg\left(m_n^+\right)\right]\right]$$

where

$$m_n^- = \frac{a_n I_0}{2}\sum_{k=0..Z-1}\sum_{j=0..2m-1} N_{k,j} e^{i\left(-\frac{\pi}{m}j + kn\frac{2\pi}{Z}\right)}$$

(1-14)

$$m_n^+ = \frac{a_n I_0}{2} \sum_{k=0..Z-1} \sum_{j=0..2m-1} N_{k,j} e^{i\left(-\frac{\pi}{m}j - kn\frac{2\pi}{Z}\right)}$$

(1-15)

These are the complex coefficients for the n^{th}-order MMF space harmonics, respectively revolving in the same (sign "–") and opposite (sign "+") direction with respect to the rotor. A more compact expression for (1-14) - (1-15) can be obtained if all the variables N_{kj} are grouped into a single $2mZ$-sized "turn vector" $\mathbf{x}$ defined as follows

$$\mathbf{x} = (\mathrm{N_{0,0}} \ldots \mathrm{N_{0,2m\text{-}1}}|\, \mathrm{N_{1,0}} \ldots \mathrm{N_{1,2m\text{-}1}}|\, \mathrm{N_{2,0}} \ldots \mathrm{N_{2,2m\text{-}1}}|\ldots |\mathrm{N_{Z\text{-}1,0}} \ldots \mathrm{N_{Z\text{-}1,2m\text{-}1}})^{\mathrm{T}}.$$

(1-16)

such that

$$[\boldsymbol{x}]_{2mk+j} = N_{k,j} \quad \forall j = 0..2m-1;\ k = 0..Z-1$$

(1-17)

This allows for (1-14) (1-15) to be written as

$$m_n^{\pm} = \frac{a_n I_0}{2} \sum_{h=0..2mZ-1} [\boldsymbol{x}]_h e^{i\left[-\frac{\pi}{m} mod(h,2m) \mp n\frac{2\pi}{Z} \mathrm{floor}(h/2m)\right]} = \boldsymbol{v}_n^{\pm T}\boldsymbol{x}$$

(1-18)

where mod(x, y) and floor(x, y) respectively return the reminder and integer part for the division of x by y and the complex vectors $\mathbf{v}_n^+$ and $\mathbf{v}_n^-$ are defined as follows:

$$\left[\boldsymbol{v}_n^{\pm}\right]_h = \frac{1}{2} a_n I_0 e^{i\left[-\frac{\pi}{3} mod(h,2m) \mp n\frac{2\pi}{Z} \mathrm{floor}(h,2m)\right]} \quad \forall h = 0..2mZ-1$$

(1-19)

Based on (1-18), the air-gap space harmonic amplitudes appearing in (1-13) can be then expressed as

$$|m_n^{\pm}| = \sqrt{\bar{m}_n^{\pm} m_n^{\pm}} = \sqrt{\overline{\left(\boldsymbol{v}_n^{\pm T}\boldsymbol{x}\right)}\left(\boldsymbol{v}_n^{\pm T}\boldsymbol{x}\right)} = \sqrt{\overline{\left(\boldsymbol{v}_n^{\pm T}\boldsymbol{x}\right)}^{T}\left(\boldsymbol{v}_n^{\pm T}\boldsymbol{x}\right)}$$

$$= \sqrt{\boldsymbol{x}^T \bar{\boldsymbol{v}}_n^{\pm} \boldsymbol{v}_n^{\pm T}\boldsymbol{x}} = \sqrt{\boldsymbol{x}^T \boldsymbol{H}_n^{\pm}\boldsymbol{x}}$$

(1-20)

where overlines indicate complex conjugates and $\mathbf{H}_n^{\pm}$ are the symmetric $2mZ \times 2mZ$ matrices defined as follows

$$\boldsymbol{H}_n^{\pm} = \bar{\boldsymbol{v}}_n^{\pm} \boldsymbol{v}_n^{\pm T}$$

(1-21)

According to this definition, $\mathbf{H}_n^{\pm}$ are complex-valued matrices. However, we observe that, being the $\mathbf{x}$ vector (1-16) real, from (1-20) one can write

$$\left|m_n^{\pm}\right|^2 = Re\left\{\left|m_n^{\pm}\right|^2\right\} = \boldsymbol{x}^T Re\{\boldsymbol{H}_n^{\pm}\}\boldsymbol{x} = \boldsymbol{x}^T \boldsymbol{Q}_n^{\pm} \boldsymbol{x}$$

(1-22)

where $\mathbf{Q}_n^{\pm} = \mathbf{Re}\{\mathbf{H}_n^{\pm}\}$ are real-valued symmetric matrices. Based on (1-21), they can be computed as

$$\boldsymbol{Q}_n^{\pm} = Re\left\{\bar{\boldsymbol{v}}_n^{\pm} \boldsymbol{v}_n^{\pm T}\right\} = Re\{\boldsymbol{v}_n^{\pm}\} Re\left\{\boldsymbol{v}_n^{\pm T}\right\} + Im\{\boldsymbol{v}_n^{\pm}\} Im\left\{\boldsymbol{v}_n^{\pm T}\right\}$$

(1-23)

1.3. Single phase contribution to the MMF fundamental

One of the constraints to be imposed for the FSCW optimization will be the symmetry of the three-phase system. In order to formalize this constraint, it is useful to identify the contribution of the three phases to the MMF fundamental. The latter is obtained from (1-13) considering only the harmonic order n equal to the number of pole pairs p and revolving in the same direction as the rotor, that is:

$$M_{fund}(\theta, t) = \mathrm{Re}\{\mathrm{m_p^- e^{i(\omega t - p\theta)}}\}$$

(1-24)

Substitution of (1-18) into (1-24) gives:

$$M_{fund}(\theta, t) = Re\{\boldsymbol{v}_p^{-T} \boldsymbol{x} e^{i(\omega t - p\theta)}\}$$

(1-25)

To determine the MMF fundamental

$$M_{fund}(\theta,t) = Re\left\{\boldsymbol{v}_p^{-T}\boldsymbol{x}e^{i(\omega t - p\theta)}\right\}$$

(1-25)

due to the three phases individually, we introduce the following $2m \times 2m$ matrices:

$$\mathbf{K}_{2m,a} = \left(\begin{array}{ccccc|ccccc} 1 & 0 & 0 & \dots & 0 & 0 & 0 & 0 & \dots & 0 \\ 0 & 0 & 0 & \dots & 0 & 0 & 0 & 0 & \dots & 0 \\ 0 & 0 & 0 & \dots & 0 & 0 & 0 & 0 & \dots & 0 \\ \dots & \dots & \dots & \dots & 0 & \dots & \dots & \dots & \dots & 0 \\ 0 & 0 & 0 & 0 & 0 & 0 & 0 & 0 & 0 & 0 \\ \hline 0 & 0 & 0 & \dots & 0 & 1 & 0 & 0 & \dots & 0 \\ 0 & 0 & 0 & \dots & 0 & 0 & 0 & 0 & \dots & 0 \\ 0 & 0 & 0 & \dots & 0 & 0 & 0 & 0 & \dots & 0 \\ \dots & \dots & \dots & \dots & 0 & \dots & \dots & \dots & \dots & 0 \\ 0 & 0 & 0 & 0 & 0 & 0 & 0 & 0 & 0 & 0 \end{array}\right); \mathbf{K}_{2m,b} = \left(\begin{array}{ccccc|ccccc} 0 & 0 & 0 & \dots & 0 & 0 & 0 & 0 & \dots & 0 \\ 0 & 1 & 0 & \dots & 0 & 0 & 0 & 0 & \dots & 0 \\ 0 & 0 & 0 & \dots & 0 & 0 & 0 & 0 & \dots & 0 \\ \dots & \dots & \dots & \dots & 0 & \dots & \dots & \dots & \dots & 0 \\ 0 & 0 & 0 & 0 & 0 & 0 & 0 & 0 & 0 & 0 \\ \hline 0 & 0 & 0 & \dots & 0 & 0 & 0 & 0 & \dots & 0 \\ 0 & 0 & 0 & \dots & 0 & 0 & 1 & 0 & \dots & 0 \\ 0 & 0 & 0 & \dots & 0 & 0 & 0 & 0 & \dots & 0 \\ \dots & \dots & \dots & \dots & 0 & \dots & \dots & \dots & \dots & 0 \\ 0 & 0 & 0 & 0 & 0 & 0 & 0 & 0 & 0 & 0 \end{array}\right)$$

$$\mathbf{K}_{2m,m} = \left(\begin{array}{ccccc|ccccc} 0 & 0 & 0 & 0 & 0 & 0 & 0 & 0 & 0 & 0 \\ 0 & \dots & \dots & \dots & \dots & 0 & \dots & \dots & \dots & \dots \\ 0 & \dots & 0 & 0 & 0 & 0 & \dots & 0 & 0 & 0 \\ 0 & \dots & 0 & 0 & 0 & 0 & \dots & 0 & 0 & 0 \\ 0 & \dots & 0 & 0 & 1 & 0 & \dots & 0 & 0 & 0 \\ \hline 0 & 0 & 0 & 0 & 0 & 0 & 0 & 0 & 0 & 0 \\ 0 & \dots & \dots & \dots & \dots & 0 & \dots & \dots & \dots & \dots \\ 0 & \dots & 0 & 0 & 0 & 0 & \dots & 0 & 0 & 0 \\ 0 & \dots & 0 & 0 & 0 & 0 & \dots & 0 & 0 & 0 \\ 0 & \dots & 0 & 0 & 0 & 0 & \dots & 0 & 0 & 1 \end{array}\right)$$

(1-26)

while $\mathbf{0}_{2m}$ are null $2m$ x $2m$ matrices, and use them to build the following $2mZ \times 2mZ$ matrices:

$$\mathbf{K}_a = \begin{pmatrix} \mathbf{K}_{2m,a} & \mathbf{0}_{2m} & \cdots & \mathbf{0}_{2m} \\ \mathbf{0}_{2m} & \mathbf{K}_{2m,a} & \cdots & \mathbf{0}_{2m} \\ \vdots & \vdots & \ddots & \vdots \\ \mathbf{0}_{2m} & \mathbf{0}_{2m} & \cdots & \mathbf{K}_{2m,a} \end{pmatrix}; \dots; \mathbf{K}_m = \begin{pmatrix} \mathbf{K}_{2m,m} & \mathbf{0}_{2m} & \cdots & \mathbf{0}_{2m} \\ \mathbf{0}_{2m} & \mathbf{K}_{2m,m} & \cdots & \mathbf{0}_{2m} \\ \vdots & \vdots & \ddots & \vdots \\ \mathbf{0}_{2m} & \mathbf{0}_{2m} & \cdots & \mathbf{K}_{2m,m} \end{pmatrix}$$

(1-27)

It can be easily seen that, when summed together, the matrices in (1-27) give the 2mZ×2mZ identity matrix $\mathbf{I}_{2mZ}$. Hence, the turn vector $\mathbf{x}$ can be also written as:

$$\boldsymbol{x} = \boldsymbol{I}_{2mZ}\boldsymbol{x} = (\boldsymbol{K}_a + \boldsymbol{K}_b + \ldots + \boldsymbol{K}_m)\boldsymbol{x} = \boldsymbol{x}_a + \boldsymbol{x}_b + \ldots + \boldsymbol{x}_m$$

(1-28)

where

$$\boldsymbol{x}_a = \boldsymbol{K}_a\boldsymbol{x}\ , \quad \boldsymbol{x}_b = \boldsymbol{K}_b\boldsymbol{x}, \quad \ldots \quad , \boldsymbol{x}_m = \boldsymbol{K}_m\boldsymbol{x}.$$

(1-29)

Considering the structure of $\mathbf{K}_a$ and of the turn vector $\mathbf{x}$, it is apparent that $\mathbf{x}_a$ represents a new FSCW where the number of turns for sub-phases "0" and "m" (corresponding to "a" and "$-a$", Fig. 3) is the same as in $\mathbf{x}$ while all the other sub-phases are set to have zero turns. As an example, the winding configuration identified by the turn vector $\mathbf{x}_a$ is shown in Fig. 5 (a) for the k^{th} tooth. Similarly, Fig. 5 (b) and Fig. 5 (c) show the winding configurations identified by the turn vectors $\mathbf{x}_b$ and $\mathbf{x}_m$, where only the turns of phases "b" and "m" are considered, respectively.

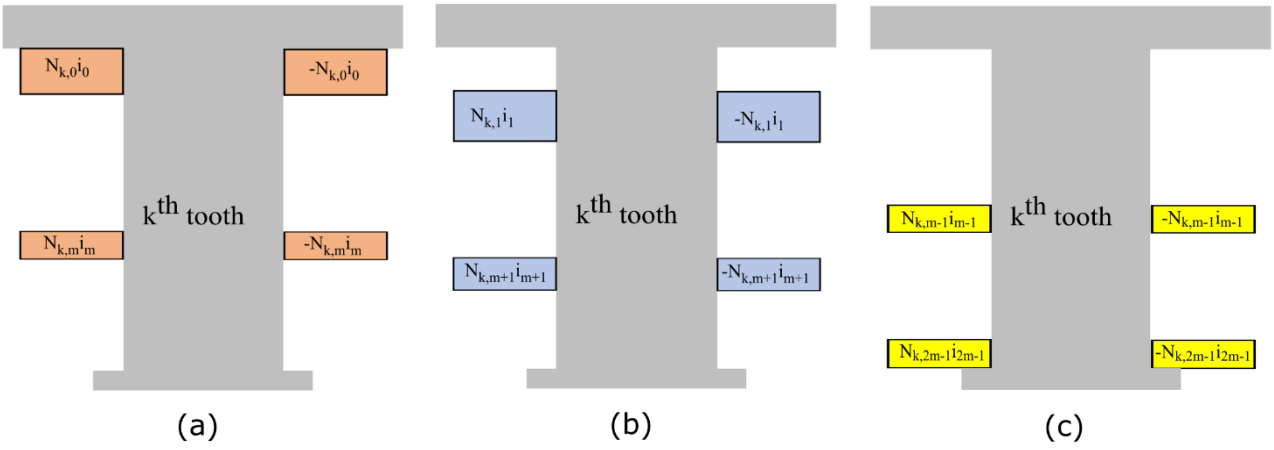

Fig. 5 k^{th} tooth configuration when the turn vector is equal to (a) $\mathbf{x}_a=\mathbf{K}_a\mathbf{x}$; (b) $\mathbf{x}_b=\mathbf{K}_b\mathbf{x}$; … ; (c) $\mathbf{x}_m=\mathbf{K}_m\mathbf{x}$

Substitution of (1-28) into (1-25) gives:

$$M_{fund}(\theta,t) = \mathrm{Re}\left\{\mathbf{v}_p^{-T}\left(\mathbf{x}_a + \mathbf{x}_b + \ldots + \mathbf{x}_m\right)e^{j(\omega t - p\theta)}\right\} = M_{fund,a}(\theta,t) + M_{fund,b}(\theta,t) + \ldots + M_{fund,m}(\theta,t)$$

(1-30)

where $M_{fund,a}$, $M_{fund,b}$ and $M_{fund,m}$ are:

$$M_{fund,a}(\theta,t)=\mathrm{Re}\left\{\mathbf{v}_p^{-T}\mathbf{x}_a e^{i(\omega t-p\theta)}\right\}=\left|\mathbf{v}_p^{-}\mathbf{x}_a{}^{T}\right|\cos\left(\omega t-p\theta+\arg(\mathbf{v}_p^{-T}\mathbf{x}_a)\right)$$

(1-31)

$$M_{fund,b}(\theta,t)=\mathrm{Re}\left\{\mathbf{v}_p^{-T}\mathbf{x}_b e^{i(\omega t-p\theta)}\right\}=\left|\mathbf{v}_p^{-T}\mathbf{x}_b\right|\cos\left(\omega t-p\theta+\arg(\mathbf{v}_p^{-T}\mathbf{x}_b)\right)$$

(1-32)

…

$$M_{fund,m}(\theta,t)=\mathrm{Re}\left\{\mathbf{v}_p^{-T}\mathbf{x}_m e^{i(\omega t-p\theta)}\right\}=\left|\mathbf{v}_p^{-T}\mathbf{x}_m\right|\cos\left(\omega t-p\theta+\arg(\mathbf{v}_p^{-T}\mathbf{x}_m)\right)$$

(1-33)

and represent the MMF fundamentals produced by the three phases a, b, … m individually.

In order for the winding to be symmetric, the three sinusoidal waves in (1-33) -(1-33) must be equal in magnitude and phase, which implies the equality of the m complex numbers $\boldsymbol{v}_p^{-T}\boldsymbol{x}_a$, $\boldsymbol{v}_p^{-T}\boldsymbol{x}_b$ and $\boldsymbol{v}_p^{-T}\boldsymbol{x}_m$, i.e.:

$$\mathrm{Re}\left\{v_p^{-T}\left(\mathbf{x}_b-\mathbf{x}_a\right)\right\}=\mathrm{Im}\left\{v_p^{-T}\left(\mathbf{x}_b-\mathbf{x}_a\right)\right\}=0$$

$$\mathrm{Re}\left\{v_p^{-T}\left(\mathbf{x}_c-\mathbf{x}_b\right)\right\}=\mathrm{Im}\left\{v_p^{-T}\left(\mathbf{x}_c-\mathbf{x}_b\right)\right\}=0$$

…

$$\mathrm{Re}\left\{v_p^{-T}\left(\mathbf{x}_m-\mathbf{x}_{m-1}\right)\right\}=\mathrm{Im}\left\{v_p^{-T}\left(\mathbf{x}_m-\mathbf{x}_{m-1}\right)\right\}=0$$

(1-34)

Considering (1-29), this results in the following set of linear constraints to be applied to the turn vector $\mathbf{x}$

$$Re\left\{v_p^{-T}(\boldsymbol{K}_b-\boldsymbol{K}_a)\right\}\boldsymbol{x}=Im\left\{v_p^{-T}(\boldsymbol{K}_b-\boldsymbol{K}_a)\right\}\boldsymbol{x}=0$$

$$Re\left\{v_p^{-T}(\boldsymbol{K}_c-\boldsymbol{K}_b)\right\}\boldsymbol{x}=Im\left\{v_p^{-T}(\boldsymbol{K}_c-\boldsymbol{K}_b)\right\}\boldsymbol{x}=0$$

(1-35)

1.4. Calculation of magnet eddy-current losses

One of the objectives of the FSCW optimization is reducing the eddy-current losses which arise in the magnets as a consequence of the air-gap MMF harmonics analyzed in 1.2. To this end, it is important to have a fast but accurate formula that expresses the eddy-current losses produced in the magnets by each of the stator MMF space harmonic. In the literature, the problem has been often addressed through conformal transformations leading to a linear geometry for the air-gap [4]. However, the use of conformal transformations for energy or loss computation can introduce some inaccuracies [32]. For this reason, it is found safer to consider a circular air-gap model like that shown in Fig. 6 as described next

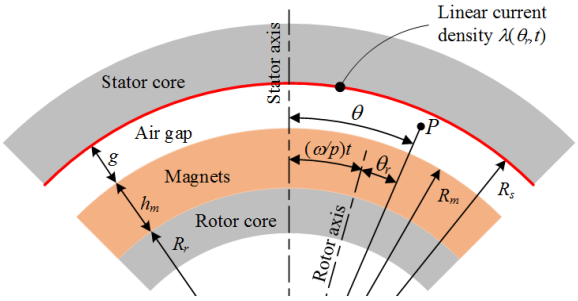

Fig. 6 Geometric model for the analysis of magnet eddy-current losses due to air-gap MMF harmonics

1.4.1. Model for magnet loss computation

With regard to Fig. 6, the following simplifications are assumed: stator slotting is neglected; stator and rotor cores are assumed infinitely permeable; rotor magnets are modeled as a continuous annulus with magnetic permeability μ and electric conductivity σ. Introducing a rotor-attached polar reference frame with coordinates r and θ_r (which revolves at ω/p radians per second) and calling θ the angular position of a generic point P in the stator reference frame, its position θ_r with respect to the rotor is such that

$$\theta = \theta_r + \frac{\omega}{p}t \qquad (1\text{-}36)$$

Substitution of (1-36) into (1-13) leads to express the stator MMF in rotor coordinates as follows

$$M\left(\theta_r + \frac{\omega}{p}t, t\right) = Re\left\{\sum_{n=1..\infty}\left[m_n^- e^{i(\omega(1-\frac{n}{p})t - n\theta_r)} + m_n^+ e^{i(\omega(1+\frac{n}{p})t + n\theta_r)}\right]\right\}$$

(1-37)

In the model shown in Fig. 4, stator MMF is represented by an equivalent linear current distribution $\lambda(\theta_r, t)$, spread around the stator bore surface, such that:

$$\lambda(\theta_r, t) = \frac{1}{R_s}\frac{\partial}{\partial\theta_r}M\left(\theta_r + \frac{\omega}{p}t, t\right)$$

(1-38)

This naturally imposes a tangential component of the air-gap magnetic field at $r=R_s$ given by:

$$H_\theta(\theta_r, t)|_{r=R_s} = \lambda(\theta_r, t) =$$

$$= \frac{1}{R_s}Re\left\{\sum_{n=1..\infty}\left[-n\ m_n^- e^{i(\omega(1-\frac{n}{p})t - n\theta_r)} + n\ m_n^+ e^{i(\omega(1+\frac{n}{p})t + n\theta_r)}\right]\right\}$$

(1-39)

Such magnetic field can be expressed by the following complex phasors (functions of θ_r):

$$H_\theta^\pm(\theta_r)\big|_{r=R_s} = \pm\frac{1}{R_s}\sum_{n=1..\infty} n\ m_n^\pm e^{\pm in\theta_r}$$

(1-40)

associated with the rotor frequencies:

$$\omega_n^\pm = \omega(1 \pm n/p)$$

(1-41)

1.4.2. Determining the vector potential in the magnet region

Given the generic n^{th}-order harmonic, associated with the rotor frequency $\omega_n^\pm$, we shall call $U_n^\pm(\theta_r, r)$ and $V_n^\pm(\theta_r, r)$ the complex vector potentials it produces respectively in the gap and magnet

regions. The two vector potentials obey to the following Laplace's and Helmholtz's differential equations [33]:

$$\frac{\partial^2 U_n^{\pm}}{\partial r^2}+\frac{1}{r}\frac{\partial U_n^{\pm}}{\partial r}+\frac{1}{r^2}\frac{\partial^2 U_n^{\pm}}{\partial {\theta_r}^2}=0 \qquad R_m \le r \le R_s$$

(1-42)

$$\frac{\partial^2 V_n^{\pm}}{\partial r^2}+\frac{1}{r}\frac{\partial V_n^{\pm}}{\partial r}+\frac{1}{r^2}\frac{\partial^2 V_n^{\pm}}{\partial {\theta_r}^2}=i\omega_n^{\pm}\mu\sigma V_n^{\pm} \qquad R_r \le r < R_m$$

(1-43)

where R_r, R_m and R_s are the radii shown in Fig. 6. The general solution for (1-42)(1-43) is assumed in the form below [33]:

$$U_n^{\pm}(r,\theta_r)=\left(A_n^{\pm}r^n+B_n^{\pm}r^{-n}\right)e^{\pm in\theta_r}$$

(1-44)

$$V_n^{\pm}(r,\theta_r)=\left[C_n^{\pm}J_n\left(\kappa_n^{\pm}r\right)+D_n^{\pm}Y_n\left(\kappa_n^{\pm}r\right)\right]e^{\pm in\theta_r}$$

(1-45)

where: $J_n(\cdot)$ and $Y_n(\cdot)$ are the n^{th}-order Bessel functions of the first and second kind; $A_n^{\pm}$, $B_n^{\pm}$, $C_n^{\pm}$ and $D_n^{\pm}$ are complex coefficients depending on boundary conditions; $\kappa_n^{\pm}$ is a complex coefficient such that $\left(\kappa_n^{\pm}\right)^2=-i\sigma\mu\omega_n^{\pm}$, i.e.:

$$\kappa_n^{\pm}=\sqrt{-i\sigma\mu\omega_n^{\pm}}=(1-i)\sqrt{\sigma\mu\omega_n^{\pm}/2}$$

(1-46)

To determine coefficients $A_n^{\pm}$, $B_n^{\pm}$, $C_n^{\pm}$ and $D_n^{\pm}$, the following boundary conditions are established

$$\pm\frac{1}{R_s}n\ m_n^{\pm}e^{\pm in\theta_r}=-\frac{1}{\mu_0}\left.\frac{\partial U_n^{\pm}}{\partial r}\right|_{r=R_s}$$

(1-47)

$$\left.\frac{\partial U_n^{\pm}}{\partial \theta_r}\right|_{r=R_m}=\left.\frac{\partial V_n^{\pm}}{\partial \theta_r}\right|_{r=R_m},\left.\frac{\partial U_n^{\pm}}{\partial r}\right|_{r=R_m}=\left.\frac{\partial V_n^{\pm}}{\partial r}\right|_{r=R_m}$$

(1-48)

$$\left.\frac{\partial V_n^{\pm}}{\partial r}\right|_{r=R_r} = 0$$

(1-49)

where: (1-47) imposes that the magnetic field tangential component at $r=R_s$ be equal to that given by (1-40); equations (1-48) impose the continuity of the radial and tangential field components across the boundary ($r=R_m$) between the gap and the magnets; (1-49) imposes that the magnetic field be purely radial on $r=R_r$. Equations (1-47) - (1-49), after the substitution of (1-44)(1-45), result in a linear system from which the coefficients $C_n^{\pm}$ and $D_n^{\pm}$ can be determined as follows:

$$C_n^{\pm} = -\frac{2i\mu_0 n\varphi_n^{\pm} m_n^{\pm}}{\Delta_n^{\pm} R_s {R_m}^2}, D_n^{\pm} = \frac{2i\mu_0 n\varepsilon_n^{\pm} m_n^{\pm}}{\Delta_n^{\pm} R_s {R_m}^2}$$

(1-50)

where $\varepsilon_n^{\pm}$, $\phi_n^{\pm}$ and $\Delta_n^{\pm}$ are defined by (1-51) - (1-56)

$$\begin{aligned}\Delta_n^{\pm} = {} & \left(\beta_n^{\pm}\varepsilon_n^{\pm} - \alpha_n^{\pm}\varphi_n^{\pm} - i\delta_n^{\pm}\varepsilon_n^{\pm} + i\chi_n^{\pm}\varphi_n^{\pm}\right){R_s}^{n-1}{R_m}^{-n-1} \\ & + \left(\alpha_n^{\pm}\varphi_n^{\pm} - \beta_n^{\pm}\varepsilon_n^{\pm} - i\delta_n^{\pm}\varepsilon_n^{\pm} + i\chi_n^{\pm}\varphi_n^{\pm}\right){R_m}^{n-1}{R_s}^{-n-1}\end{aligned}$$

(1-51)

$$\alpha_n^{\pm} = inJ_n\left(\kappa_n^{\pm}R_m\right){R_m}^{-1}, \beta_n^{\pm} = -inY_n\left(\kappa_n^{\pm}R_m\right){R_m}^{-1}$$

(1-52)

$$\chi_n^{\pm} = -\kappa_n^{\pm}J_{n+1}\left(\kappa_n^{\pm}R_m\right) + nR_m{}^{-1}J_n\left(\kappa_n^{\pm}R_m\right)$$

(1-53)

$$\delta_n^{\pm} = -\kappa_n^{\pm}Y_{n+1}\left(\kappa_n^{\pm}R_m\right) + nR_m{}^{-1}Y_n\left(\kappa_n^{\pm}R_m\right)$$

(1-54)

$$\varepsilon_n^{\pm} = \kappa_n^{\pm}J_{n+1}\left(\kappa_n^{\pm}R_r\right) - nR_r{}^{-1}J_n\left(\kappa_n^{\pm}R_r\right)$$

(1-55)

$$\varphi_n^{\pm} = \kappa_n^{\pm}Y_{n+1}\left(\kappa_n^{\pm}R_r\right) - nR_r{}^{-1}Y_n\left(\kappa_n^{\pm}R_r\right)$$

(1-56)

1.4.3. Determining magnet losses

Once the vector potential (1-45) in the magnet region is evaluated through (1-50) - (1-56), the eddy current density phasor $j_n^{\pm}$ in the magnets due to the n^{th}-order harmonic is also known as [33]:

$$j_n^{\pm}(r,\theta_r) = -i\omega_n^{\pm}\sigma V_n^{\pm}(r,\theta_r).$$

(1-57)

The eddy current losses $P_n^{\pm}$ in the magnet region due to the n^{th}-order harmonic will then be [33]:

$$P_n^{\pm} = \frac{L}{2\sigma}\int_0^{2\pi}\int_{R_r}^{R_m}\left|j_n^{\pm}(r,\theta_r)\right|^2 r dr d\theta_r$$

(1-58)

$$= \pi L {\omega_n^{\pm}}^2 \sigma \int_{R_r}^{R_m}\left|C_n^{\pm}J_n\left(\kappa_n^{\pm}r\right) + D_n^{\pm}Y_n\left(\kappa_n^{\pm}r\right)\right|^2 r dr$$

(1-59)

where L is the machine axial length. By substituting (1-50) into (1-58), one obtains:

$$P_n^{\pm} = \frac{4\pi {\mu_0}^2 n^2 L {\omega_n^{\pm}}^2 \sigma}{{R_m}^4 {R_s}^2\left|\Delta_n^{\pm}\right|^2}\left|m_n^{\pm}\right|^2 \times \int_{R_r}^{R_m}\left|\varepsilon_n^{\pm}Y_n\left(\kappa_n^{\pm}r\right) - \varphi_n^{\pm}J_n\left(\kappa_n^{\pm}r\right)\right|^2 r dr = p_n^{\pm}\left|m_n^{\pm}\right|^2$$

(1-60)

where $p_n^{\pm}$ gives the losses due to the n^{th}-order MMF harmonic, associated to the rotor frequency $\omega_n^{\pm}$ and having a unit magnitude, i.e.:

$$p_n^{\pm} = \frac{4\pi {\mu_0}^2 n^2 L {\omega_n^{\pm}}^2 \sigma}{{R_m}^4 {R_s}^2\left|\Delta_n^{\pm}\right|^2}\int_{R_r}^{R_m}\left|\varepsilon_n^{\pm}Y_n\left(\kappa_n^{\pm}r\right) - \varphi_n^{\pm}J_n\left(\kappa_n^{\pm}r\right)\right|^2 r dr$$

(1-61)

It is known that the superposition principle can be applied to the losses caused by different MMF harmonics [34]. Therefore, the total losses P_{loss} in the magnets are

$$P_{loss} = \sum_{n=1..\infty}(P_n^+ + P_n^-) = \sum_{n=1..\infty}(p_n^+|m_n^+|^2 + p_n^-|m_n^-|^2)$$

(1-62)

and, using(1-22), they can be written as:

$$P_{loss} = \sum_{n=1..\infty} (p_n^+ \mathbf{x}^T \boldsymbol{Q}_n^+ \mathbf{x} + p_n^- \mathbf{x}^T \boldsymbol{Q}_n^- \mathbf{x})$$

$$= \mathbf{x}^T \left[\sum_{n=1..\infty} (p_n^+ \boldsymbol{Q}_n^+ + p_n^- \boldsymbol{Q}_n^-) \right] \mathbf{x}$$

(1-63)

The total magnet losses are thus expressed as a quadratic function of the turn vector $\mathbf{x}$

More details about the validation of (1-63) are in Appendix B.

2. Design optimization of FSCW for SPM machines with three phases

At this point of the treatment, we have all the equations ready to define the FSCW optimal design as a quadratic programming problem. For this purpose, we shall separately identify the objective function and the constraints.

In this chapter will be introduced objective functions and constraints in order to formulate an optimization problem for three phase SPM machines and will be explained the results and limits obtained. The application of the procedure to machines with more than three phases with be addressed later on in this work.

2.1. Quadratic Programming Problem Formulation

As seen in 1.2, the whole stator winding arrangement is univocally defined once the six numbers N_{k0}, N_{k1}, …, N_{k5} are defined for any tooth index k=0, 1, …, Z–1. In other words, the winding arrangement is fully described by the 6Z-sized non-null winding vector $\mathbf{x}$ (1-16). Let us now suppose that the three stator phases carry the following set of symmetric balanced currents

$$i_a(t) = I_0 \cos(\omega t),$$

$$i_b(t) = I_0 \cos\left(\omega t - \frac{2}{3}\pi\right),$$

$$i_c(t) = I_0 \cos\left(\omega t - \frac{4}{3}\pi\right)$$

(2-1)

where I_0 is the current amplitude, t is time and ω is the stator angular frequency. The expression for the air-gap MMF due to such stator currents at time t in an angular position θ along the air-gap can be obtained (1-13) in the following form

$$M(\theta, t) = \sum_{n=1..\infty} \{M_n^- \cos[\omega t - n\theta + \phi_n^-] + M_n^+ \cos[\omega t + n\theta + \phi_n^+]\}$$

(2-2)

where: n is a positive integer; M_n^- and φ_n^- are the amplitude and phase of the n^{th}-order MMF space harmonic revolving in the rotor direction; M_n^+ and φ_n^+ are the amplitude and phase of the n^{th}-order MMF space harmonic revolving in the opposite direction with respect to the rotor.

As demonstrated in 1.2, the MMF harmonics are related to the winding vector $\mathbf{x}$ (1-16) through the following linear relationship:

$$M_n^{\pm} e^{j\phi_n^{\pm}} = \left[\boldsymbol{c}_n^{\pm} + j\boldsymbol{s}_n^{\pm}\right]^T \boldsymbol{x}$$

(2-3)

where j is the imaginary unit and $\boldsymbol{s}_n^{\pm}$ and $\boldsymbol{c}_n^{\pm}$ are constant 6Z-sized column vectors defined as:

$$\left[\boldsymbol{s}_n^{\pm}\right]_h = \frac{(-1)^n}{n\pi} sin\left(\frac{\pi n(Z-1)}{Z}\right) I_0 \, sin\left[-\frac{\pi}{3} mod(h,6) \mp n\frac{2\pi}{Z} \text{floor}\left(\frac{h}{6}\right)\right]$$

$$\left[\boldsymbol{c}_n^{\pm}\right]_h = \frac{(-1)^n}{n\pi} sin\left(\frac{\pi n(Z-1)}{Z}\right) I_0 \, cos\left[-\frac{\pi}{3} mod(h,6) \mp n\frac{2\pi}{Z} \text{floor}\left(\frac{h}{6}\right)\right]$$

$$\forall h = 0..6Z-1$$

(2-4)

In (2-4) mod(x, y) returns the reminder on dividing x by y and floor(x) returns the integer part of x.

The MMF harmonic amplitudes $\mathbf{c}_n^{\pm}$ and $\mathbf{s}_n^{\pm}$ are, instead, related to the winding vector $\mathbf{x}$ (1-16) through the following quadratic expression

$$\left(M_n^{\pm}\right)^2 = \boldsymbol{x}^T\left[\boldsymbol{c}_n^{\pm}\left(\boldsymbol{c}_n^{\pm}\right)^T + \boldsymbol{s}_n^{\pm}\left(\boldsymbol{s}_n^{\pm}\right)^T\right]\boldsymbol{x} = \boldsymbol{x}^T\boldsymbol{Q}_n^{\pm}\boldsymbol{x}$$

(2-5)

where $\mathbf{Q}_n^{\pm}$ is the $6Z$x$6Z$ real symmetric matrix

$$\boldsymbol{Q}_n^{\pm} = \boldsymbol{c}_n^{\pm}\left(\boldsymbol{c}_n^{\pm}\right)^T + \boldsymbol{s}_n^{\pm}\left(\boldsymbol{s}_n^{\pm}\right)^T$$

(2-6)

In particular, the MMF fundamental in a machine with p pole pairs coincides with the MMF harmonic of order p rotating in the same sense as the rotor; its amplitude M_{fund} is therefore obtained from (2-5) as

$$M_{fund} = M_p^- = \sqrt{\boldsymbol{x}^T\boldsymbol{Q}_p^-\boldsymbol{x}}$$

(2-7)

Alternatively, (2-3) yields the following couple of linear equations for the MMF fundamental.

$$M_{fund}\, cos\, \varphi_p = \left(\boldsymbol{c}_p^-\right)^T\boldsymbol{x}$$

$$M_{fund}\, sin\, \varphi_p = \left(\boldsymbol{s}_p^-\right)^T\boldsymbol{x}$$

(2-8)

where M_{fund} and $\boldsymbol{\varphi_p}$ are magnitude and phase of the MMF *fundamental*.

At this point of the treatment, we have all the equations ready to define the FSCW optimal design as a quadratic programming problem. For this purpose, we shall separately identify the objective function and the constraints.

2.2. Objective functions

The optimal multilayer FSCW design is intrinsically a dual-objective optimization problem: one goal is to maximize the MMF fundamental; the other objective is to minimize the parasitic behavior subject to optimization (e.g. rotor losses) due to MMF space harmonics. In more formal terms, the two objective functions are described below.:

$$f_{fund}(\boldsymbol{x}) = -\left|m_p^-\right|^2 = -\boldsymbol{x}^T \boldsymbol{Q}_p \boldsymbol{x} \tag{2-9}$$

$$f_{loss}(\boldsymbol{x}) = \boldsymbol{x}^T \left[\sum_{n=1..\infty} (p_n^+ \boldsymbol{Q}_n^+ + p_n^- \boldsymbol{Q}_n^-) \right] \boldsymbol{x} \tag{2-10}$$

The former returns minus the square of the magnitude of the MMF fundamental based on (1-22); the latter returns the total magnet losses due to MMF harmonics based on (1-63). Both functions are to be minimized.

An effective way to cope with dual-objective optimization problems is it to simplify them into a single-objective form though a weighed sum. For example, we can define a weighing coefficient $w \in [0,1]$ and generate the following w-dependent objective function:

$$f_w(\boldsymbol{x}) = (1-w) f_{fund}(\boldsymbol{x}) + w f_{loss}(\boldsymbol{x})$$

$$= \boldsymbol{x}^T \left[-(1-w)\boldsymbol{Q}_p^- + w \sum_{n=1..\infty} (p_n^+ \boldsymbol{Q}_n^+ + p_n^- \boldsymbol{Q}_n^-) \right] \boldsymbol{x} = \boldsymbol{x}^T \boldsymbol{F}_w \boldsymbol{x}$$

(2-11)

where the $6Z \times 6Z$ real symmetric matrix $\mathbf{F}_w$ is given by:

$$\boldsymbol{F}_w = (w-1)\boldsymbol{Q}_p^- + w \sum_{n=1..\infty} (p_n^+ \boldsymbol{Q}_n^+ + p_n^- \boldsymbol{Q}_n^-)$$

(2-12)

.

Equation (2-11) therefore defines the total quantity to be minimized. Of course, the optimization is expected to yield different results depending on the value assigned to w.

In order to know the optimal design only in terms of fundamental of MMF, for a certain slot and pole combination, it is necessary to set w=0. In this case (2-12) becomes a real single objective function, which maximizes the fundamental of MMF.

With this strategy, as the output of the optimization dual layer winding is found, the same that can be produced by the methodology called "*Star of slots*" (it will be better discussed in following sections).

Through the use of a weighing coefficient w, the dual-objective optimization can be reduced to a real single-objective form. In practice, however, the objective function dependency on the weight makes it exceedingly sensitive even to little changes.

In order to cope these numerical problems, one way to avoid using weighting coefficients is to consider only a single objective function and treat the other one as a constraint. In this case, the main objective function to be minimized is the one dealing with the parasitic effects (e.g., the losses in the magnets).

$$\text{minimize } P_{loss} = \boldsymbol{x}^T \left[\sum_{n=1}^{\infty} (p_n^+ \boldsymbol{Q}_n^+ + p_n^- \boldsymbol{Q}_n^-) \right] \boldsymbol{x}$$

(2-13)

2.3. Constraints

In order to solve a quadratic optimization problem and obtain a feasible result, it is necessary to set constraints.

The first constraint, as discussed in 1.1, is the maximum number of turns N_0 that can be accommodated around a wound tooth. The condition, expressed by (1-4) for the k^{th} tooth, can be formulated compactly for all the teeth using the turn vector $\mathbf{x}$ as follows:

$$\boldsymbol{A}_1\boldsymbol{x} \leq \boldsymbol{b}_1$$

(2-14)

where $\mathbf{A}_1$ is the Z×6Z matrix and $\mathbf{b}_1$ is the Z-sized vector below

$$\boldsymbol{A}_1 = \begin{pmatrix} \mathbf{1}_{1\times6} & \mathbf{0}_{1\times6} & \cdots & \mathbf{0}_{1\times6} \\ \mathbf{0}_{1\times6} & \mathbf{1}_{1\times6} & \cdots & \mathbf{0}_{1\times6} \\ \vdots & \vdots & \ddots & \vdots \\ \mathbf{0}_{1\times6} & \mathbf{0}_{1\times6} & \cdots & \mathbf{1}_{1\times6} \end{pmatrix}, \boldsymbol{b}_1 = N_0\mathbf{1}_{Z\times1}$$

(2-15)

with $\mathbf{1}_{m\times n}$ and $\mathbf{0}_{m\times n}$ indicating the m×n unit and zero matrix, respectively.

Furthermore, all turn vector elements must be null or positive, according to the convention specified in 1.1.

$$\boldsymbol{A}_2\boldsymbol{x} \leq \boldsymbol{b}_2$$

(2-16)

with $\mathbf{A_2}$ being the opposite of the 6Zx6Z identity matrix $\mathbf{I}_{6Z}$ and $\mathbf{b}_2$ the 6Z-sized null vector:

$$\boldsymbol{A}_2 = -\boldsymbol{I}_{6Z},\ \boldsymbol{b}_2 = \mathbf{0}_{6Z\times1}$$

(2-17)

For the winding to be symmetric, all the three phases must produce equal MMF fundamentals at any instant. In 1.3 it has been shown how this condition can be formalized with the following equation:

$$\boldsymbol{A}_3\boldsymbol{x} = \boldsymbol{b}_3$$

(2-18)

where, based on (1-35), $\mathbf{A}_3$ and $\mathbf{b}_3$ are the 4×6Z matrix and 4×1 vector below:

$$\boldsymbol{A}_3 = \begin{pmatrix} Re\{v_p^{-T}(\boldsymbol{K}_b - \boldsymbol{K}_a)\} \\ Im\{v_p^{-T}(\boldsymbol{K}_b - \boldsymbol{K}_a)\} \\ Re\{v_p^{-T}(\boldsymbol{K}_c - \boldsymbol{K}_b)\} \\ Im\{v_p^{-T}(\boldsymbol{K}_c - \boldsymbol{K}_b)\} \end{pmatrix}, \boldsymbol{b}_3 = \begin{pmatrix} 0 \\ 0 \\ 0 \\ 0 \end{pmatrix}$$

(2-19)

It is to be noted that, in the quadratic problem the winding vector $\mathbf{x}$ is treated as real, although its elements (which represent numbers of turns) should be actually constrained to be integers. In fact, the formulation of the same problem as an integer programming one would make the solution procedure much more difficult. On the other side, supposing that the number of turns N_{tooth} which can be wound around a tooth is sufficiently large, very little errors result from solving this problem as a real quadratic problem and then rounding the single elements of the solution vector $\mathbf{x}$ to determine the number of turns $N_{k,0}$, $N_{k,1}$, …, $N_{k,5}$.

The last constraint involves the MMF fundamental maximum value. As explained in 2.2, the objective function (2-12) expressed as the weighted sum of two objective functions is too sensitive even to little changes of *w (weight)*. Taking this into account, as discussed in 2.2, the maximum value of MMF fundamental for a slot-pole combination is achieved by a dual layer winding machine. In order to have a reduction of losses in the magnets, it is necessary to reduce the MMF fundamental. In other words, for a given slot-pole combination it is possible to evaluate the maximum fundamental of MMF $M_{fund,max}$ using double layer concentrated winding (star of slots). This value can be used to set the reduction of the MMF fundamental as a new constraint, using (2-8) in the following form:

$$rM_{fund,max}\cos\varphi_p = \left(\boldsymbol{c}_p^-\right)^T\boldsymbol{x},$$

$$rM_{fund,max}\sin\varphi_p = \left(\boldsymbol{s}_p^-\right)^T\boldsymbol{x},$$

(2-20)

where $0 < r \leq 1$ is the reduction coefficient and $\boldsymbol{\varphi_p}$ relates to the initial phase of the MMF fundamental waveform.

This condition can be formalized through the following equation:

$$\boldsymbol{A_4 x} = \boldsymbol{b_4}(\varphi_p)$$

(2-21)

where

$$\boldsymbol{A_4} = \begin{pmatrix} (\boldsymbol{c_p^-})^T \\ (\boldsymbol{s_p^-})^T \end{pmatrix}$$

$$\boldsymbol{b_4}(\varphi_p) = rM_{fund,max} \begin{pmatrix} cos\,\varphi_p \\ sin\,\varphi_p \end{pmatrix}$$

(2-22)

with $\boldsymbol{\varphi_p}$ being a generic phase angle between 0 and 2π.

The overall quadratic problem can be formalized as:

$$\text{minimize} \quad P_{loss}(\varphi_p) = \boldsymbol{x}(\varphi_p)^T \left[\sum_{n=1}^{\infty} (p_n^+ \boldsymbol{Q_n^+} + p_n^- \boldsymbol{Q_n^-}) \right] \boldsymbol{x}(\varphi_p)$$

$$\text{subject to}$$

$$\mathbf{A}_1 \boldsymbol{x}(\varphi_p) \leq \boldsymbol{b}_1$$

$$\boldsymbol{A}_2 \boldsymbol{x}(\varphi_p) \leq \boldsymbol{b}_2$$

$$\boldsymbol{A}_3 \boldsymbol{x}(\varphi_p) = \boldsymbol{b}_3$$

$$\boldsymbol{A}_4 \boldsymbol{x}(\varphi_p) = \boldsymbol{b}_4(\varphi_p)$$

(2-23)

To make the notation simpler, the dependency on $\boldsymbol{\varphi_p}$ will be omitted. The problem (2-23) is a parametric function of the unknown angle $\boldsymbol{\varphi_p}$, that represents the phase of MMF fundamental. Its solution therefore provides a the minimum magnet losses $P_{\text{loss}}(\boldsymbol{\varphi_p})$ as a function of $\boldsymbol{\varphi_p}$ ranging between 0 and 2π. The solution of (2-23) leads to identify the minimum losses in the magnets P_{loss} with a

MMF fundamental amplitude $M_{\text{fund,max}}$, which can be attained for the given slot-pole combination, multiplied by the reduction coefficient r. However, as it will be shown later on, the problem (2-23) does not have, in general, a unique solution. This means that the same losses in the magnet P_{loss} with MMF fundamental amplitude $rM_{\text{fund,max}}$ can be obtained with different winding layouts that satisfy the symmetry and feasibility constraints. However, if we fix a certain angle $\boldsymbol{\varphi_p}$, this solution becomes unique. In order to know the optimal solution, it is necessary to find φ_{opt}, i.e. the phase which minimizes P_{loss}.

The result of the optimization problem (2-23) fixing $\boldsymbol{\varphi_p}$ is an optimal winding vector **x.** This vector completely and univocally describes the over winding structure as seen in (1-16).

2.4. Optimal phase

As explained in 2.3, the quadratic optimization problem is a parametric problem, function of $\boldsymbol{\varphi_p}$, the phase of MMF fundamental. This quadratic problem has been applied to different slots - poles configurations in order to verify the reduction potentials in terms of losses in the magnets. For each configuration, the maximum amplitude of MMF fundamental ($M_{\text{fund,max}}$) has been preliminary computed, then the optimization (2-23) has been solved, imposing a reduction coefficient from 1 to 0.95.

For each reduction coefficient the optimization problem (2-23) has been run setting $\mathbf{0 < \varphi_p < 2\pi}$. The results are presented in the following.

The polar graphs provided next represent the losses in the magnets as a function of FMM fundamental reduction and the MMF phase angle. In particular, as explained in Fig. 7 every single symbol represents a winding vector (different distribution in terms of turns belonging to a phase). The color and the type of symbols is linked to r, thus to the reduction in the MMF fundamental.

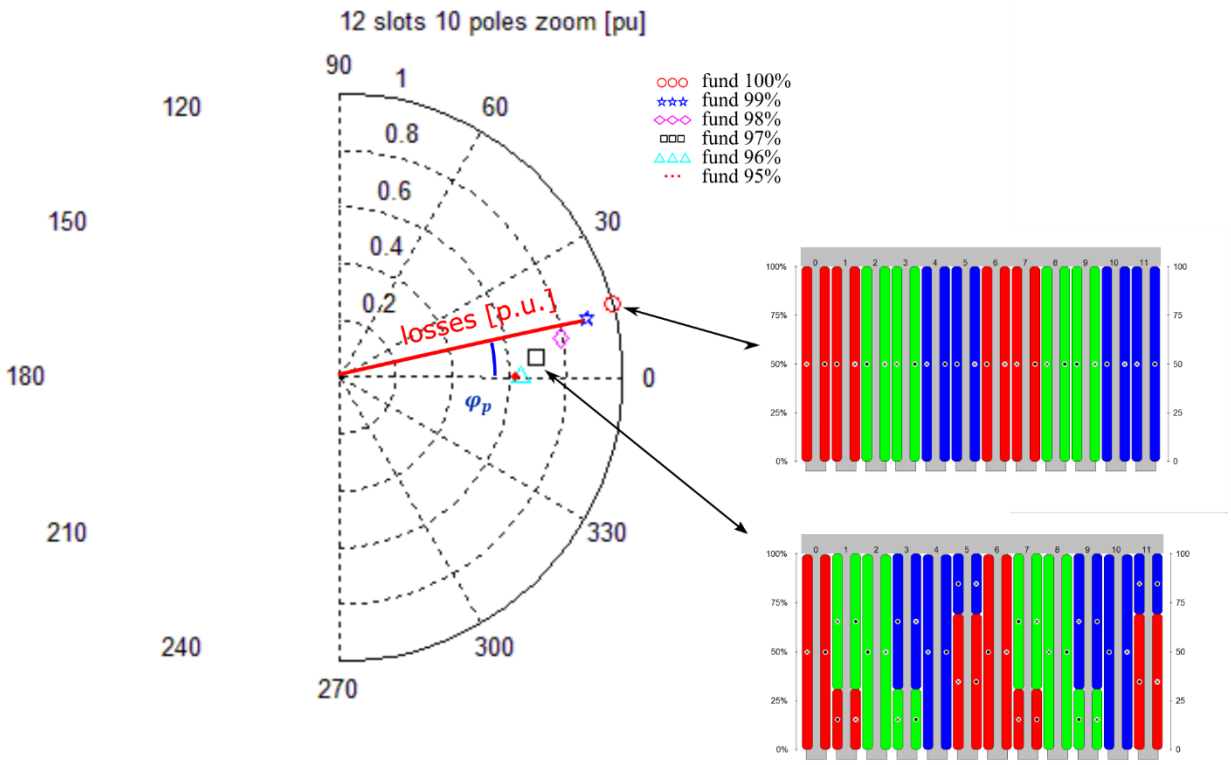

Fig. 7 Example of polar representation

In the Fig. 7, it is possible to see five different windings: the red circle represents the classical dual-layer topology, designed through the "star of slots" methodology. This winding, for each slots-poles configuration, has the maximum MMF fundamental as already mentioned in 2.2, and it is the optimization reference (indeed has unitary distance from the center of the graph in Fig. 7).

The distance of symbols from the origin is proportional to the losses in the magnets produced by the winding. Instead, the angular coordinates indicates the MMF fundamental phase angle of the winding MMF fundamental (a problem parameter, as seen in (2-23)).

This representation has been used in order to explore the possibilities of improving the performance in terms of losses in the magnets for various configurations, focusing on fractional slot with $¼<q<1/2$, where q is the number of slots per pole per phase. Obviously, in polar coordinates, for a certain MMF fundamental amplitude, the best solutions are located with minimal distance from the origin. The diagrams in Fig. 8 (a, b, c, d) are polar representations for 9-slots configurations, that is (slots-poles): 9-6(a), 9-8 (b); 9-10(c); 9-12(d).

The first characteristic which can be noticed is that there are two different behaviors in terms of losses reduction. There are “reducible combinations” (Z =9, P=8 Fig. 8 (b) and Z=9 P=10 Fig. 8 (c)) which have an important reduction of losses (10%) together with a quite small reduction of MMF fundamental (2%). However, there are also “unreducible combinations” (Z =9, P=6 Fig. 8 (a) and Z=9 P=12 Fig. 8 (d)) where the optimization is not effective. In addition, problem (2-23) does not have any solution for some values of $\varphi_{p.}$

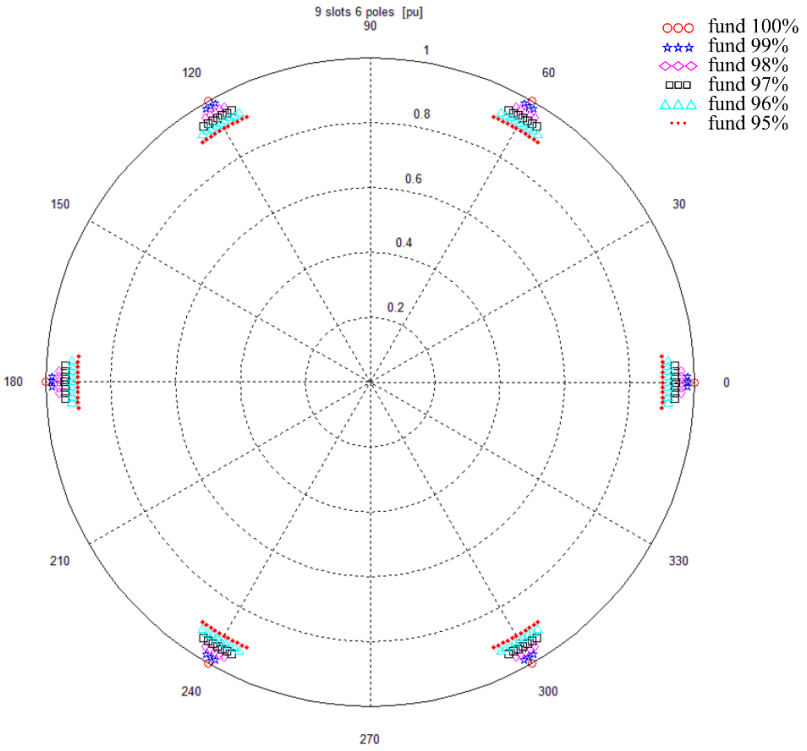
9 slots 6 poles [pu]
fund 100%
fund 99%
fund 98%
fund 97%
fund 96%
fund 95%
90
1
60
120
0.8
0.6
150
30
0.4
0.2
180
0
210
330
240
300
270

(a)

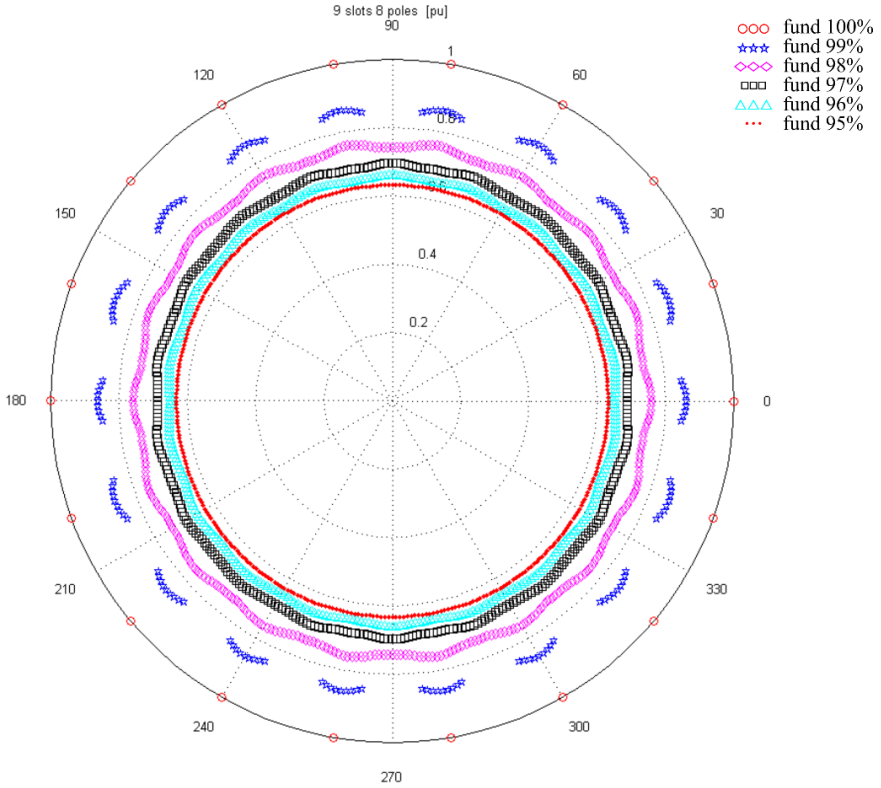
9 slots 8 poles [pu]
fund 100%
fund 99%
fund 98%
fund 97%
fund 96%
fund 95%
90
1
120
60
0.8
0.6
150
30
0.4
0.2
180
0
210
330
240
300
270

(b)

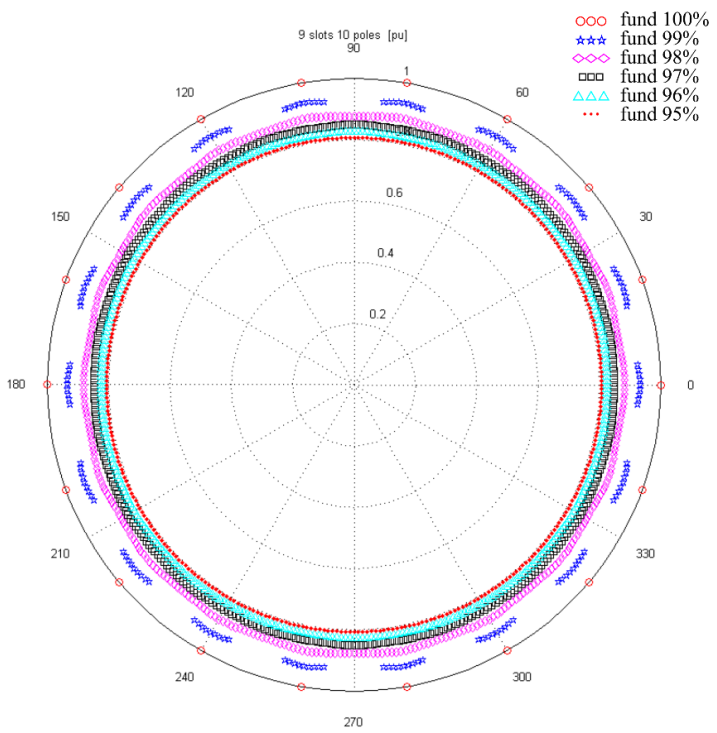

(c)

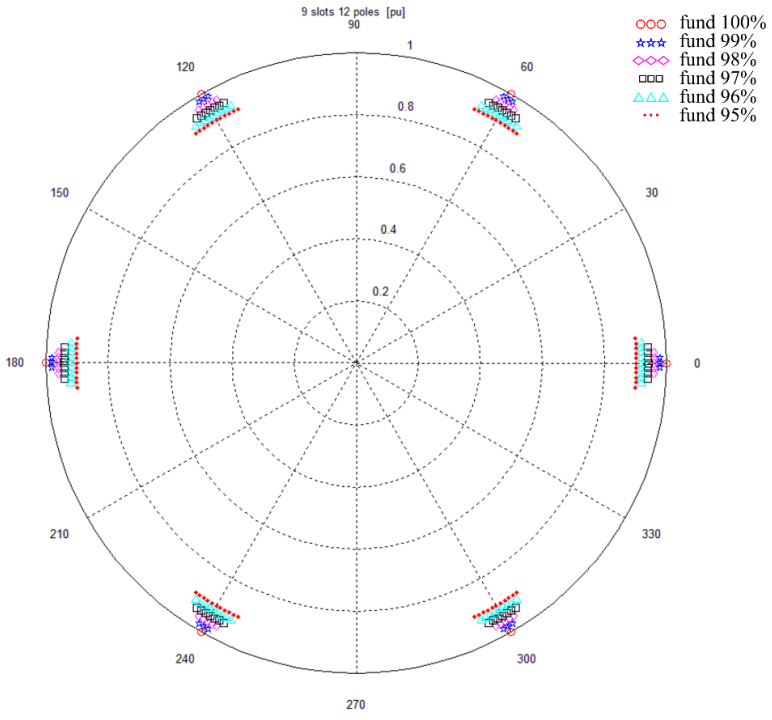

(d)

Fig. 8 polar representation of losses in magnets, different phases and reductions of MMF fundamental (9 slots, and poles = 6,8,10,12)

The polar representation of the "reducible combinations" has a periodicity, as illustrated in Table 1. This table indicates that when r=1 is used, the problem does not always have a solution since the maximum value of MMF fundamental, which is a constraint in this case, cannot be achieved for all phase φ_p values.

The maximum value of MMF fundamental can be achieved when the MMF waveform has its maximum value aligned with a slot; in this way it is possible to have Z points with maximum MMF if the number of slots is even, 2 x Z if the number of slots is odd. The periodicity is then:

$\frac{2\pi}{Z}$ if Z is even

$\frac{\pi}{Z}$ if Z is odd.

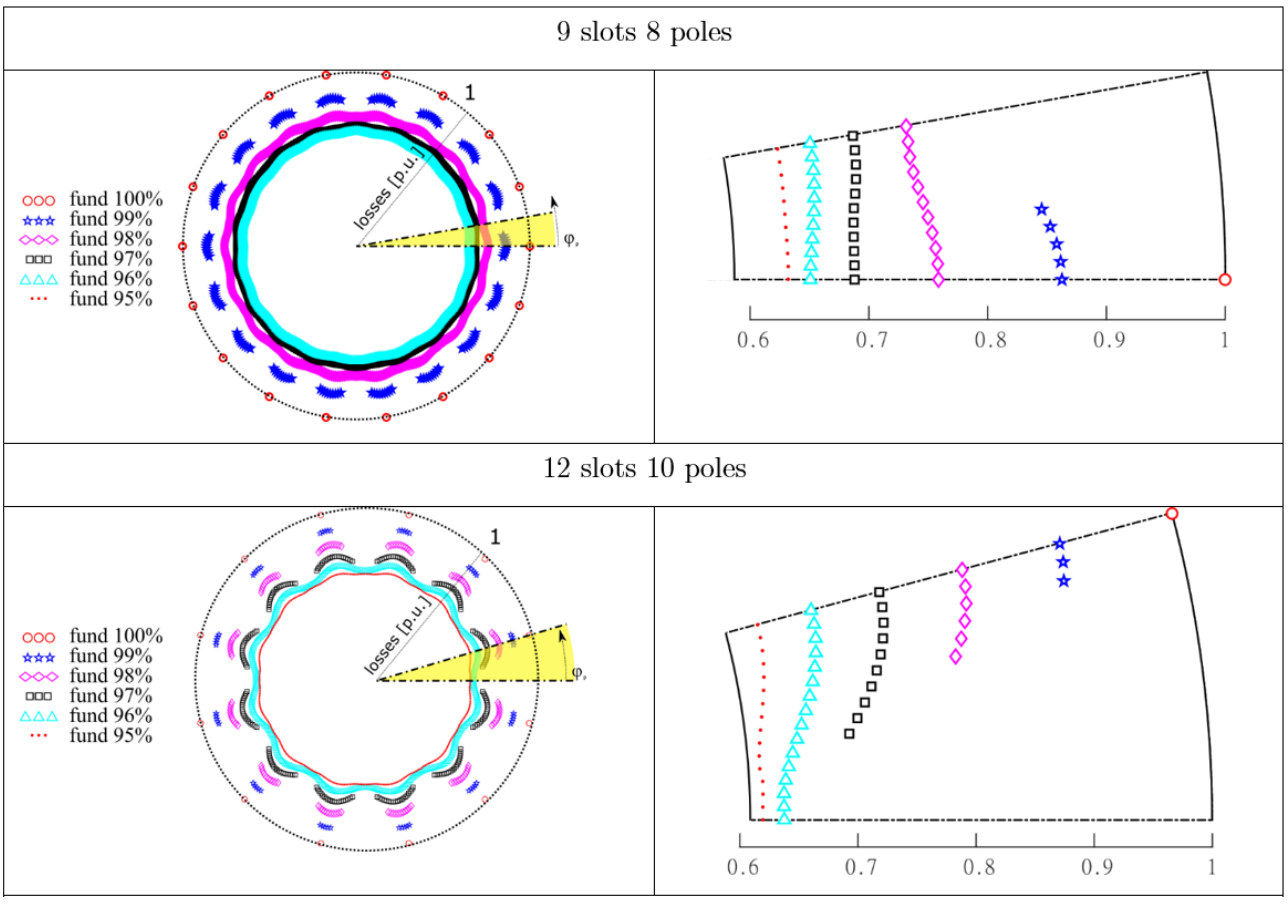

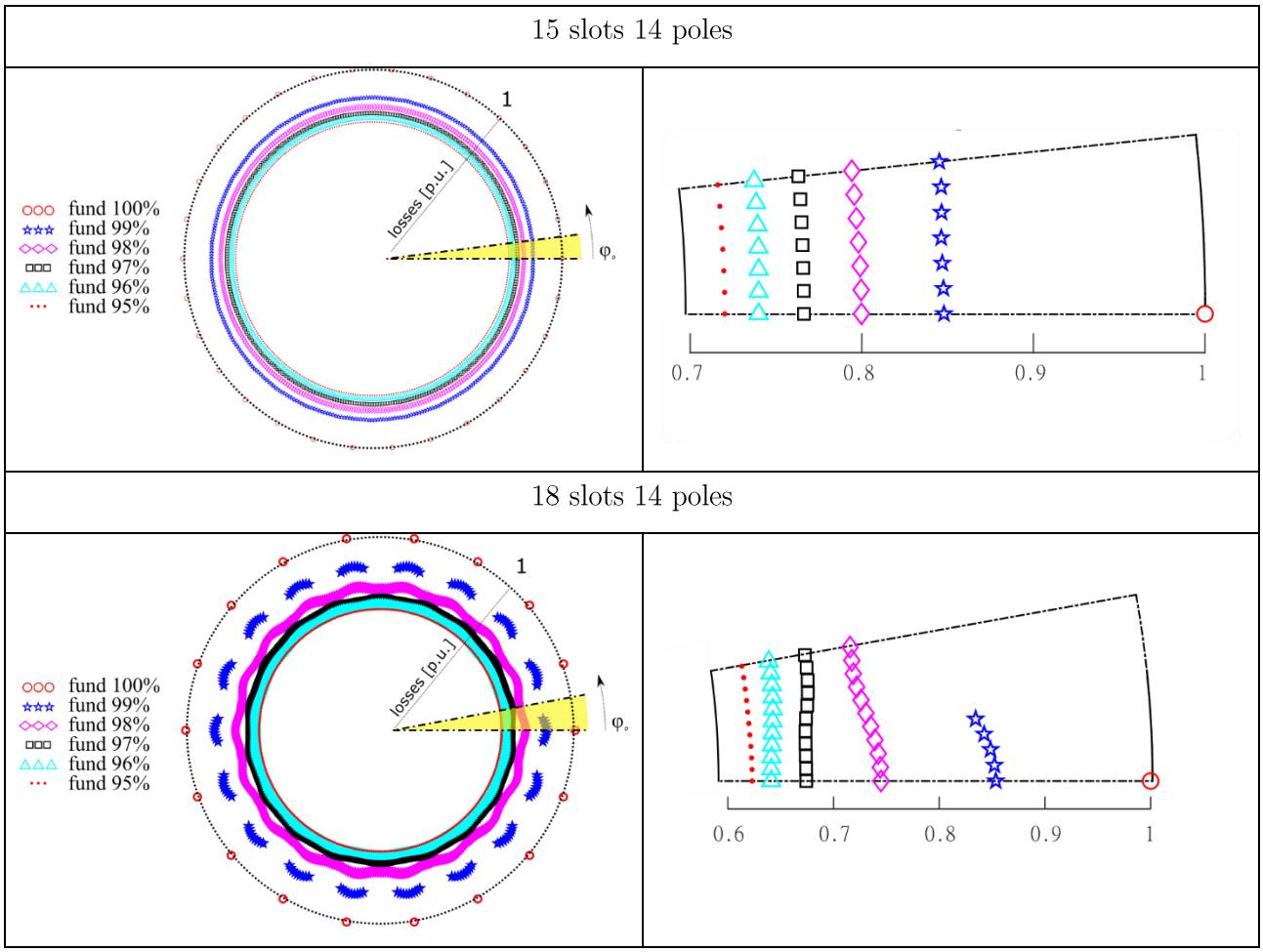

Table 1 polar plot- losses in the magnets

For each variation of r, the symbol closer to the origin represents the optimal winding for that particular MMF reduction coefficient.

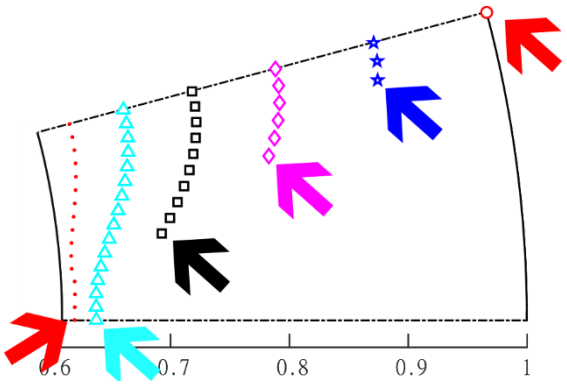

Fig. 9 optimal design for each fundamental reduction

In the next sections, the best topologies will be considered in order to define a pareto front for the optimization.

2.5. Reducible and unreducible combinations

As mentioned in the previous chapter, several ways have been proposed by different authors for FSCW design optimization using multi-layer configurations. In order to formulate the problem in a general and comprehensive manner, we can observe that all the approaches assume that the FSCW configurations can be univocally described by a set of variables, which we can think of collecting into the vector $\mathbf{x}$. The elements of $\mathbf{x}$ generally include the information of how many turns are wound on all single teeth and of what phase these turns belong to [35]. The generic MMF space harmonic of order ν can be expressed as a function of $\mathbf{x}$ as $f_\nu(\mathbf{x})$ so that the fundamental will be then given by $f_p(\mathbf{x})$, p being the number of pole pairs. At this point, at least two objective functions, depending on $\mathbf{x}$, need to be introduced. One of them consists of maximizing the magnitude of the MMF fundamental $f_p(\mathbf{x})$ the other consists of minimizing the negative effects (e.g., permanent-magnet losses, torque ripple, UMP, etc.) caused by MMF space harmonics different from the fundamental. As it will be pointed out in the following, each negative effect depends on different sets of space harmonics. For instance, it is well known that permanent magnet losses are mainly affected by subharmonics, whose order n is such that $n < p$, but this is not the case for other kinds of parasitic phenomena which may be desirable to reduce. Finally, constraints must be imposed so that the design variable $\mathbf{x}$ represents a FSCW that is physically manufacturable as a symmetrical three-phase winding. Typical manufacturability constraints relate to the maximum number of turns that can be accommodated in stator slots and the symmetry of the windings is guaranteed by the MMF fundamentals produced by the three phases being equal and shifted by 120 electrical degrees apart [35] [17].

With a suitable definition of the design variable $\mathbf{x}$, manufacturability and symmetry constraints can be represented through a linear relationship like $\mathbf{Ax}=\mathbf{b}$, where $\mathbf{A}$ is a suitable constant rectangular matrix and $\mathbf{b}$ a constant vector [17].

The general design optimization problem can be thus formulated as follows:

$$\text{maximize } \left[f_p(\mathbf{x})\right]^2, \quad \text{minimize } \sum_{\nu \in \mathcal{H}} c_\nu [f_\nu(\mathbf{x})]^2$$

$$\text{subject to } \mathbf{Ax} = \mathbf{b}$$

(2-24)

where $\mathcal{H}$ is a suitable set of the harmonic orders and c_ν are constant weight coefficients. Both $\mathcal{H}$ and c_ν change depending on the adverse effect that needs to be minimized. If only the first objective function (maximization of the fundamental) is considered, the optimization problem yields the same winding layout as the star-of-slot method [17]. In the following, we shall call $\mathbf{x}_0$ the design vector variable that identifies the star-of-slot winding layout.

It may be worth observing that the MMF space harmonics produced by a FSCW are not independent of one another.

In [17] it has been proven that the amplitude of the ν^{th} order MMF space harmonic can be expressed as:

$$|f_\nu(\mathbf{x})| = |\mathbf{m}_\nu^t\, \mathbf{x}|$$

(2-25)

Where $\mathbf{x}$ is 6Z-sized vector (e.g., three phases case) which univocally determines the winding layout, superscript t denotes transposition and the 6Z-sized vector $\mathbf{m}_\nu$ is defined as follows:

$$[\mathbf{m}_\nu]_j = C_\nu e^{i\left[-\frac{\pi}{3}\text{mod}(j-1,6)\pm\nu\frac{2\pi}{Z}\text{floor}\left(\frac{j-1}{6}\right)\right]} \qquad \text{with } j=1,2,..,6Z$$

(2-26)

where: C_ν is a constant; i is the imaginary unit; mod(a,b) is the function that returns the reminder on dividing a by b; floor(a) is the function that return the largest integer less than or equal to a. From (2-25) and (2-26) it is apparent that, if two space harmonic indices ν_1 and ν_1 satisfy

$$\nu_1 \pm \nu_2 = kZ, \;\; k \in \mathbb{Z}.$$

(2-27)

For the some integer k, where Z is the number of slots, the ratio between the two relevant space harmonic amplitudes will be

$$|f_{\nu_1}(\mathbf{x})|/|f_{\nu_2}(\mathbf{x})| = |C_{\nu_1}|/|C_{\nu_2}|$$

(2-28)

for any $\mathbf{x}$, i.e. for any winding design. In other words, two space harmonics whose orders satisfy (2-27) are such that their ratio cannot be changed by acting on the winding layout.

In fact, two MMF harmonics having orders ν_1 and ν_2 have proportional amplitude regardless of the winding layout, i.e.

$$f_{\nu_1}(\mathbf{x}) = const \times f_{\nu_2}(\mathbf{x}) \quad \forall \mathbf{x},$$

(2-29)

if the condition (2-27) holds.

In particular, the harmonics whose order ν is such that

$$\nu \pm p = kZ, \quad k \in \mathbb{Z}$$

(2-30)

are proportional to the fundamental. This implies that no kind of optimization (regardless of the algorithm used) can be effective in reducing these harmonics without reducing the fundamental exactly by the same amount.

For instance, Fig. 10 shows the MMF harmonic spectrum of the dual-layer 9 slot – 8 pole FSCW (corresponding to the design vector variable $\mathbf{x}_0$) obtained with the star-of-slot method. Space harmonics can be classified into three groups, respectively indicated by green and red lines and highlighted in yellow. For any winding configuration $\mathbf{x}$ resulting from the optimization, all the harmonics belonging to the same group are bound to remain proportional to one another, i.e. they can be reduced or increased by the same amount. In particular, the harmonics highlighted in yellow are “linked” to the fundamental (in the sense that they vary proportionally to it).

This connection between harmonic orders will be shown to differently affect the winding optimization task (possibly making it unfeasible) depending on the objective function being chosen.

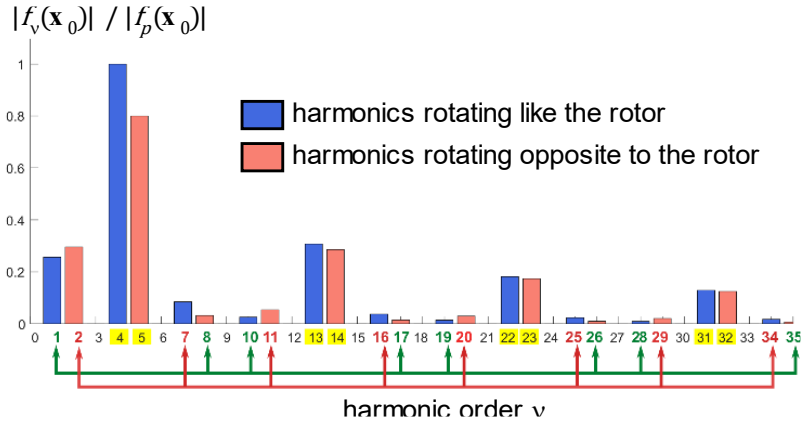

Fig. 10 MMF harmonic spectrum of the dual-layer 9 slot – 8 pole FSCW designed according to the star-of-slot method. Harmonic amplitudes are in per unit of the fundamental (for which v=p)

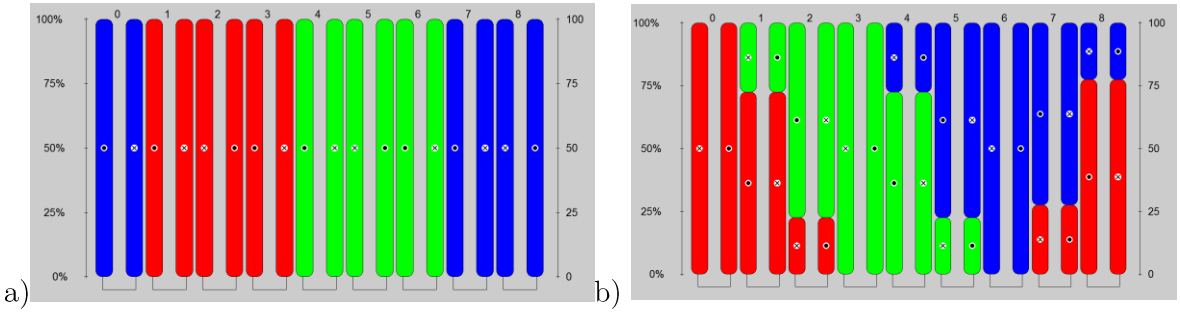

Fig. 11 Different optimization results for a 9 slot – 8 pole FSCW to reduce winding losses, on the left 100% MMF fundamental, on the right 97%.

Fig. 12 shows the harmonic spectrum of the standard 9 – 8 configuration (9 slots, 8 poles) designed through "star of slots" method, dual layer winding (Fig. 11 (a)). It can be seen that there are sub-harmonics and not all the harmonics are linked to the fundamental, according to (2-30).

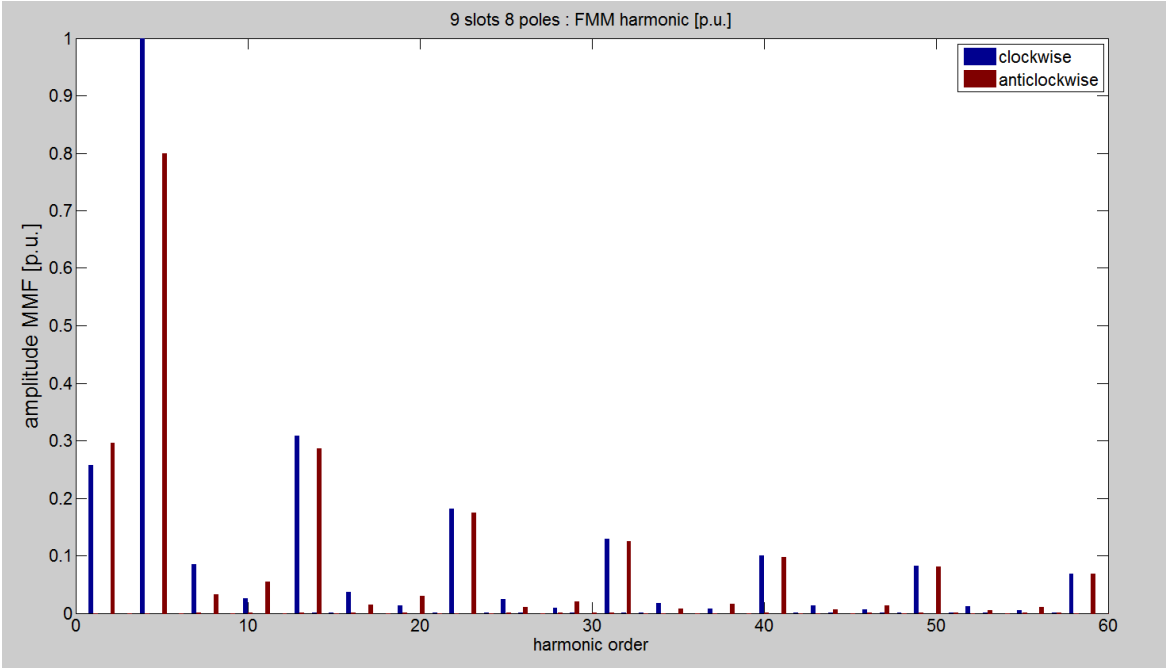

Fig. 12 Space harmonic spectrum of 9 slots 8 poles configuration

Indeed, Fig. 13 shows that the reduction is possible for the harmonic that are not linked to the fundamental. Each color represents the reduction with 1% fundamental MMF reducing. Harmonics linked to the fundamental are reduced by the same amount (yellow columns are the harmonic content of optimization results for a 9 slot – 8 pole FSCW to reduce winding losses, imposing a fundamental equal to 97% (Fig. 11 (b)).

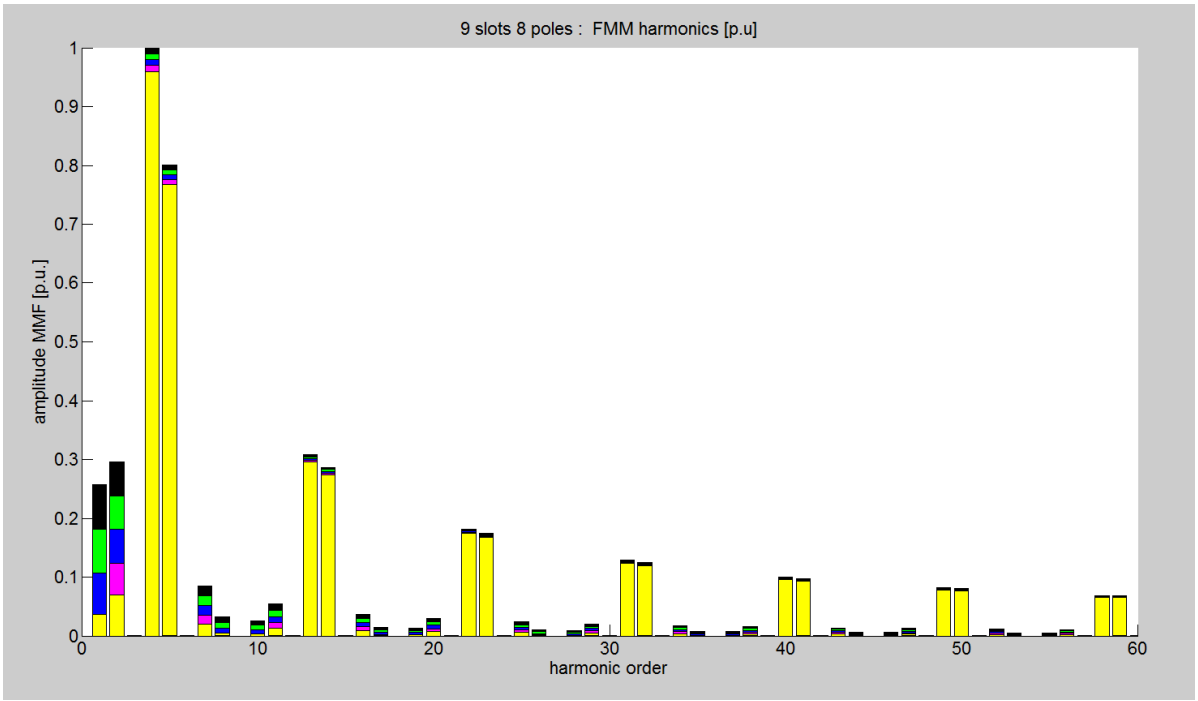

Fig. 13 Harmonic spectrum reduction for 9 slots 8 poles configuration

Fig. 14 shows the harmonic spectrum of 9 slot 6 slot layout, where only harmonics linked to the fundamental are produced by the stator winding. This is an unreducible configuration; indeed (Fig. 15) all harmonics can be reduced by the same amount.

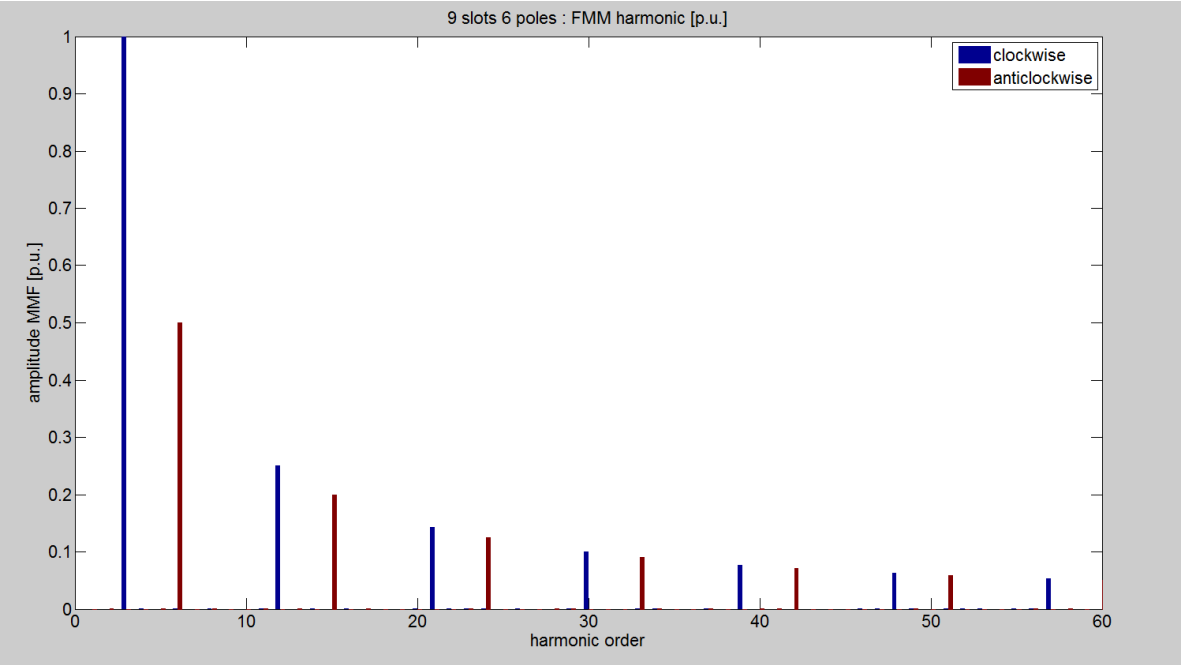

Fig. 14 Harmonic spectrum of 9 slots 6 poles configuration

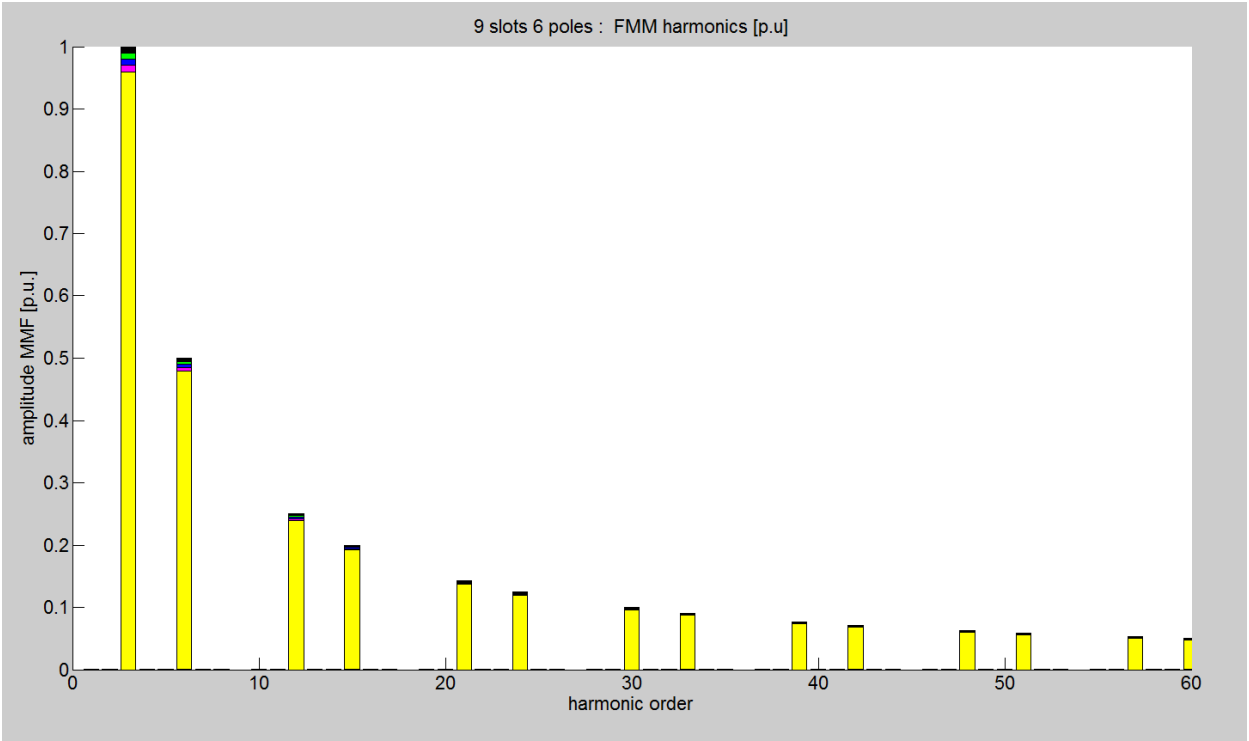

Fig. 15 Harmonic spectrum reduction for 9 slots 6 poles configuration

Table 2 provides an overview of the most common slot-pole combinations for FSCWs having acceptable winding factors (i.e. with $Z \cong 2p$) in terms of winding optimization effectiveness. Cells with symbol "—" identify configurations which cannot be designed in a symmetrical manner according to classical rules [6]. For feasible slot-pole configurations, "v" identifies those for which a design optimization is effective because it is possible to reduce subharmonics more than the fundamental, while "×" indicates those for which optimization is ineffective because the subharmonics are linked to the fundamental according to (2-30). For the latter combinations it would make no sense to use an optimized multi-layer design where both the fundamental and subharmonics are reduced by the same factor k because the same performance in terms of permanent magnet loss and output torque could be obtained with a conventional dual-layer design (built with the star-of-slot method) by simply reducing the current by the factor k; hence, the manufacturing complications associated with the multi-layer design would not have any justification.

		Number of poles, 2p												
		2	4	6	8	10	12	14	16	18	20	22	24	26
Number of slot, Z	3	x	x											
	4													
	5													
	6		x	–	x									
	7													
	8													
	9			x	v	v	x							
	10													
	11													
	12				x	v	–	v	x					
	13													
	14													
	15					x	v	v	v	v	x			
	16													
	17													
	18						x	v	v	–	v	v	x	

Table 2 Slot-pole combinations for which design optimization aimed at magnet loss reduction is effective (V) or ineffective (X)

2.6. Pareto fronts comparisons

The optimization is intrinsically a double objective function problem, even defining one object as a constraint (2-23). As written in 2.2, the classical windings designed by "star of slots" method produce maximum torque but also maximum losses in terms of eddy currents in the magnet. When losses are reduced thanks to multilayer winding, the fundamental of MMF is inevitably reduced. Therefore, there are infinite optimal solutions and the best way to represent these solutions is a pareto front.

As mentioned in 2.4, in order to define a pareto front, there is a need to select the best winding in terms of losses in the magnets, for each reduction of MMF fundamental. In other words, it is necessary to consider only the windings indicated by arrows in Fig. 9, taking into account the optimal φ_p.

Fig. 16 and Fig. 17 show the Pareto front for the optimization process, confirming that a very significant magnet loss reduction can be achieved with a small MMF fundamental decrease. This confirms the optimization effectiveness.

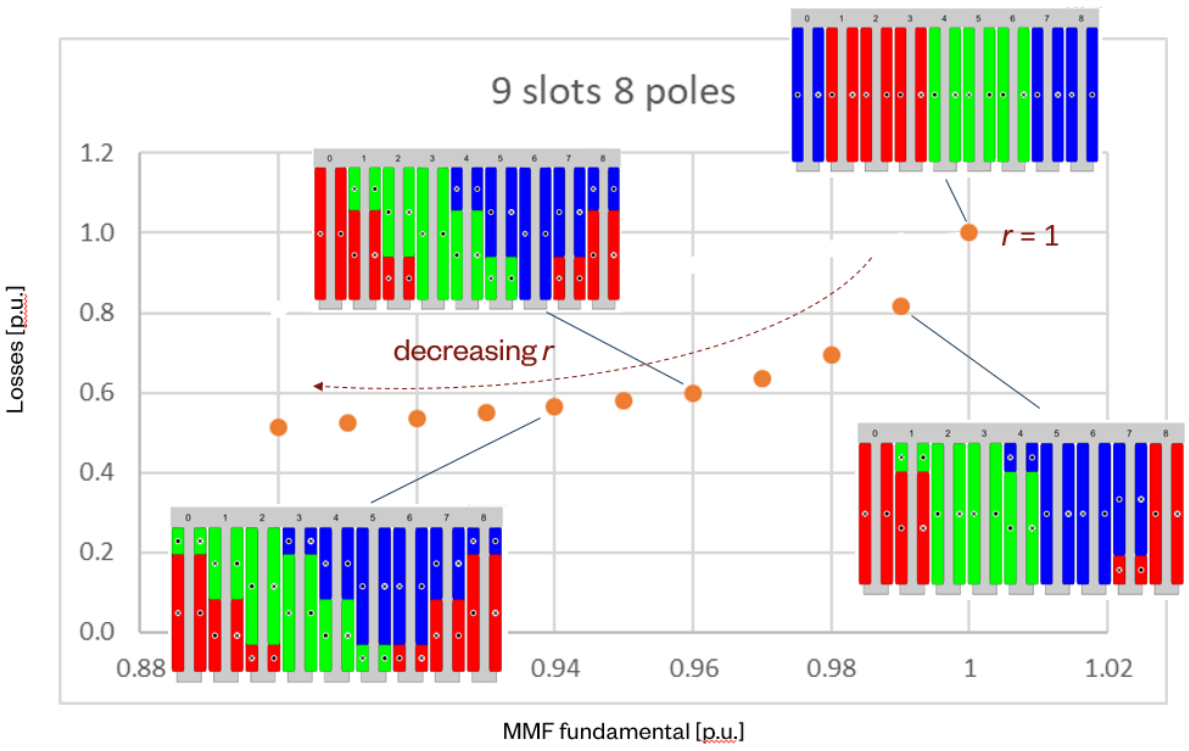

Fig. 16 pareto front for configuration 9,8

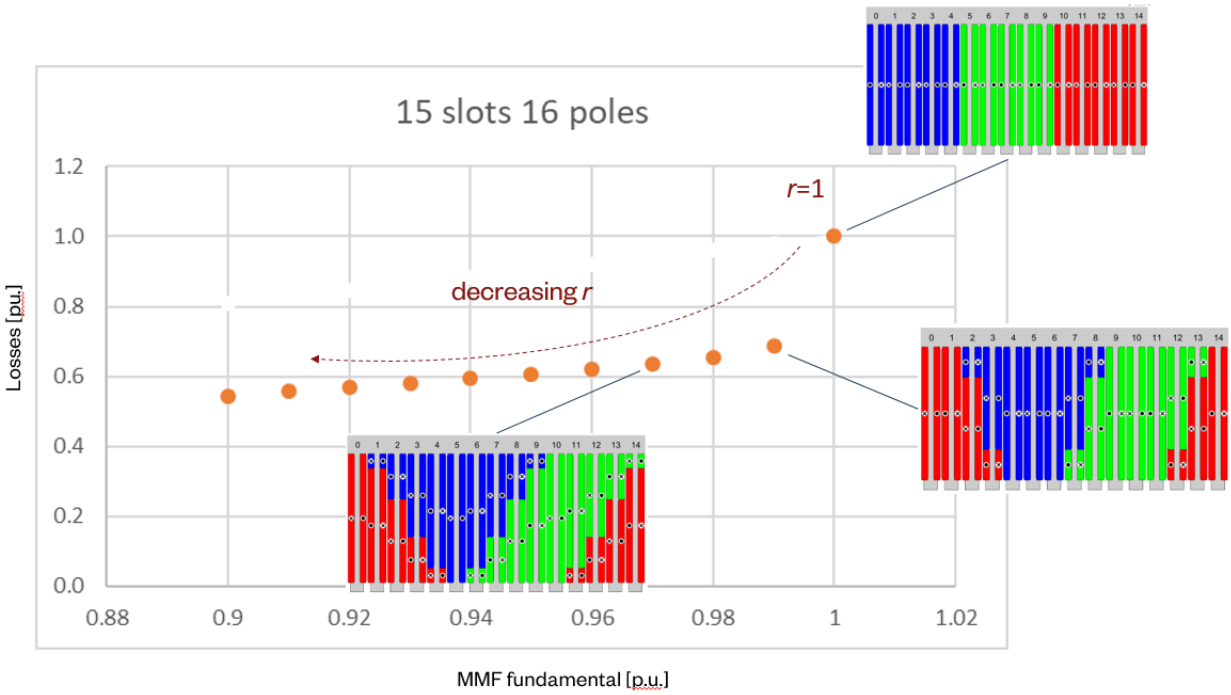

Fig. 17 pareto front for configuration 15,16

As known, the losses produced by eddy currents in the magnets are also function of the current flowing through the winding; however, reducing the current will decrease the MMF and the torque. With the aim of knowing the real improvement obtained by optimization, the loss reduction (and torque reduction) caused by a decrease of current for a "Star of slot" winding has been compared to the losses reduction caused by changing the winding arrangement with the same current supply. In Table 3 many configurations are considered: black lines are losses as a function of MMF fundamental in case of reducing current in a "star of slot" winding, orange points represent losses and MMF amplitude pairs obtained through winding optimization.

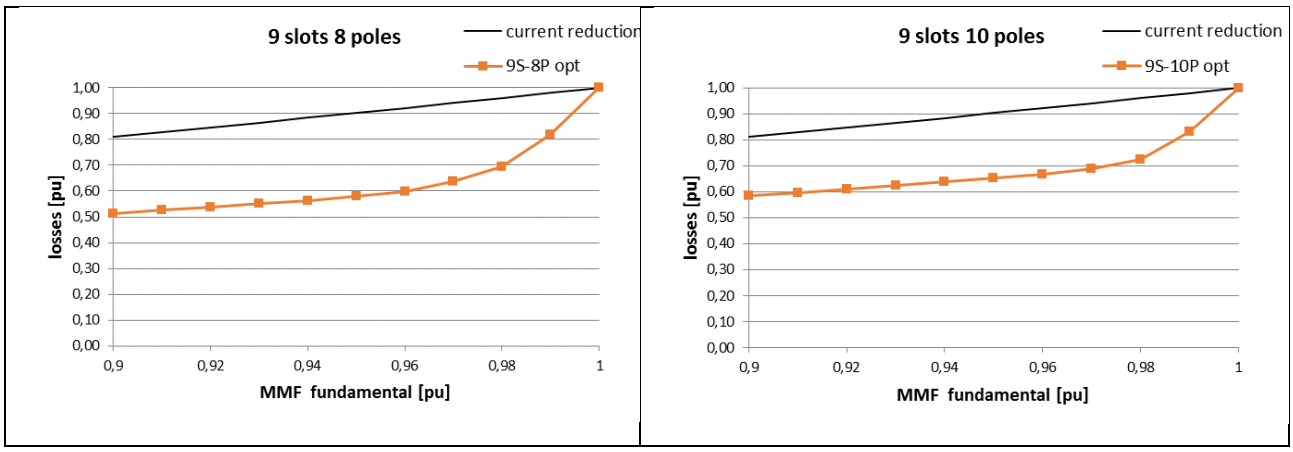

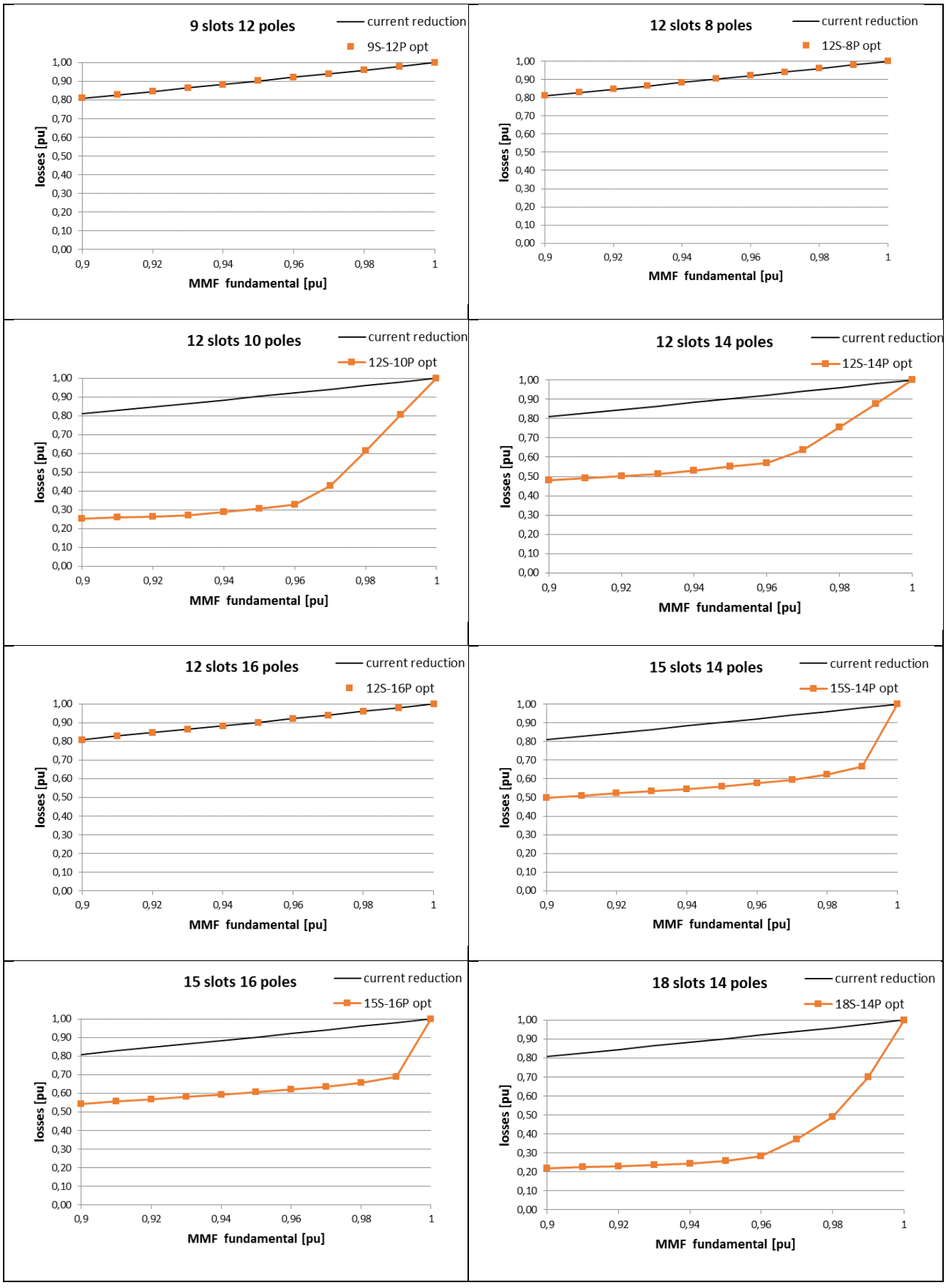
9 slots 12 poles
current reduction
9S-12P opt
losses [pu]
MMF fundamental [pu]
12 slots 8 poles
current reduction
12S-8P opt
losses [pu]
MMF fundamental [pu]
12 slots 10 poles
current reduction
12S-10P opt
losses [pu]
MMF fundamental [pu]
12 slots 14 poles
current reduction
12S-14P opt
losses [pu]
MMF fundamental [pu]
12 slots 16 poles
current reduction
12S-16P opt
losses [pu]
MMF fundamental [pu]
15 slots 14 poles
current reduction
15S-14P opt
losses [pu]
MMF fundamental [pu]
15 slots 16 poles
current reduction
15S-16P opt
losses [pu]
MMF fundamental [pu]
18 slots 14 poles
current reduction
18S-14P opt
losses [pu]
MMF fundamental [pu]

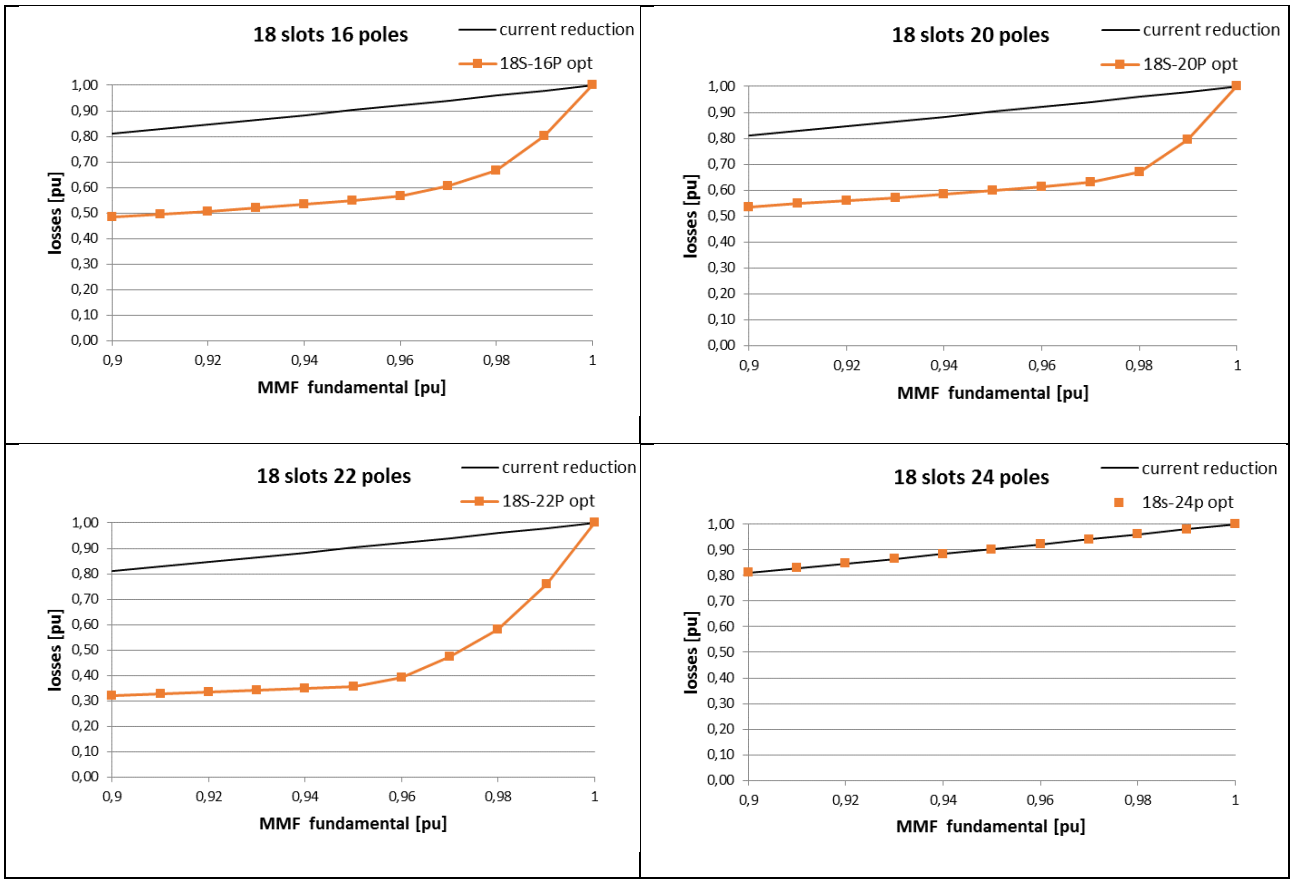

Table 3 Pareto fronts

In the examples listed in Table 3 the difference is clarified between "reducible" and "unreducible" combinations (explained in 2.5). In case of "Unreducible" combinations it is not possible to reduce the losses more than they can be reduced by lowering the current in the star of slot winding.

2.7. Genetic optimization approach

In (2-23) the dual objective problem has been formalized as a single objective problem. Thus, the maximization of MMF fundamental has been turned into a constraint. In particular, this constraint has been assumed equal to its maximum possible value (corresponding to the dual-layer standard star-of-slot winding) and it has been decreased of steps of 1%. In order to be rigorous, it is necessary to prove that imposing a discrete reduction is not a limitation for the optimization. In other words, it is

not guaranteed that there exists a better solution of (2-23) in terms of pareto front, imposing another value of reduction (e.g., r=0.995).

In order to solve this uncertainty, a completely independent method has been used to solve this type of problem, i.e. a genetic algorithm has been adopted. A genetic algorithm is a method for solving both constrained and unconstrained optimization problems based on a natural selection process that mimics biological evolution. The algorithm repeatedly modifies a population of individual solutions. In this case the variation of MMF fundamental is totally a free variable. Fig. 18 shows the comparison between the different independent methods. It is possible to see that the discrete value for the MMF fundamental constraint is not a limit for the optimization, as the pareto front independently obtained using genetic algorithms is practically coincident (or even worse) compared to that resulting from quadratic programming.

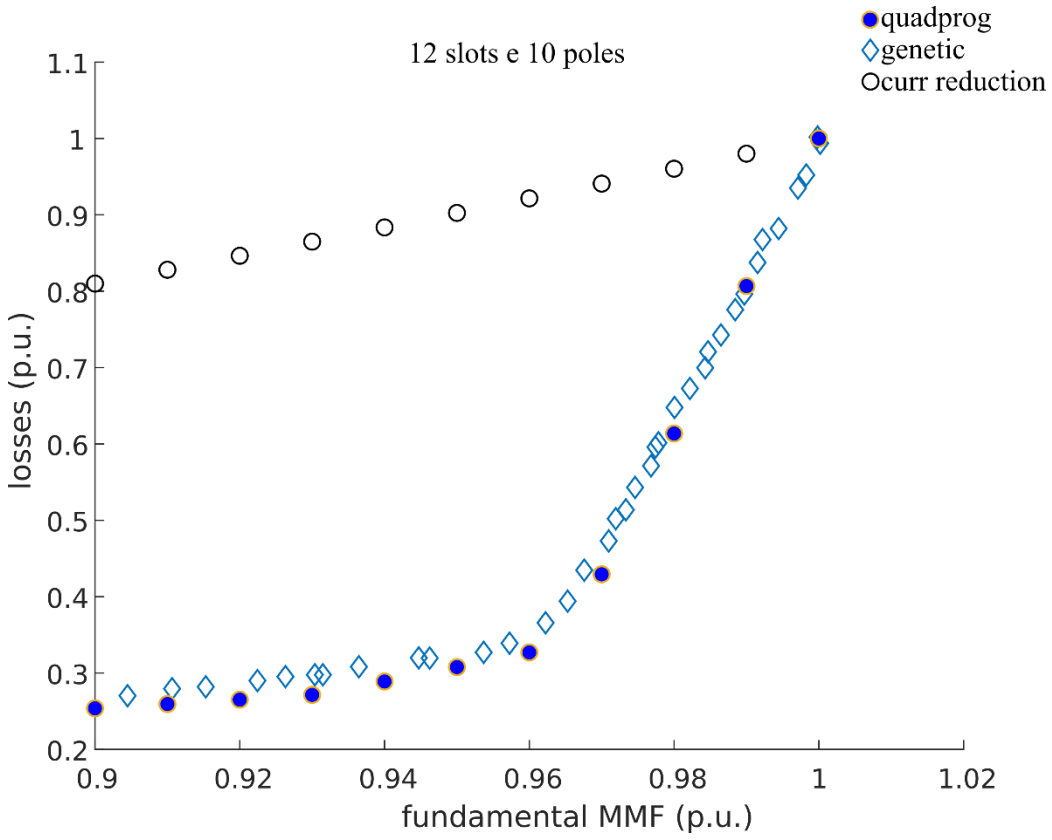

Fig. 18 Pareto front obtained by quadratic problem and genetic approach

3. Evolution of Star of slots method

Star of slots is a geometrical method to define the winding structure. In particular, it is very helpful for defining which phase each coil belongs to, especially in case of fractional slots windings, when the position of each phase in not so easy to select. This chapter will describe a modification of this method in order to design a multilayer winding, with a reduction of losses in the magnets due to MMF harmonics produced by the winding. This is presented as an elementary and easy-to-implement alternative to the quadratic programming approach for multi-layer winding layout optimization.

3.1. Star of slots

A balanced and symmetrical m–phase winding can be designed using an algorithm based on the star of slots method. In the follow paragraph this algorithm is explained.

The star of slots is divided into 2 x m sectors, each of them spanning $360/(2\ m)$ degrees. In Fig. 19 the case of 9 slots, 8 poles, 3 phases is represented. Two opposite sectors (identified by the same color) are assigned to each phase (blue arrows). The two sectors are referred to as positive (e.g., labeled A+) and negative sectors (e.g., labeled A-), and they are drawn on the star of slots with a displacement of 180 degrees, see Fig. 19.

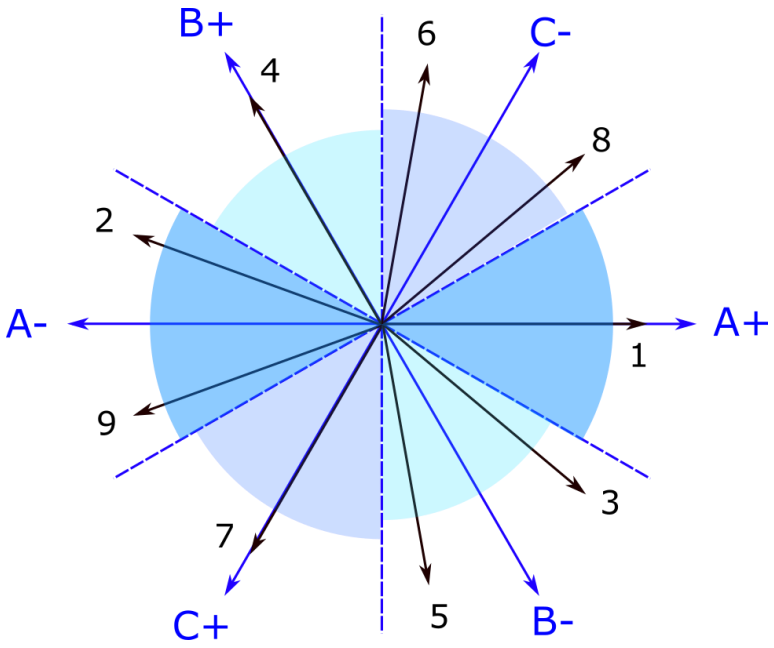

Fig. 19 Star of slots diagram, configuration 9 8.

Black spokes represent teeth shifted by the electrical angle. Given an initial position (es tooth 1 aligned to phase A+, second spokes (tooth 2) will be rotated by an angle

$$\alpha_{slot} = \frac{2\pi}{Z} p \qquad (3\text{-}1)$$

where Z is the number of slots and p is the number of pole pairs. This angle is the electrical angle between two adjacent teeth (Fig. 20).

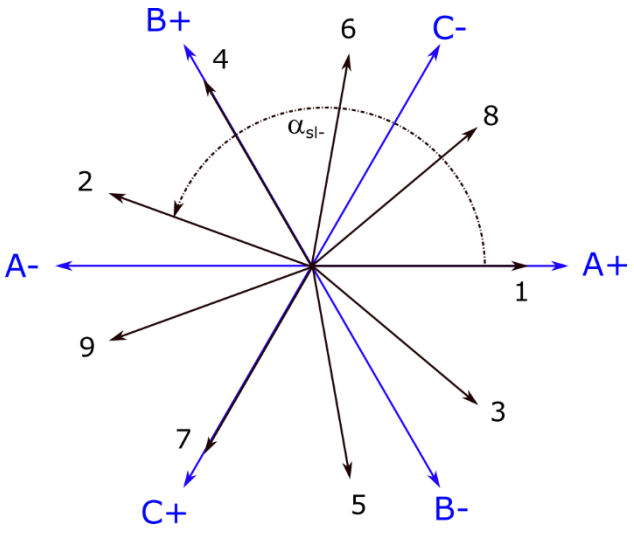

Fig. 20 Electrical angle between two adjacent slots

Once the phase sectors are drawn, Fig. 19, it is possible to assign the coil of each phase to the corresponding tooth. Taking into account slot 1, the corresponding spoke has the same position as the blue spoke A+. It means that around tooth 1 a coil connected to phase A has to be wound (conventional positive direction for the current). Spoke 2 are placed in A- sectors, so the coil has to be associated with the phase A- (conventional negative direction for the current, or in other word, the coil has to be wound in the opposite direction compared to tooth 1). So, each tooth (represented by a black spoke) has to be wound with the closer phase (blue spoke).

The star of slots method for 9-8 configuration produces the winding below.

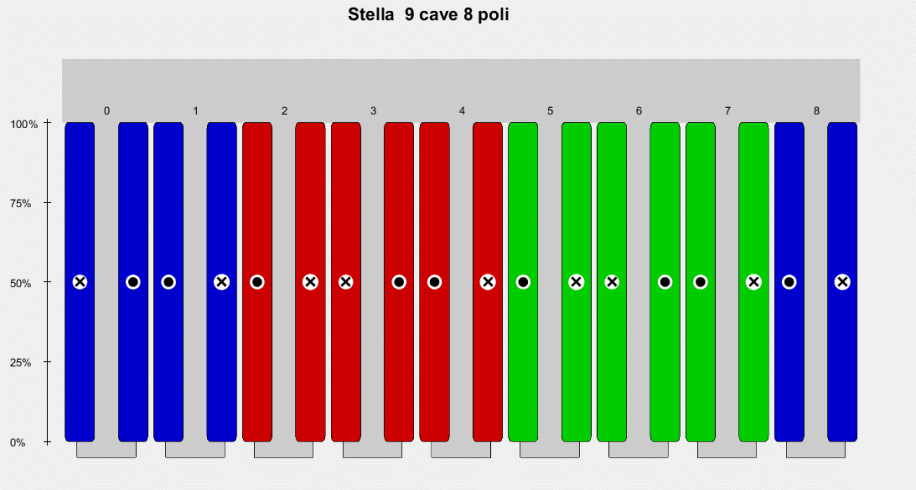

Fig. 21 9-8 configuration, produced by "star of slots" method

The greatest common divisor (GCD) between the slots number Z and the pole pairs p is defined as the machine periodicity t:

$$t = \mathrm{GCD}\{Z, p\} \tag{3-2}$$

The number of visible spokes in the star of slots is

$$N_{vs} = \frac{Z}{t} \tag{3-3}$$

If t=1 all spokes representing slots are visible while if t≠1 there are spokes superimposed. It means there is a periodicity.

3.2. Star of slots evolution

It is possible to design a multilayer topology by means an original evolution of the known star of slots obtaining a balanced and symmetrical winding with a reduction of losses in the magnet.

The main idea is to split coils when the corresponding spokes in the star of slot diagram are not aligned with the phase spokes. For instance, Fig. 22, referring to a 9 slots 8 poles configuration, a single coil wound around tooth 1 is associated with phase A+, while around tooth 2 there are two different coils. One coil is associated with A- and the other with B+. The ratio between turn will be inversely proportional to the angle. Thus:

$$\frac{N_{B+,2}}{N_{A-,2}} = \frac{\alpha_{2b+}}{\alpha_{2a-}}$$

where $N_{b+,2}$ is the number of turns wound around tooth 2 supplied by phase B+ and $N_{b+,2}$ is the number of turns wound around tooth 2 belonging to A-. α_{2b+} e α_{2a-} are the angles described in Fig. 22.

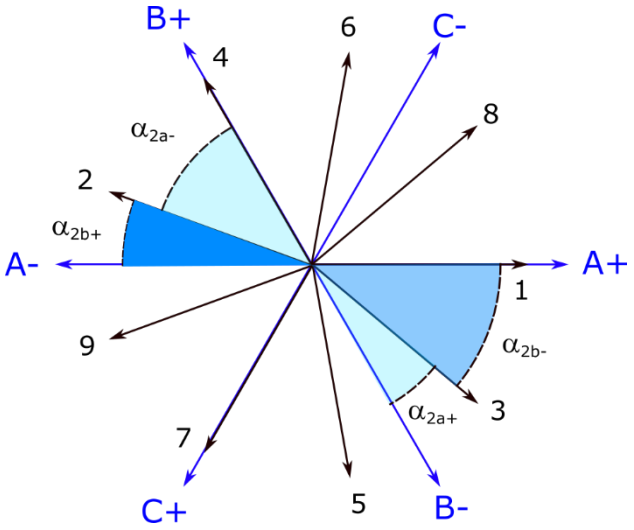

Fig. 22 Star of slot evolution 9 8 configuration

This type of approach is strongly dependent on the initial angle, i.e. the position of spoke corresponding to the first tooth. As it is possible to see in Fig. 23, shifting the initial angle, it is possible to obtain different winding structures, because the amplitude of angles between blue spokes and black spokes change. Imposing an initial angle equal to 0, it is easy to see that there is only one coil wound around teeth 1, 4, 7 in Fig. 24 while the other have two coils belonging to different phases.

.

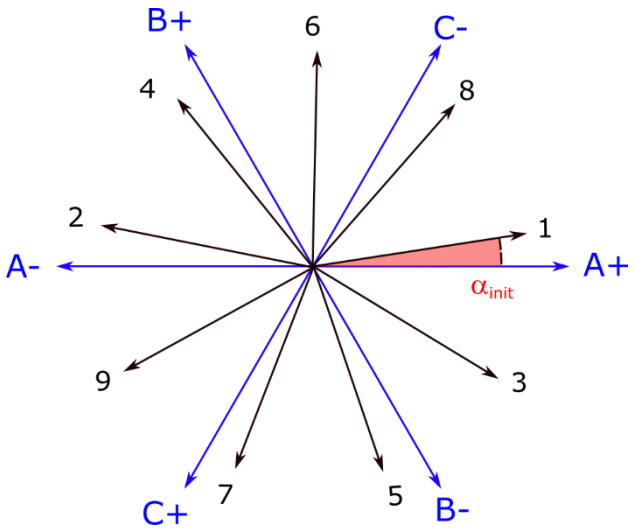

Fig. 23 Initial angle for star of slot evolution 9 8 configuration

In Fig. 23, given an initial angle unequal to zero, all teeth have two coils wounded around them (Fig. 25).

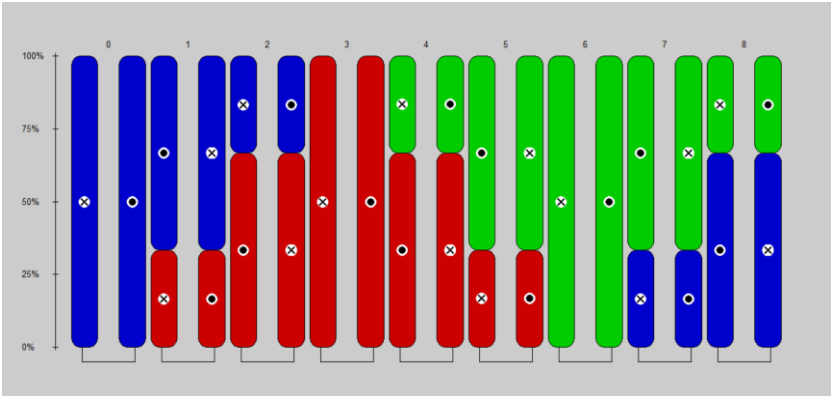

Fig. 24 winding for 9 8 configuration star of slots evolution, initial angle = 0

number of turns 9 8 config α_{init}=0				
		phases		
		a	b	c
tooth	1	100	0	0
	2	-67	33	0
	3	33	-67	0
	4	0	100	0
	5	0	-67	33
	6	0	33	-67
	7	0	0	100
	8	33	0	-67
	9	-67	0	33

Table 4 winding matrix for 9 8 configuration star of slots evolution, initial angle = 0

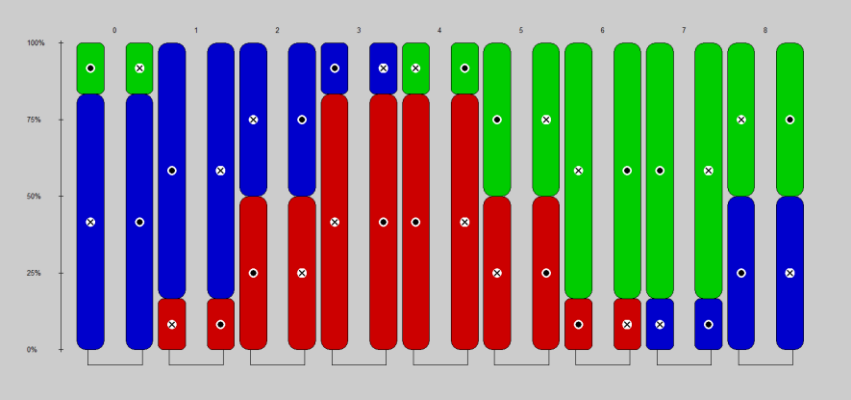

Fig. 25 winding for 9 8 configuration star of slots evolution, initial angle = 10°

number of turns 9 8 config α_{init}=10				
		phases		
		a	b	c
tooth	1	83	0	-17
	2	-83	17	0
	3	50	-50	0
	4	-17	83	0
	5	0	-83	17
	6	0	50	-50
	7	0	-17	83
	8	17	0	-83
	9	-50	0	50

Table 5 winding matrix for 9 8 configuration star of slots evolution, initial angle = 10

This evolution of star of slots leads to design multilayer windings with α_{init} as a variable. Setting this variable, it is possible to change the fundamental of MMF on one side, on the other side the

amount of losses in the magnets. The next step is to know the range of this variable. Minimum angle assumable is obviously 0. Increasing α_{init}, the MMF fundamental and losses in the magnets decrease. The maximum angle depends on the periodicity of the machine and is different for odd or even number of visible slots (3-3). The maximum value of α_{init} is

$$\alpha_{init} = \frac{2\pi}{\frac{Z}{t}*2} \text{ if } N_{VS} \text{ is even}$$

$$\alpha_{init} = \frac{2\pi}{\frac{Z}{t}*4}, \text{ if } N_{VS} \text{ is odd.}$$

In order to verify the electrical symmetry of the wining, an independent numerical method has been used. A finite element model of a generic machine with concentrated winding designed through star of evolution and described in Table 4 has been built and solved. In Table 6 there are the main data. In particular, simulating the machine as a generator in no load condition, the voltage output waveform has been analyzed. A rotor speed equal to 750 rpm has been used, in order to obtain a frequency of 50 Hz.

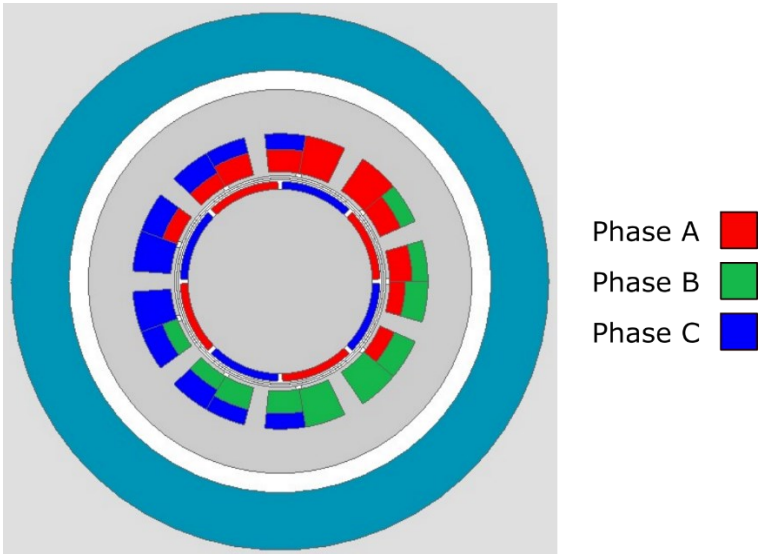

Fig. 26 cross section of a FEM model

Number of stator slots, Z	9	Number of phases	3
Number of pole pairs, p	4	Maximum number of turns per coil, N_0	100
Stator bore radius, R_s	55 mm	Stator frequency, f	50 Hz
Rotor core radius R_r	48 mm	Magnet permeability, μ	$4\pi10^{-7}$ H/m
Permanent magnet height, h_m	4 mm	Magnet electrical conductivity, σ	0.667 MS/m
Air gap width, g	3 mm	Magnet to pole span ratio, c_m	0.95
Core length, L	100 mm	Stator and rotor core permeability	$4\pi10^{-2}$ H/m

Table 6 FEM model main data

Phase voltage in no-load condition (Fig. 27) shows three sinusoidal waveforms with the same amplitude and shifted each other by 120 electrical degrees. This is another independent method to prove the electrical symmetry for the multilayer winding deigned by star of slot evolution.

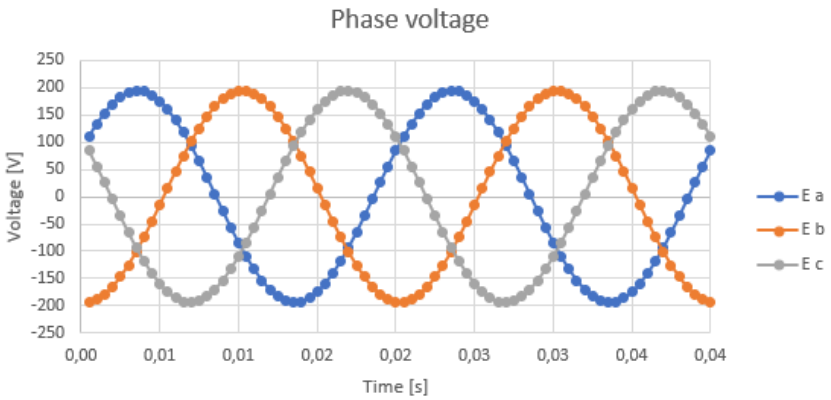

Fig. 27 Back EMF FEM model, no load conditions

3.3. Comparison

This paragraph will present the comparison between the performances of windings built by quadratic optimization and by the evolution of star of slots. The performance of winding designed by evolution of star of slots is added to the pareto front graphs (already discussed in the previous chapter) in order to evaluate potentials and limits of this algorithm.

Fig. 28 shows a comparison of pareto fronts diagram for 9 slots 8 pols configuration; two green point can be seen representing two windings designed through evolution of star of slots method. The green point on the right (A) represents a winding designed setting initial point equal to zero. As earlier observed, this winding produces higher fundamental MMF and losses, than the winding represented by point (B). These two points are compared to pareto front produced through quadratic optimization. On the left side, there is an image of "visible" spokes for Star of slots theory.

For 9 slots 8 poles configurations, there seems to be a good accordance between the two methods. However, there are limits for the evolution of star of slots method, indeed, as shown in Fig. 28: it is not possible to design windings having performance spanning in the complete range of optimal designs obtained through quadratic programming. Instead, only a subset of the points constituting the Pareto front can be obtained.

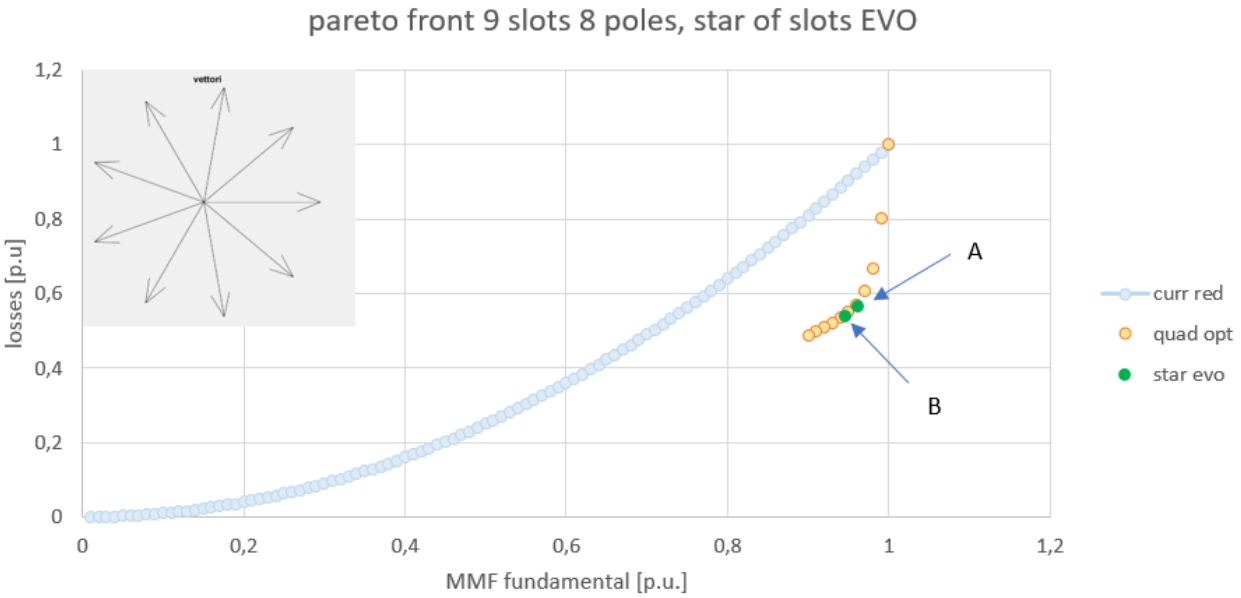

Fig. 28 comparison of quadratic optimization and evolution of star of slots configuration 9 slots 8 poles

An interesting case of study is a unreducible combination, for example 9 slots 6 poles. In 2.5 and 2.6 it has been seen that unreducible combinations have harmonic spectra composed of only MMF harmonics linked to each other and linked to the foundamental. In this case, making use of optimization, a improving of perfromances is not obtainable.

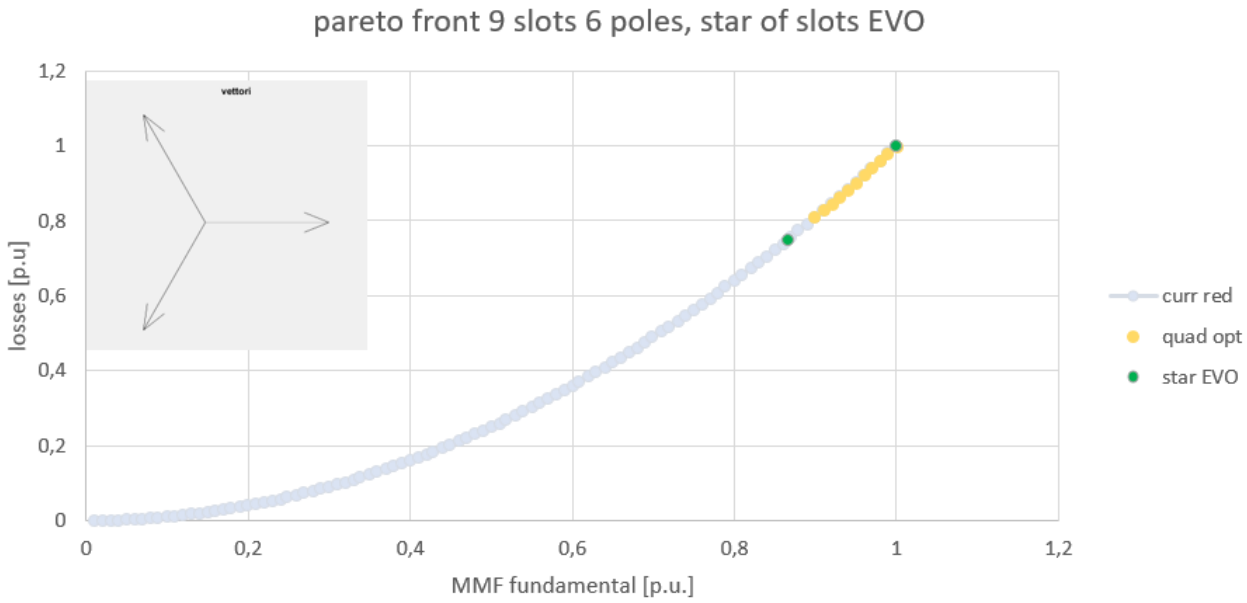

Fig. 29 comparison of quadratic optimization and evolution of star of slots configuration 9 slots 6 poles

Fig. 29 confirms that for unreducible configuration the star of slots fails to improve the winding performance, as expected. Looking at the box in Fig. 29 it can be noticed that the visible spokes are 3 shifted by 120 degrees (as phase angle). In other words, all other spokes are superimposed. It means that, imposing an initial angle equal to 0, all three spokes are aligned with spokes representing phases and double layer winding is obtained. Changing the initial angle, multilayer windings can be obtained, but the performances are not better than star of slots winding with decreased supply current. This behavior is consistent with 2.7, i.e. it confirms that there does not exist any better winding than the topology designed the standard star of slots.

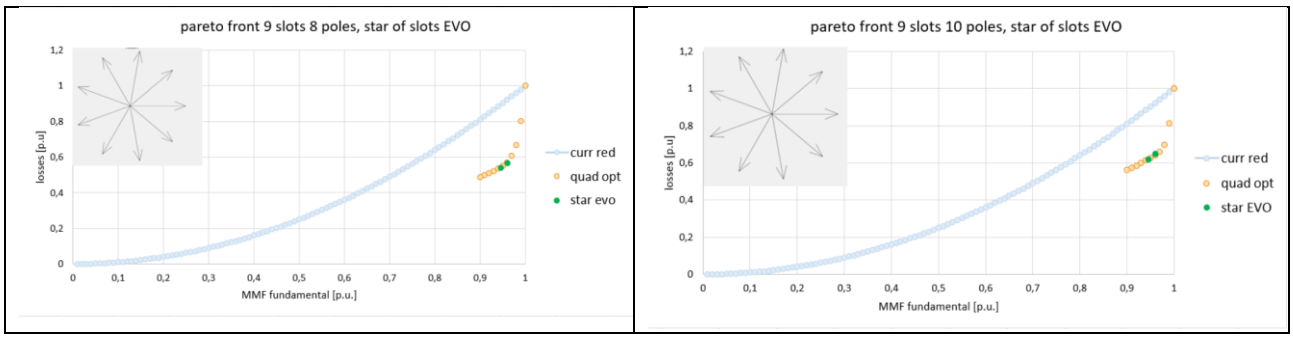

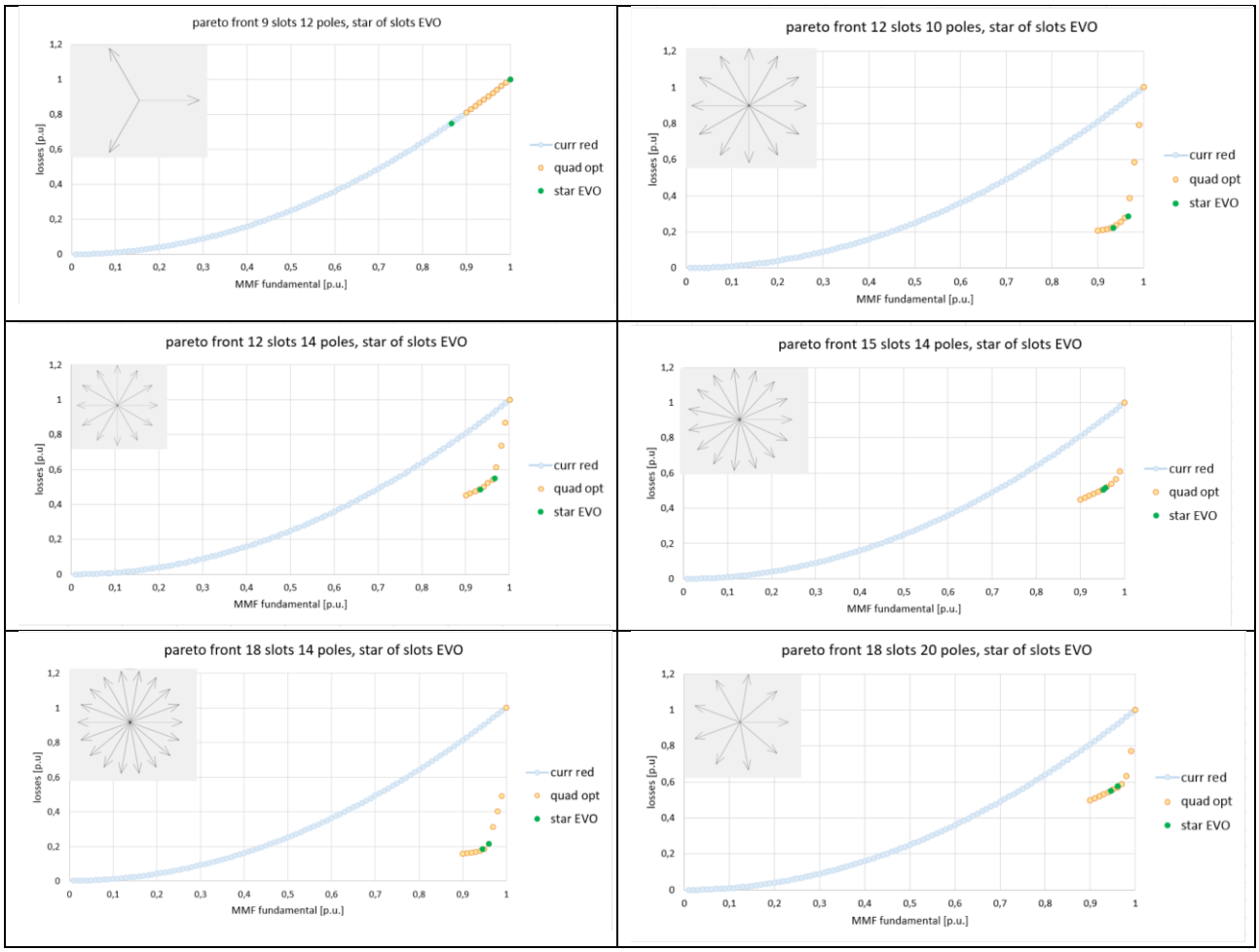

Table 7 comparison of evolution of star of slots for different configurations

In Table 7 Pareto fronts for different configurations are represented and green points refer to windings designed by means evolution of star of slots.

In conclusion, in this chapter an evolution of the known "star of slot method" has been proposed, the geometrical algorithm has been explained, electrical symmetry has been also validated through a FEM simulation in some sample cases and, finally, the performance in terms or losses in the magnet reduction is compared to the results that can be obtained through quadratic optimization as described in 2.6.

4. Design and analysis of multi-layer FSCW with unconventional slot pole combination. – 3 phase machines

Fractional-slot concentrated winding (FSCW) is gaining increasing popularity for electric machine stator construction as it is easy to manufacture, gives short end coils, helps reduce resistive losses, allows for modular architectures and better flux weakening performance [1]. Among the various types of FSCW variants, the dual-layer one (with a single coil wound on each tooth) is the most frequent choice [16]. It is commonly assumed in the existing literature that a symmetrical three-phase FSCW is feasible only on condition that the number of slots Z is an integer multiple of 3 times the maximum common divisor between Z and the number of pole pairs p. Slot-pole combinations satisfying this rule can be defined conventional, the others unconventional. In contrast to the common belief it will be shown that, using a multi-layer arrangement, it is possible to synthetize a symmetrical FSCW having unconventional slot pole combinations. A general design methodology for this purpose is presented and validated by Finite Element Analysis (FEA).

4.1. Feasibility rule

It is commonly assumed in the literature that [6] for a three-phase dual-layer FSCW with Z slots and p pole pairs to be symmetrical, the number of slots Z must be and integer multiple of $3t$, being t the maximum common divisor between the number of slots Z and the number of pole pairs p. In general

$$\frac{Z}{m * t} \in \mathbb{Z} \tag{4-1}$$

where Z is number of slots, m is number of phases, and t is maximum common divisor between the number of slots Z and the number of pole pairs p.

This rule is commonly presented as a general condition for the winding feasibility even if multi-layer design solutions are used [16]. Slot-pole combinations satisfying the rule are hereinafter referred to as conventional, while the others are defined unconventional. The way how the number of slots and poles is chosen strongly affects machine performance in various respects, such as: winding factor, radial forces and vibration behavior, cogging torque, flux-weakening capability and leakage inductances. Therefore, the need to choose the number of slots and poles, Z and $2p$, among conventional slot-pole combinations poses a limitation to the designer as it narrows the scope of the design solutions for machine performance optimization.

The goal of sections is to prove that, contrary to the common belief, a perfectly symmetrical FSCW can be obtained even with unconventional pole-slot combinations, on condition that a multi-layer winding arrangement (with one or two coils per tooth) is used. A design methodology to synthetize FSCWs with unconventional slot-pole combinations, based on the quadratic-programming approach proposed in Chapter 2, is first presented and validated through finite-element analysis (FEA) simulations.

4.2. Quadratic problem

In Chapter 2 a quadratic-programming approach is presented for the design optimization of a FSCW with reduced rotor losses. In this chapter, the approach is briefly recalled and then adapted to the purpose of designing a three-phase FSCW with a generic number of slots Z and pole pairs p.

Based on the mathematical relationships recalled in the Chapter 2, the problem of designing a symmetric FSCW with Z slots and p pole pairs can be formulated in terms of determining a winding vector $\mathbf{x}$ defined in (1-16) that maximizes the air-gap MMF fundamental amplitude [hence its square (2-9)] while satisfying constraints (2-14)(2-16) and (2-18). The objective of maximizing the MMF fundamental is obviously justified by the need to obtain a FSCW layout with the highest possible winding factor. The FSCW design is thus reduced to the solution of the following quadratic programming problem:

$$
\begin{gathered}
maximize\ \boldsymbol{x}^{\boldsymbol{T}}\boldsymbol{Q}_{\boldsymbol{p}}\,\boldsymbol{x} \\
\text{subject to} \\
\boldsymbol{A}_1\boldsymbol{x} \leq \boldsymbol{b}_1 \\
\boldsymbol{A}_2\boldsymbol{x} \leq \boldsymbol{b}_2 \\
\boldsymbol{A}_3\boldsymbol{x} = \boldsymbol{b}_3
\end{gathered}
\qquad (4\text{-}2)
$$

The formulation (4-2) differs from that considered (2-23) because it is a single-objective problem without dependency on φ_p , which can be straightforwardly solved in the Matlab environment. In addition, being the MMF fundamental an objective function, the constraint regarding its value is removed.

Vector element	Meaning
$[\mathbf{x}_{\text{tooth},k}]_0$	Number of phase-*a* turns wound on tooth *k* in CW. sense
$[\mathbf{x}_{\text{tooth},k}]_1$	Number of phase-*c* turns wound on tooth *k* in CCW sense
$[\mathbf{x}_{\text{tooth},k}]_2$	Number of phase-*b* turns wound on tooth *k* in CW sense
$[\mathbf{x}_{\text{tooth},k}]_3$	Number of phase-*a* turns wound on tooth *k* in CCW sense
$[\mathbf{x}_{\text{tooth},k}]_4$	Number of phase-*c* turns wound on tooth *k* in CW sense
$[\mathbf{x}_{\text{tooth},k}]_5$	Number of phase-*b* turns wound on tooth *k* in CCW sense

Table 8 Definition of the k-th tooth vector elements

As a solution of (4-2), the optimal winding vector is obtained, and, from this, it is possible to fully determine the whole winding layout. To this end, it is sufficient to extract the Z tooth winding vectors according to (1-16): in the three-phase case, the six elements of k_{th} winding vector indicate (according to Table 8) how many turns are to be wound on the k_{th} tooth for any phase, and in which sense.

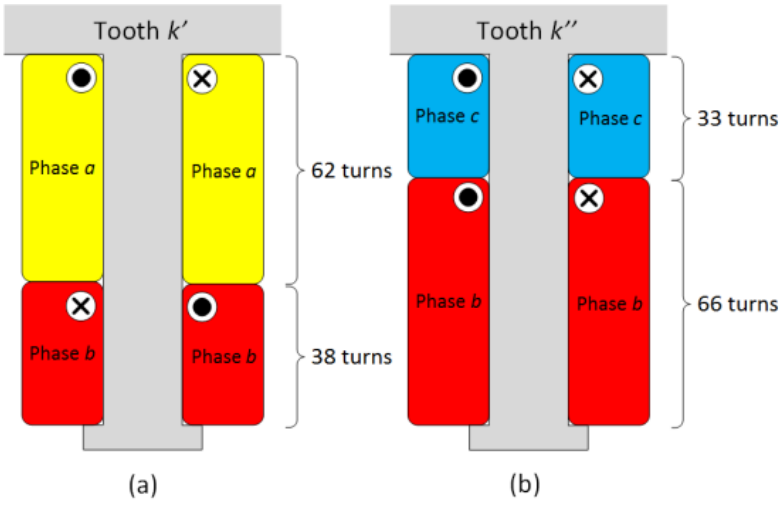

Fig. 30 Examples of tooth windings for (a) the k-th tooth; (b) the k-th

It may be worth noting that all the matrices $\mathbf{Q}_p$, $\mathbf{A}_1$, $\mathbf{b}_1$, $\mathbf{A}_2$, $\mathbf{b}_2$ e $\mathbf{A}_3$, $\mathbf{b}_3$ and appearing in (4-2) do not depend on the machine geometry, as proved by their analytical formulations recalled in Chapter 1. Hence, the FSCW layout obtained from the solution of (4-2) is the same irrespective of machine geometry and dimensions.

It is important to observe that, in both deriving and using the equations reported in the previous chapters, no restrictive hypothesis has been made on Z and p, which can be two arbitrary integers. This suggests that the optimization problem (4-2) may yield a solution even for those slot-pole combinations which are commonly regarded as unsuitable for a symmetric winding design. This fact will be confirmed in the next paragraph focusing on two case studies (8-slot 6-pole and 11-slot 10-pole FSCWs).

4.3. Design and performance assessment of an 8 slot 6 pole of an 11 slot 10 pole FSCW

For illustration purposes, the problem (4-2) is herein solved for two example slot-pole combinations, which are: Z=8, $2p$=6 and Z=11 and $2p$=10. For the 8-slot 6-pole winding the maximum number N_{tooth} of turns which can be wound around a tooth is set to 88, while for the 11-slot 10-pole machine it is assumed equal to 100.

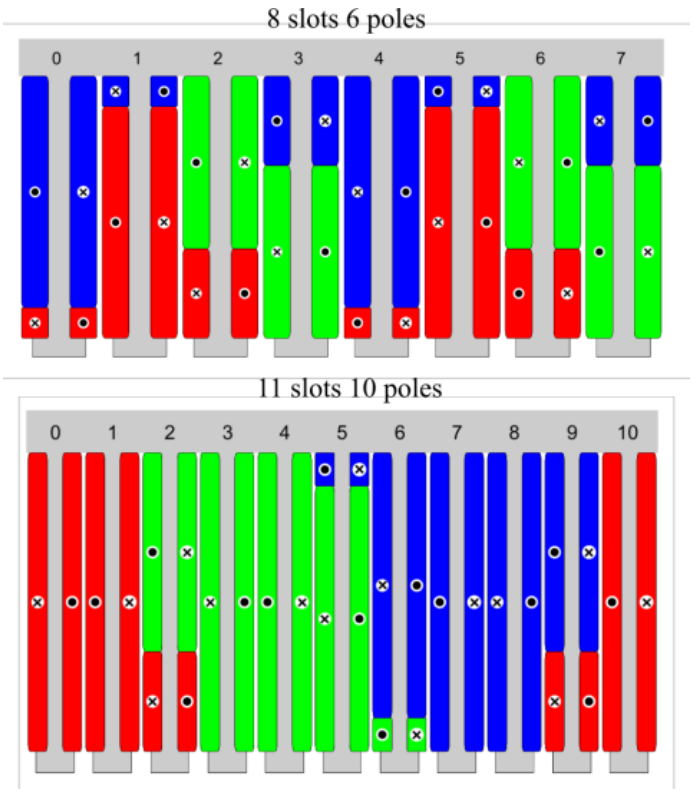

Fig. 31 Winding layouts for a FSCW with 8 slots and 6 poles and with 11 slots and 10 poles

The FSCW layouts, which result from the numerical solution of (4-2) in the two cases, are shown in

Fig. *31* and the numbers of turns per tooth per phase are detailed in Table 9 and Table 10.

	Tooth index							
	k=0	k=1	k=2	k=3	k=4	k=5	k=6	k=7
Phase +a	11	0	30	0	0	77	0	0
Phase –a	0	77	0	0	11	0	30	0
Phase +b	0	0	0	58	0	0	58	0
Phase –b	0	0	58	0	0	0	0	58
Phase +c	0	11	0	0	77	0	0	30
Phase –c	77	0	0	30	0	11	0	0

Table 9 Turns per tooth per phase in the 8-slot 6-pole winding

	Tooth index									
	k=0	k=1	k=2	k=3	k=4	k=5	k=6	k=7	k=8	k=9	k=10
Phase +a	100	0	33	0	0	0	0	0	0	33	0
Phase –a	0	100	0	0	0	0	0	0	0	0	100
Phase +b	0	0	0	100	0	89	0	0	0	0	0
Phase –b	0	0	67	0	100	0	11	0	0	0	0
Phase +c	0	0	0	0	0	0	89	0	100	0	0
Phase –c	0	0	0	0	0	11	0	100	0	67	0

Table 10 Turns per tooth per phase in the 11-slot 10-pole winding

For the sake of simplicity, in Table 9 and Table 10 as well as in the rest of the thesis, each phase is designed with sign "+" if wound in CW sense and sign "–" otherwise. In order to assess the performance of the two synthetized windings, they are applied to a sample SPM machine and compared to a couple of similar conventional winding configuration, having the same pole count: the 8-slot 6-pole winding is compared to the usual 9-pole 6-phase one and the 11-slot 10-pole winding is compared to the usual 12-slot 10-pole one.

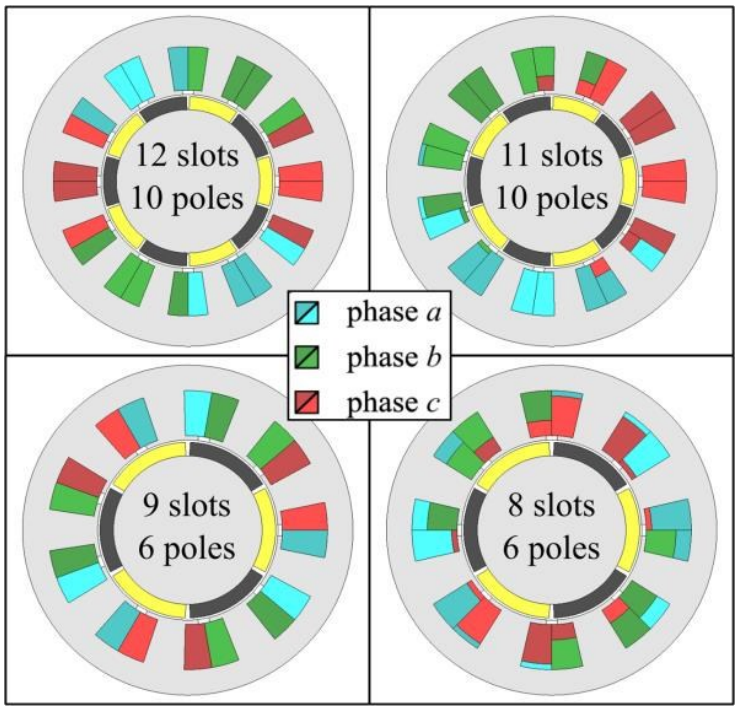

Fig. 32 Cross sections of the four SPM machines considered for performance comparison.

The cross sections of the SPM machines under comparison are shown in Fig. 32 and their characteristic design data are provided in Table 11.

	9 slots 6 poles	8 slots 6 poles	12 slots 10 poles	11 slots 10 poles
Nr. of turns per tooth, N_{tooth}	100	100	100	100
Phase peak current, I_0	15.4 A	17.8 A	29.7 A	32.2 A
Magnet to pole span ratio	0.95	0.95	0.95	0.95
Magnet relative permeability	1.04	1.04	1.04	1.04
Magnet electrical conductivity	0.6 MS/m	0.67 MS/m	0.67 MS/m	0.67 MS/m
Magnet coercive force	800 kA/m	800 kA/m	800 kA/m	800 kA/m
Core relative permeability	10^5	10^5	10^5	10^5
Stator bore radius	60 mm	60 mm	100 mm	100 mm
Rotor core radius	49.5 mm	49.5 mm	82.5 mm	82.5 mm
Magnet height	9 mm	9 mm	15 mm	15 mm
Air gap width	1.5 mm	1.5 mm	2.5 mm	2.5 mm
Core length	100 mm	100 mm	100 mm	100 mm

Table 11 Design data of the SPM machines under comparison

For the comparison to be fair, the same slot fill factor, conductor current density and magnetic loading are applied to the all the four machines.

To compare their performance, the four machines are modelled in the JMAG environment and a FEA time stepping simulations are run with a sinusoidal 50 Hz voltage supply in the maximum-torque operating condition, in which the rated current (Table 11) is applied along the rotor q (inter-polar) axis.

Simulation results for the 6 pole machines are given in Fig. 33 (a) and those for the 10 pole machines in Fig. 33(b). The considered diagrams show phase back Electro-Motive Forces (EMFs), supply voltages and currents, electromagnetic torque and radial force components (Fx and Fy) along two orthogonal (x and y) axes. The magnet losses resulting from simulations as well as from the analytical computation method described in 1.4 are reported in Table 12.

	9 slots 6 poles	8 slots 6 poles	12 slots 10 poles	11 slots 10 poles
Magnet losses from FEA	0.16 W/mm^3	0.25 W/mm^3	0.57 W/mm^3	0.67 W/mm^3
Analytically computed magnet losses [16]	0.16 W/mm^3	0.26 W/mm^3	0.58 W/mm^3	0.69 W/mm^3

Table 12 Permanent magnet loss density from fea and analysis

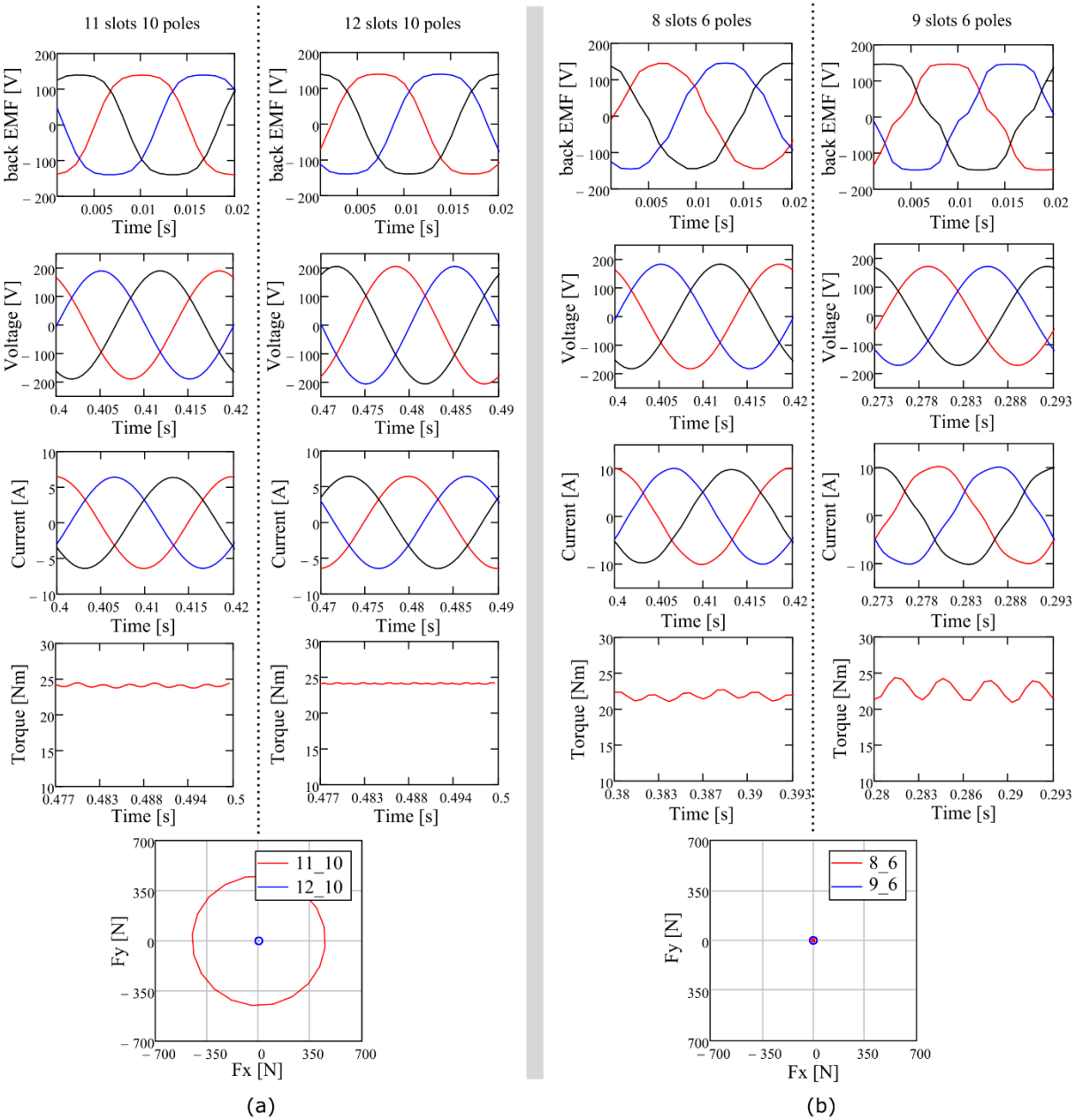

Fig. 33 Time-stepping FEA simulation results for (a) the 9-slot 6-pole (conventional) and the 8-slot 6-pole (unconventional) and (b) 12-slot 10-pole (conventional) and the 11-slot 10-pole (unconventional) machines working in their rated conditions.

Simulation results confirm that the synthetized unconventional FSCWs are perfectly symmetrical (as it can be seen from the back-EMF waveforms) and do not exhibit any kind of current imbalance when supplied from a sinusoidal three-phase source.

More particularly, the performance comparison for the 6-pole machines (Fig. 33 (b)) clearly shows that the unconventional FSCW produces a better EMF, which results in a less distorted stator current and a smaller torque ripple. Conversely, the mean torque is slightly higher for the conventional

motor, since the 9-slot 6-pole FSCW has a higher winding factor (0.866) than that (0.844) of the 8-slot 6-pole FSCW, as it will be discussed in Chapter 5. Regarding the radial forces, both winding configurations give a practically negligible Unbalanced Magnetic Pull (UMP). Finally, with respect to the magnet eddy-current losses (Table 12), these are lower in the conventional machine, indicating a worse air gap MMF space harmonic spectrum from this standpoint.

Moving to the comparison between the 10-pole machines (Fig. 33 (b)), we can observe very similar performance in terms of EMF, current and torque harmonics. The unconventional configuration, however, suffers from higher permanent magnet losses and a noticeably larger UMP compared to the conventional 12-slot 10-pole layout.

It is apparent from the mentioned case studies that unconventional designs cannot be said to give better or worse performance, in general. This justifies the interest of extending the comparison to a wider variety of slot-pole combinations, as done in the next Chapter.

It is a common belief that the design of a symmetrical FSCW is possible only if the number of slots and the number of poles satisfy well-defined algebraic conditions. This Chapter has shown that perfectly symmetrical FSCWs with slot-pole combinations not respecting such conditions and hence defined unconventional, can be designed if a multi-layer winding layout is adopted. A general algorithm, based on quadratic programming, is presented to synthetize a symmetrical FSCW with an arbitrary number of slots and poles. The method has been illustrated in detail taking the 11-slot 10-pole and the 8-slot 6-pole combinations as case studies.

.

5. Comparison between conventional and unconventional slot poles combination

The aim of this chapter is to investigate the performance of FSCWs for a wide variety of both conventional and unconventional slot-pole combinations. The number of slots Z is assumed to vary in the range between 3 and 18, while the number of poles 2p between 2 and 24. As seen in 4.1 a generic combinations of Z slots and 2p poles is conventional if

$$\frac{Z}{3\ x\ GCD\ (Z,p)} \in \mathbb{Z}$$

(5-1)

where $\mathbb{Z}$ is the set of integers, and unconventional otherwise.

The number q of slots per phase is, in any case, defined as:

$$q = \frac{Z}{6p}$$

(5-2)

For the purpose of the investigation, FSCWs with conventional slot-pole combinations are designed in their usual dual-layer form with the well-known star-of-slot method [16]. Conversely, FSCWs with unconventional slot pole combinations are synthetized as discussed in paragraph (4-2) and exemplified in paragraph 4.3, by solving the constrained quadratic programming problem (4-2). However, it is noted that also conventional FSCWs can be, equivalently, designed by solving (4-2). In fact, taking the MMF fundamental maximization as the only objective function, (4-2) always yields

the same optimal solution as the star-of-slot method when Z and p satisfy (5-1). This was already observed in paragraph 2.3 and paragraph 2.4 for conventional machines. As a further remark, it is noted that, in any case, 4.2 provides an optimal solution in which the constraint (2-14) is satisfied in its equality form, i.e. such that each tooth is wound with the maximum possible number of turns N_{tooth}. Next, conventional and unconventional FSCW designs will be compared in terms of various performance or goodness indices, starting with the winding factor.

5.1. Winding factor

Once the optimal winding vector **x** is obtained solving (4-2) for either a conventional or unconventional slot-pole combination, the winding factor k_w of the corresponding FSCW can be easily computed based on the well-known relationship [36]

$$M_{fund} = \frac{3}{\pi}\frac{k_w}{p}N_s I_0$$

(5-3)

where: M_{fund} is the stator MMF fundamental amplitude, I_0 is the stator phase peak current and N_s is the number of series connected turns per phase.

By using

$$M_{fund}^2 = x^T Q\, x$$

(5-4)

for M_{fund} and assuming the number of turns is series per phase given by:

$$N_s = \frac{Z\, N_{tooth}}{3}$$

(5-5)

we obtain the following winding factor expression from (5-3)

$$k_w = \frac{\pi p}{Z\, I_0 N_{tooth}} M_{fund} = \frac{\pi p}{Z\, I_0 N_{tooth}} \sqrt{x^T Q\, x}$$

(5-6)

By means of (5-6) the winding factor is computed for all the slot-pole combinations with 1/3<q<1/2, as these are the only ones which lead to acceptable winding factor values [11]. Results are reported in Table 13

Number of slots \ Number of poles	2	4	6	8	10	12	14	16	18	20	22	24
3	0.866	0.866										
4	0.549		0.549									
5	0.546	0.883	0.883									
6		0.866		0.866								
7		0.736	0.918	0.918	0.736							
8		0.549	0.844		0.844							
9			0.866	0.945	0.945	0.866						
10			0.751	0.883		0.883	0.751					
11			0.718	0.864	0.940	0.940	0.864					
12				0.866	0.933		0.933	0.866				
13				0.783	0.889	0.944	0.944	0.889	0.783			
14				0.736	0.848	0.918		0.918	0.848			
15					0.866	0.883	0.951	0.951	0.883	0.866		
16					0.785	0.844	0.926		0.926	0.844	0.785	
17					0.760	0.853	0.916	0.949	0.949	0.916	0.853	
18						0.866	0.902	0.945		0.945	0.902	0.866

Table 13 Winding factor for various slot pole combinations.

For conventional slot-pole combinations, the winding factors shown in Table 13 and computed through (5-6) are exactly the same as those known from existing literature [11]. It can be seen from Table 13 that the winding factor values are substantially consistent for conventional and unconventional slot-pole combinations. In both cases, k_w exhibits the same distribution, with similar top values all reached for winding configurations having $Z \cong 2p$.

5.2. Rotor eddy-current losses due to MMF harmonics

A further performance index for a FSCW is its content in MMF harmonics causing large eddy-current losses in the rotor conductive parts. To investigate how this feature varies with the chosen conventional or unconventional slot pole combination, a homogenous comparison needs to be made between reasonably designed machines. For this purpose, the SPM machine model shown in Fig. 34 is considered for any number of slots Z and pole pair p.

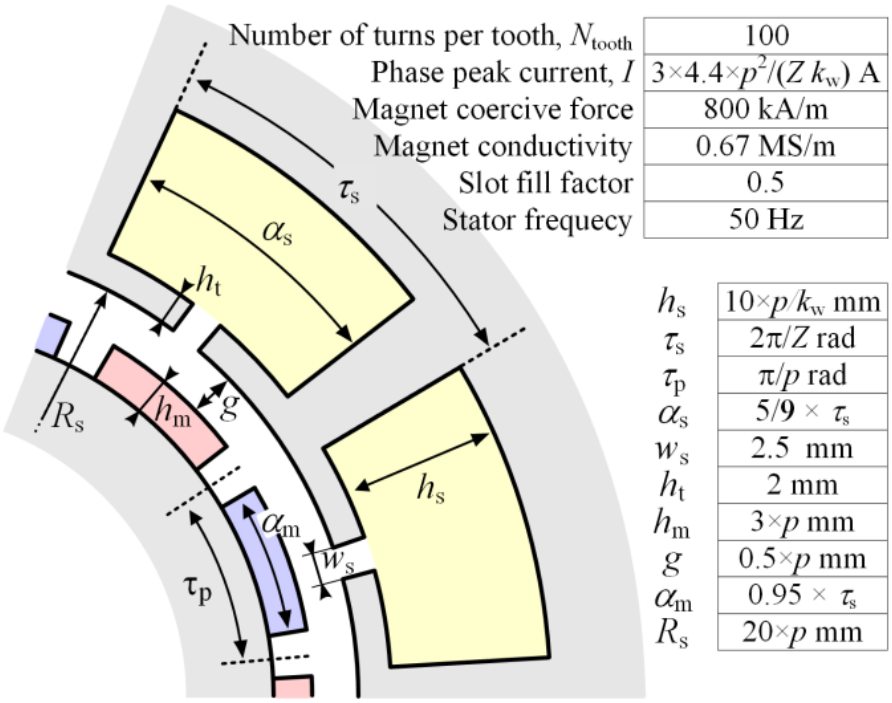

Number of turns per tooth, N_{tooth}	100
Phase peak current, I	$3\times4.4\times p^2/(Z\,k_w)$ A
Magnet coercive force	800 kA/m
Magnet conductivity	0.67 MS/m
Slot fill factor	0.5
Stator frequecy	50 Hz

h_s	$10\times p/k_w$ mm
τ_s	$2\pi/Z$ rad
τ_p	π/p rad
α_s	$5/9\times\tau_s$
w_s	2.5 mm
h_t	2 mm
h_m	$3\times p$ mm
g	$0.5\times p$ mm
α_m	$0.95\times\tau_s$
R_s	$20\times p$ mm

Fig. 34 Machine model for magnet eddy-current loss and UMP evaluation

By selecting machine parameters as indicated in Fig. 34, the conductor current density is maintained invariant (equal to 4 A/mm2) as well as the air gap field due to both permanent magnets and armature reaction (as discussed in the Appendix), while machine dimensions keep realistic for any choice of Z=3, 4, ..., 18 and p=1, 2, …, 12. Core length is not significant because magnet specific losses

(per unit of volume) are considered. Results are reported in Table 14 in terms of mW per magnet cube millimeter. The dependency of permanent-magnet eddy-current loss density on machine dimensions is investigated in [37] through a general approach which is fully applicable to both conventional and unconventional slot-pole combinations.

The losses in Table 14 are computed through the analytical model described in paragraph 1.4 and results are crosschecked by independent time-stepping FEA simulations showing a maximum error below 5%. As already observed for the winding factor, also magnet loss distribution and amplitudes appear from Table 14 substantially consistent for conventional and unconventional slot-pole combinations. This indicates that the MMF space harmonic content responsible for rotor eddy current losses cannot be, in general, said to be better for either conventional or unconventional FSCW designs.

		Numbers of poles											
		2	4	6	8	10	12	14	16	18	20	22	24
Number of slots	3	0.18	7.81										
	4	0.07		20.63									
	5	0.04	0.36	3.42									
	6		0.17		7.73								
	7		0.11	0.55	2.47	13.81							
	8		0.06	0.26		4.58							
	9			0.16	0.79	2.17	7.60						
	10			0.11	0.33		3.30	11.48					
	11			0.13	0.24	0.69	1.79	5.46					
	12				0.15	0.58		2.88	7.51				
	13				0.12	0.34	0.72	1.64	4.04	10.61			
	14				0.09	0.19	0.49		2.35	5.71			
	15					0.14	0.29	0.79	1.56	3.12	7.41		
	16					0.11	0.22	0.53		2.02	4.28	9.64	
	17					0.13	0.18	0.45	0.74	1.39	2.82	6.04	
	18						0.13	0.38	0.72		2.01	3.67	7.19

Table 14 Magnet specific losses for various slot pole

5.3. Cogging torque

The cogging torque in SPM machines is known to be independent of the winding layout. However, it strongly depends on the slot-pole combination, as well as on other design features like the slot

opening width, the magnet to pole span ratio and the stator or rotor skewing [12]. With special regard to the slot-pole combination [13], formally proves how the cogging torque is proportional to the following parameter:

$$c_T = \frac{Z\ x\ 2p}{LCM\ (Z, 2p)}$$

(5-7)

where LCM(x, y) is the least common multiple of x and y. Slot-pole combinations characterized by a large C_T are unfavorable in terms of cogging torque, while those having C_T=1 (the lowest possible value for C_T) are preferred. Table 15 reports the values of C_T for various slot-pole combinations. The table shows that many unconventional combinations have C_T=1 and are therefore good possible candidates for the design of low-cogging-torque machines. In particular, all combinations where Z is an odd number not multiple of 3 (e.g. Z=5, 7, 11, 13, etc.) enjoy the property of having C_T

Number of slots \ Numbers of poles	2	4	6	8	10	12	14	16	18	20	22	24
3	1	1	3									
4	2		2									
5	1	1	1									
6		2		2								
7		1	1	1	1							
8		4	2		2							
9			3	1	1	3						
10			2	2		2	2					
11			1	1	1	1	1					
12				4	2		2	4				
13				1	1	1	1	1	1			
14				2	2	2		2	2			
15					5	3	1	1	3	5		
16					2	4	2		2	4	2	
17					1	1	1	1	1	1	1	
18						6	2	2		2	2	6

Table 15 Parameter C_T for various slot-pole combinations. shaded cells represent unconventional combinations

5.4. Radial force

Radial forces arise in FSCW machines, even in absence of rotor eccentricity, each time the air gap magnetic field has a diametrically-asymmetrical distribution [38]. Conversely, the UMP is zero if

the machine includes a sequence of repeatable groups of coils and poles [7], such that the radial forces generated by all groups have zero sum for symmetry reasons. For example, it is well-known that 9-slot 8-pole combination suffers from high UMP [38]. The same has been observed for the 11-slot 10-pole machine considered in paragraph 4.3: in fact, its winding lacks rotational symmetry as it can be seen from Fig. 32. On the other side, negligible UPM has been found in paragraph 4.3 for the 12-slot 10-pole, 8-slot 6-pole and 9-slot 6-pole combinations, which all enjoy a rotationally-symmetric winding layout (Fig. 32). For a comprehensive comparison, the UMP is calculated considering various (conventional and unconventional) slot pole combinations. For each of them, the machine model shown in Fig. 34 is built and studied by time-stepping FEA simulating its steady-state operation at rated current in the maximum-torque working point (i.e. with the armature reaction fundamental aligned to the q axis). The specific UMP is then obtained in terms of maximum radial force acting on a cm^2 of stator inner surface. Such a specific UMP constitutes a good index for homogeneously comparing different slot-pole combinations as explained in the Appendix. The specific UMP values obtained from the simulations are shown in Table 16.

Number of slots \ Numbers of poles	2	4	6	8	10	12	14	16	18	20	22	24
3	1.67	4.52										
4	0.01		0.04									
5	0.07	2.64	2.87									
6		0.00		0.00								
7		0.68	3.28	2.08	1.13							
8		0.00	0.00		0.00							
9			0.00	3.96	1.65	0.00						
10			0.00	0.00		0.00	0.00					
11			0.87	0.83	4.62	1.34	0.35					
12				0.00	0.00		0.00	0.00				
13				0.38	0.22	5.28	1.10	1.06	0.44			
14				0.00	0.00	0.00		0.00	0.00			
15					0.00	0.00	5.95	0.98	0.00	0.00		
16					0.00	0.00	0.00		0.00	0.00	0.00	
17					0.31	0.48	0.13	6.59	0.82	0.06	0.24	
18						0.00	0.00	0.00		0.00	0.00	0.00

Table 16 Specific ump (N/cm2) for various slot-pole combinations. shaded cells are for unconventional combinations

The results shown in Table 16 are in accordance with the known fact FSCW machines having a rotationally symmetric configuration have practically zero UMP in absence of rotor eccentricity [38

]. This is noted to occur for all the slotpole combinations in which Z and 2p are not relatively prime numbers. Overall, UMP values for conventional and unconventional slot-pole combinations are consistent in their distribution and amplitude

In this chapter. by means of time-stepping FEA, the performance of FSCWs with conventional and unconventional slot-pole combinations have been comparatively assessed in terms of winding factor, rotor eddy-current losses, cogging torque and radial forces without eccentricity. The comparison has shown a substantial consistency between conventional and unconventional slot-pole combinations under all respects, in the sense that unconventional combinations cannot be stated, in general, to behave better or worse than conventional ones. In the next chapter will be introduced an interesting case of study, where a unconventional slot-pole combinations will be used.

6. Application example and experimental results

This chapter presents a real case study is which a FSCW with unconventional slot-pole combination is applied to the prototype of a motor-generator for shipboard use, illustrated in Fig. 35.

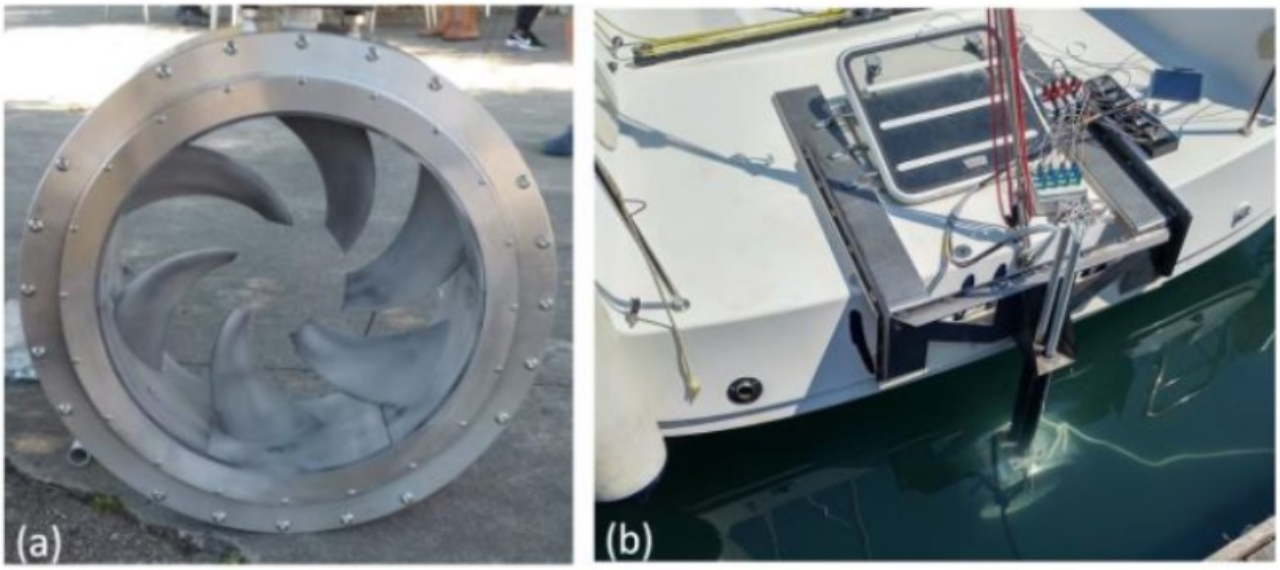

Fig. 35 Prototype motor-generator with a mechanically integrated propeller:(a) before installation; (b) after installation on a boat.

The machine is conceived to operate as an outboard propulsion motor or, when the boat navigates under sail, as a generator to recharge on-board batteries.

6.1. Dimensional and functional requirements

Due to fluid-dynamic reasons, related to propeller optimization, the inner rotor diameter (D_{in} in Fig. 36) is imposed to be equal to 400 mm and the rotor speed to 1000 r/min. Furthermore, all the radial dimension h of the active parts, including the stator and rotor yoke heights h_{sy} and h_{ry}, need be minimized to reduce drag forces during navigation.

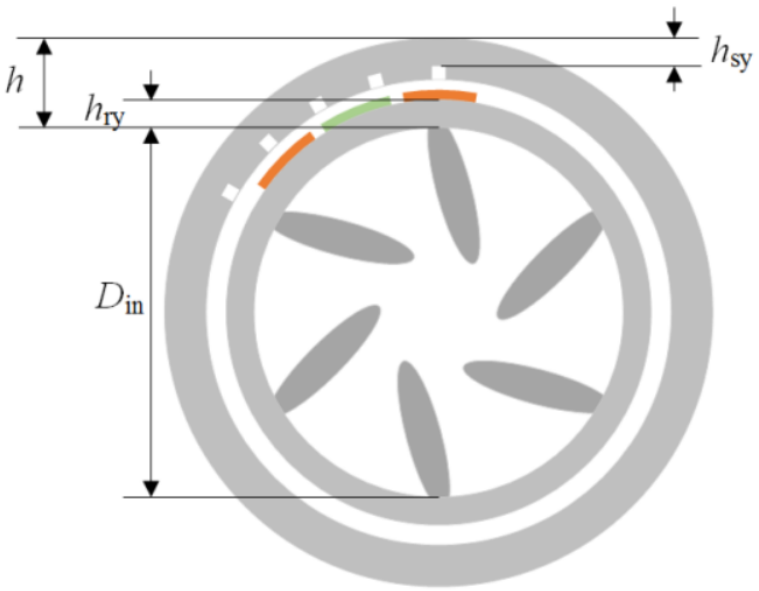

Fig. 36 Schematic machine cross section showing the inner rotor diameter Din as well as stator and rotor yoke heights h_{sy} and h_{ry}

From a system-level point of view, the machine is required to consist of four independent three-phase sections, each connected to an AC/DC converter as shown in Fig. 37.

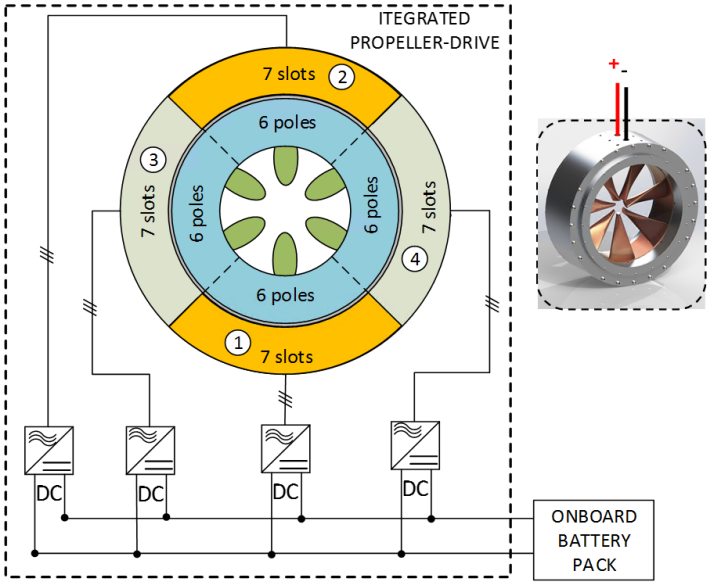

Fig. 37 Functional architecture of the system

The converters are connected to the shipboard DC bus. The segmentation of the system into four modules is aimed at improving fault tolerance (allowing for service continuity at reduced power in case of a faulty module) and is also needed to reduce the size of AC/DC converter power electronics boards, so that they can be mechanically integrated into the machine stator frame (Fig. 38).

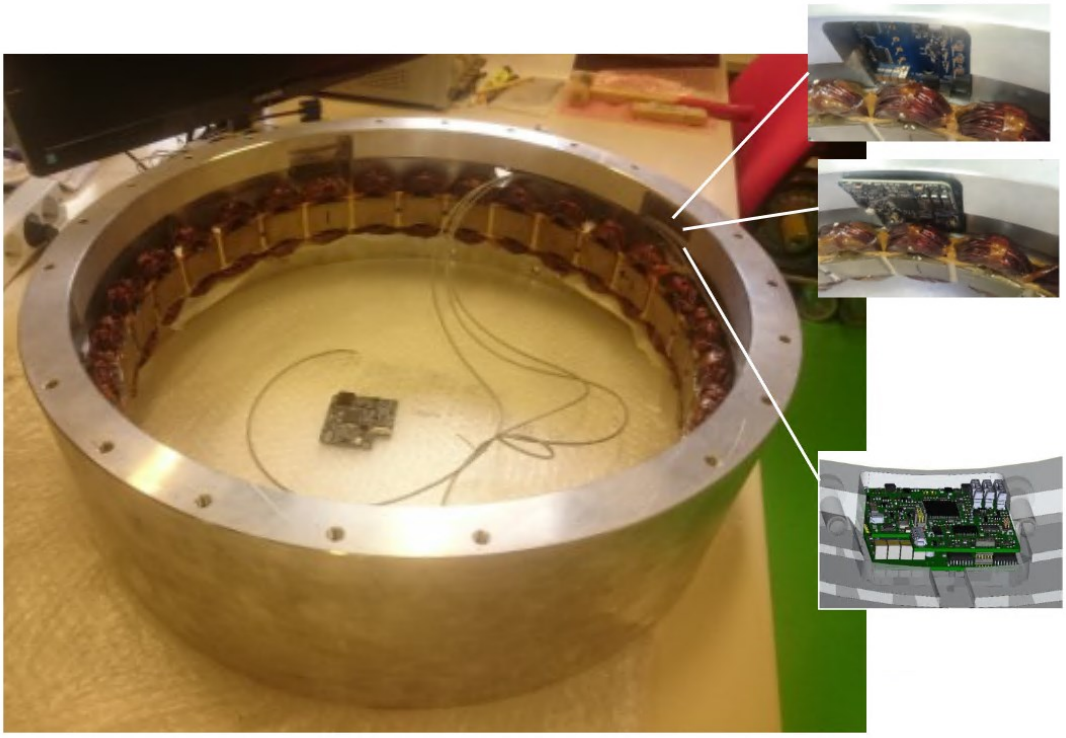

Fig. 38 Machine stator frame and compartments for AC/DC power electronics board installation.

Finally, to limit switching and iron core losses within safe limits, the system frequency is constrained not to exceed 200 Hz.

Fig. 39 machine stator winding and stator frame

6.2. Unconventional FSCW design choice

The 200 Hz frequency limit combined with the 1000 r/min rated speed leads to a maximum number of poles equal to 24. Furthermore, a very limited room is available (Fig. 38) for stator winding end coils as well as for the connecting cables between the windings and the four converters. This leads to select a dual-layer FSCW (due to its short end coils) and to segment it into four three-phase Z-slot 2-p-pole sections, displaced by 90 degrees apart. In this way, by installing the converters with a 90-degree mutual displacement too (Fig. 38), each three-phase winding section can be located near the relevant converter unit, leading to very short and compact connections.

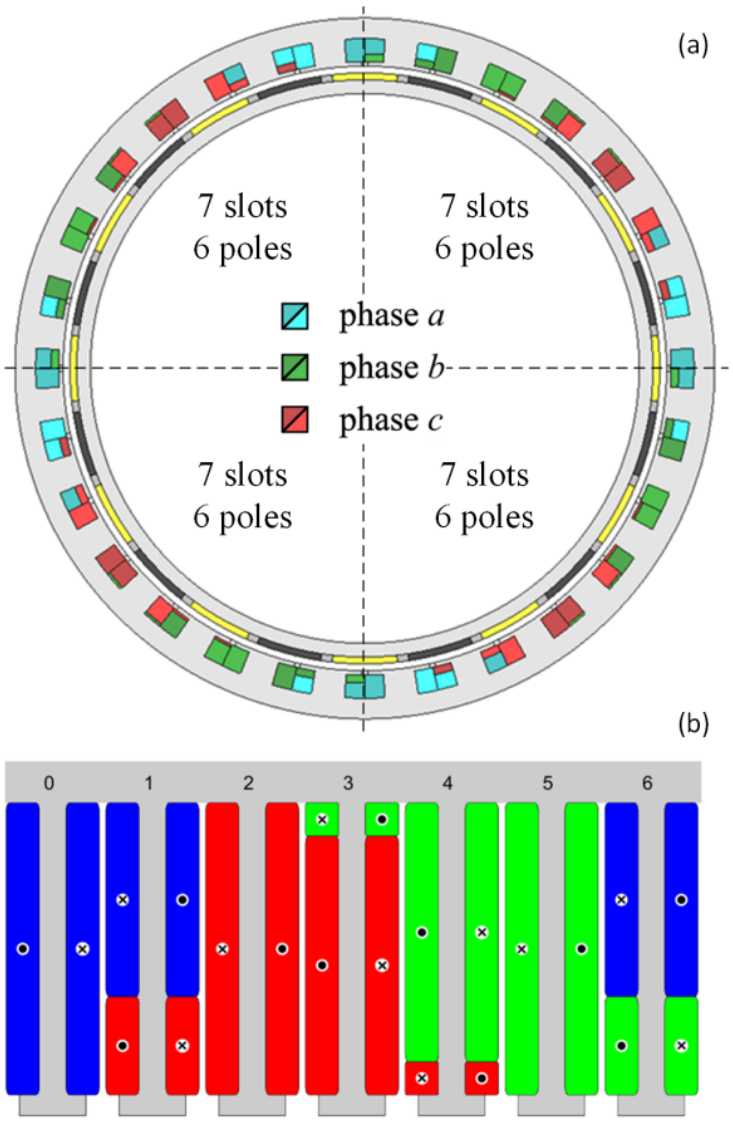

Fig. 40 (a) Motor-generator prototype cross section consisting of four three-phase 7-slot 6-pole sections; (b) FSCW layout for a single section

Since the overall pole count is constrained not to exceed 24, the number of poles 2p of each winding section must be lower than or equal to 6. However, for the fixed inner rotor diameter D_{in}=400 mm, selecting p=1 or p=2 would call for stator and rotor yoke heights h_{sy} and h_{ry} resulting in excessive radial dimensions h (Fig. 36). Hence, the choice of p=3 appears mandatory. Looking at Table 13, it appears that the only conventional 6-pole FSCW featuring an acceptable winding factor has 9 slots. However, the 9-slot 6-pole configuration suffers from a high torque ripple (Fig. 33 (a)) which may cause undesirable vibration and mechanical fatigue over time. At this point, the convenience of using an unconventional slot-pole combination emerges. Good candidates in terms of winding factor (Table 13) would be the 5-slot 6-pole, the 7-slot 6-pole and the 8-slot 6-pole combinations. The first one is discarded due to the relatively high magnet losses (Table 14).

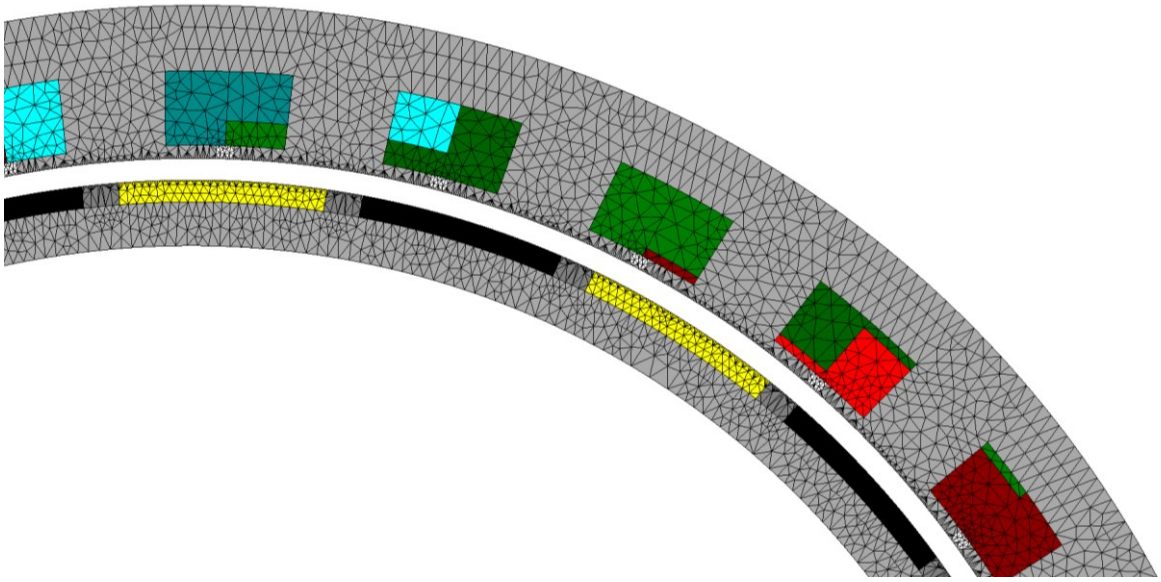

Fig. 41 Discretization of the FEM model

The finally selected choice is the 7-slot 6-pole arrangement (Fig. 40) thanks to its high winding factor (Table 13) and low torque ripple (Table 17).

Slot-pole combination	9 slot 6 poles	8 slot 6 poles	7 slot 6 poles
Peak-to-peak torque ripple in percent of rated torque	14.8%	6.8%	2.7%

Table 17 Steady-state peak-to-peak torque ripple amplitude at rated conditions with sinusoidal stator currents from fea

Regarding the UMP, it is not a concern because the digital management system is designed so that, in faulty conditions, two diametrically opposite machine sections are disconnected while the other two diametrically opposite sections continue to operate, as in [*3*]. This guarantees a rotational symmetry (and hence a negligible UMP [38] [39]) in both healthy and faulty operation, as confirmed by time stepping FEA simulations. As it can be seen from Fig. 40 (b), the 7-slot 6-pole FSCW, designed with the quadratic programming method described in 4.2, is a mixed three- four-layer type including four types of coils, differing by the number of turns. Being N_{tooth}=60 the maximum number of turns which can be wound around a tooth, the four types of coil respectively comprise the following number of turns: 60, 53, 40, 20 and 7. The main design data of the machine are summarized in Table 18.

Phase voltage	4×88 V	Rotor yoke height	10 mm
Phase current	4×9 A	Rotor inner radius	200 mm
Speed	1000 rpm	Core length	30 mm
Power factor	1.0	Magnet to pole span ratio	0.85
Number of slots	4×7	Stator slot opening width	4 mm
Number of poles	4×6	Max. nr. of turns per tooth	60
Stator outer radius	255 mm	Nr. of turns in series per phase	140
Stator bore radius	220 mm	Magnet coercive force	920 kA
Air gap width	5 mm	Magnet relative permeability	1.04
Magnet height	5 mm	Magnet electrical conductivity	0.67 MS/m

Table 18 Prototype ratings and main design data

6.3. Measurements on the prototype

In the design stage, time-stepping FEA simulations are used to assess the prototype design. As well as for the sample machines considered in 4.3, FEA simulations show that the use of an unconventional FSCW does not introduce any kind of unexpected parasitic phenomenon, in both motoring and generating operation modes. In order to achieve an experimental validation of FEA time-stepping simulations, their results are compared with measurements collected on the prototype during its preliminary laboratory testing (Fig. 42).

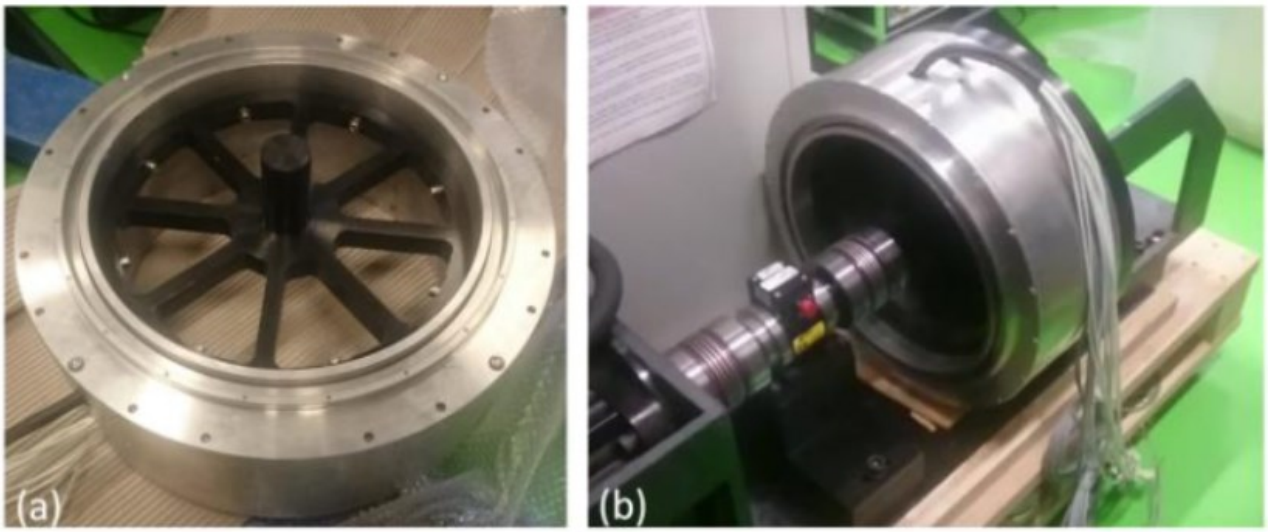

Fig. 42 (a) Machine prototype with blades replaced by a spoked wheel for laboratory testing; (b) coupled prototype on the test bench.

The tests have been performed on the machine driven as a generator, with two diametrically opposite sections at open circuit and the other two connected in parallel on an RL load (Fig. 43a) or to a diode rectifier feeding a resistor (Fig. 43b).

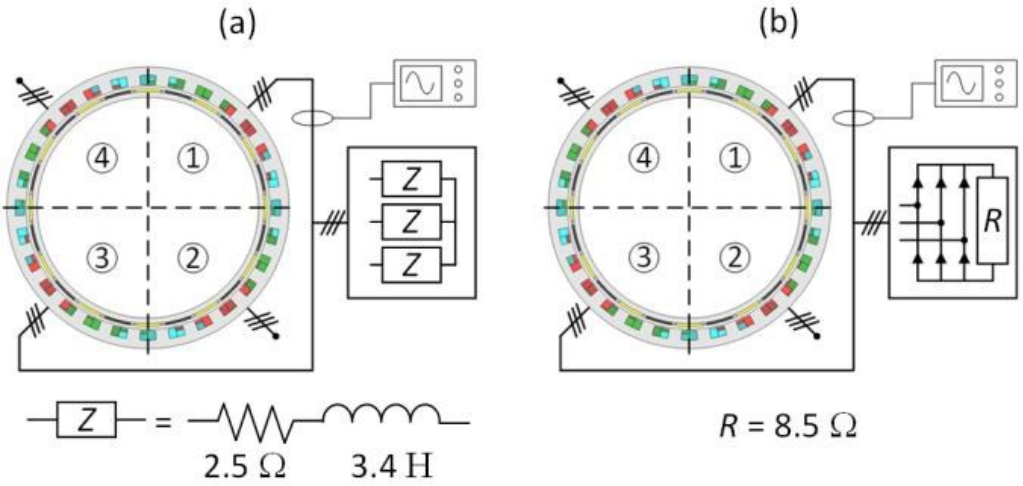

Fig. 43 Prototype test configurations, with sections 2 and 4 at open circuit and sections 3 and 4 connected in parallel to (a) an RL load (b) a diode rectifier feeding a resistor.

In the test conducted according to Fig. 43a, the resistive load is composed of three star-connected RL loads, while in the arrangement depicted in Fig. 43b the load consists of a single resistor. The voltages and currents measured on one phase in the two test arrangements are shown in Fig. 14 and Fig. 15.

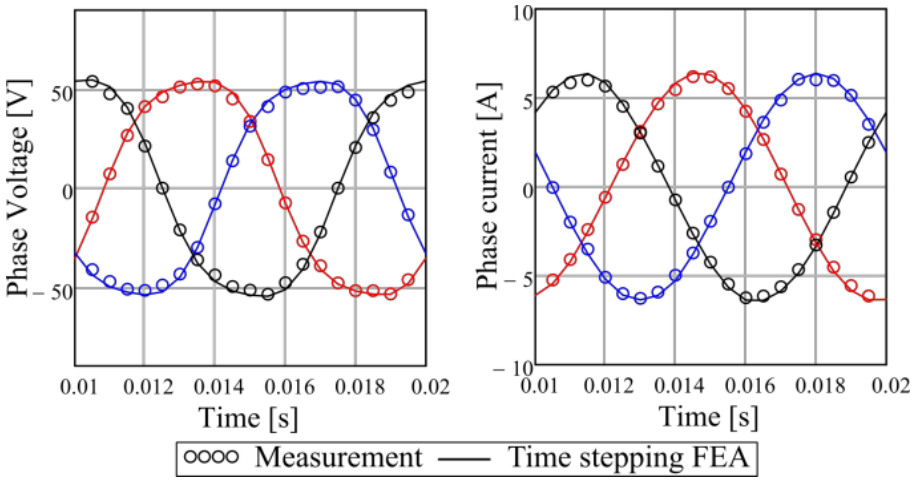

Fig. 44 Phase voltages and currents measured in the test configuration with star-connected RL loads from measurement and time-stepping FEA.

It can be seen that the machine, although loaded on only two of its four sectors, exhibits the same balanced symmetrical behavior that would be expected in case of a conventional FSCW winding. The voltage and current waveforms shown in Fig. 44 and Fig. 45 remain unchanged when sections 2 and 4 of the machine are equally loaded with either the same load as sections 1 and 3 or with a different load.

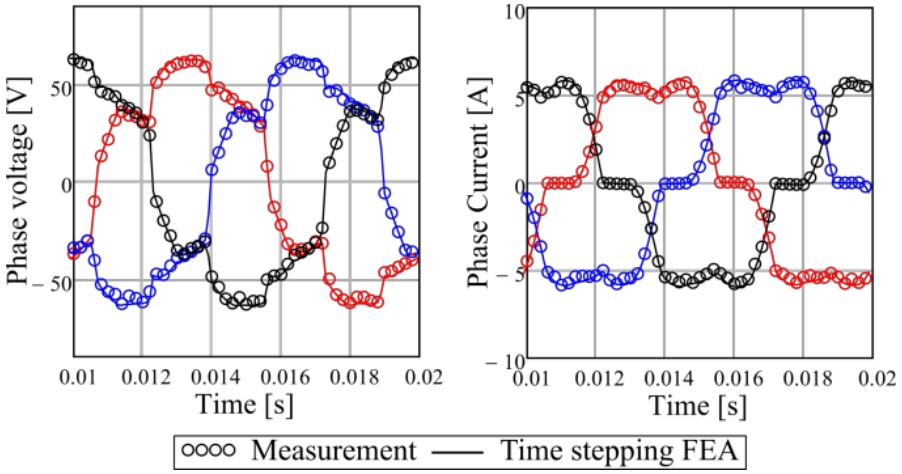

Fig. 45 Phase voltages and currents in the test configuration with a diode rectifier load from measurement and time-stepping FEA

The satisfactory accordance between measurements and simulation results confirms the reliability of time-stepping FEA as a means for analyzing different conventional and unconventional slot-pole combinations in 4.3 and chapter 5.

In this chapter, the possible practical use of an unconventional FSCW has been illustrated by reporting its application to the design of a 28-slot 24-pole permanent magnet machine prototype consisting of four independent 7-slot 6-pole winding sections. The reasons for adopting the unconventional FSCW design have been described. Measurements on the prototype as a driven generator have been reported showing a good accordance with time-stepping FEA simulations and confirming that no unexpected or abnormal effects arise as a consequence of adopting an unconventional FSCW design.

7. Design and analysis of multi-layer FSCW with unconventional slot pole combination. – 6 phases supply

In virtue of its mathematical formulation, the design procedure proposed in the previous chapters for three-phase FSCW's is suitable for an extension to a generic number of phases. Theoretical and experimental results regarding multi-phase and multiple three-phase FSCW's with unconventional slot pole combinations will be explained in this Chapter. It will be shown that the adoption of unconventional slot-pole combinations can be particularly useful in multi-phase machines with concentrated winding of small size, where the number of slots needs to be reduced due to geometrical constraints.

In particular, the adoption of unconventional 9 slot- 8 pole combination, in a 6-phase machine will be illustrated.

As seen in 4.1 a generic combinations of Z slots and $2p$ poles and 6 phases is conventional if

$$\frac{Z}{6 \text{ x } GCD\ (Z,p)} \in \mathbb{Z} \qquad (7\text{-}1)$$

where $\mathbb{Z}$ is the set of integers, and unconventional otherwise, so in this case an unconventional combination will be analyzed.

7.1. Quadratic optimization problem

As seen in 1.1, the optimization approach, based on quadratic programming approach, requires the constraints to be linear equalities o inequalities. To get round the intrinsic non-linear nature of the design variable, it has been convenient to introduce a system of fictitious "sub-currents" (1-3) (Fig. 3). In the 6-phase case, in order to obtain a doble three phase system it is convenient to use another nomenclature of the 12 "sub-currents" i_0, i_1,..., i_{11}, whose phasors are shown in Fig. 46 together with the phasors of the physical currents i_a, i_b and i_c. for the double three system.

It is easily seen that

$$i_{a1} = i_0 = -i_6 \; ; \; i_{b1} = i_4 = -i_{10} \; ; \; i_{c1} = i_8 = -i_2.$$

$$i_{a2} = i_1 = -i_7 \; ; \; i_{b2} = i_5 = -i_{11} \; ; \; i_{c2} = i_9 = -i_3.$$

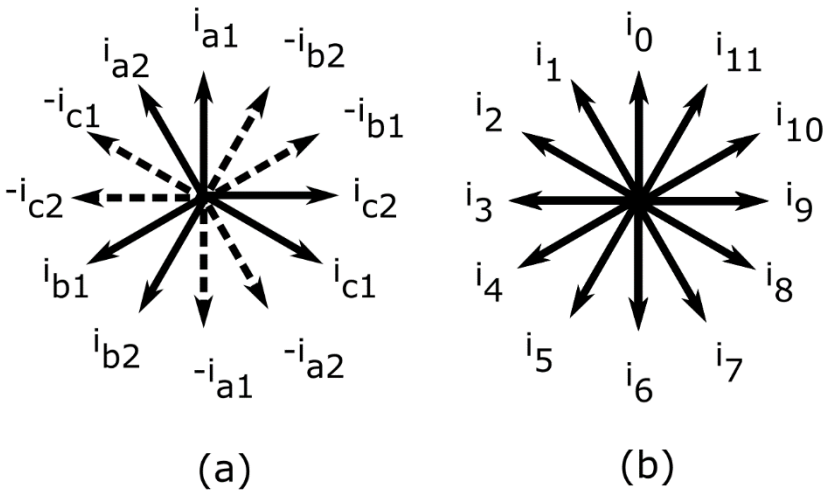

Fig. 46 Six phases case (a) Phase current phasors. (b) Equivalent sub-phase phasors.

In this case, the winding of the generic k_{th} tooth is characterized by a 12-sized positive-defined tooth vector $\mathbf{x}_{\text{tooth,k}}$. The twelve elements of the vector are defined as explained in *Table 19* where the

clockwise (CW) and counter-clockwise (CCW) senses refer to the direction in which a turn is wound around the tooth, if viewed from the air-gap.

Vector element	Meaning
$[\mathbf{x}_{tooth,k}]_0$	Number of phase-*a1* turns wound on tooth *k* in CW. sense
$[\mathbf{x}_{tooth,k}]_1$	Number of phase-*a2* turns wound on tooth *k* in CW sense
$[\mathbf{x}_{tooth,k}]_2$	Number of phase-*c1* turns wound on tooth *k* in CCW sense
$[\mathbf{x}_{tooth,k}]_3$	Number of phase-*c2* turns wound on tooth *k* in CCW sense
$[\mathbf{x}_{tooth,k}]_4$	Number of phase-b1 turns wound on tooth *k* in CW sense
$[\mathbf{x}_{tooth,k}]_5$	Number of phase-*b2* turns wound on tooth *k* in CW sense
$[\mathbf{x}_{tooth,k}]_6$	Number of phase-*a1* turns wound on tooth *k* in CCW. sense
$[\mathbf{x}_{tooth,k}]_7$	Number of phase-a2 turns wound on tooth *k* in CCW sense
$[\mathbf{x}_{tooth,k}]_8$	Number of phase-*c1* turns wound on tooth *k* in CW sense
$[\mathbf{x}_{tooth,k}]_9$	Number of phase-*c2* turns wound on tooth *k* in CW sense
$[\mathbf{x}_{tooth,k}]_{10}$	Number of phase-b1 turns wound on tooth *k* in CCW sense
$[\mathbf{x}_{tooth,k}]_{11}$	Number of phase-*b2* turns wound on tooth *k* in CCW sense

Table 19 Definition of the k-th tooth vector elements

The whole winding can be characterized by the $12Z$-sized winding vector $\mathbf{x}$ obtained by stacking all the tooth vectors:

$$\mathbf{x} = \begin{pmatrix} \mathbf{x}_{tooth,0} \\ \mathbf{x}_{tooth,1} \\ \vdots \\ \mathbf{x}_{tooth,Z-1} \end{pmatrix} \qquad (7\text{-}2)$$

The approach to the problem is the quadratic optimization, already seen in the previous chapters. In particular, the mathematical formalization involves an objective function which maximizes the fundamental MMF, and the constraints permit to be sure that the winding is feasible in terms of maximum number of turns and electrical symmetry.

It is important to observe that, in both deriving and using the equations reported in the previous chapters, no restrictive hypothesis has been made on m, number of phases.

Formulation problem (4-2) has been applied to design a unconventional 6 phases machine, the results of the optimization is the winding defined in the following Table 20, where the winding vector is presented as a winding matrix.

	Tooth index								
	k=0	k=1	k=2	k=3	k=4	k=5	k=6	k=7	k=8
Phase +a1	0	0	40	0	0	0	0	0	0
Phase -a1	0	10	0	10	0	0	0	0	0
Phase +a2	30	0	0	0	0	0	0	0	0
Phase -a2	0	30	0	0	0	0	0	0	0
Phase +c1	10	0	0	0	0	0	0	10	0
Phase -c1	0	0	0	0	0	0	0	0	40
Phase +c2	0	0	0	0	0	0	0	30	0
Phase -c2	0	0	0	0	0	0	30	0	0
Phase +b1	0	0	0	0	0	40	0	0	0
Phase -b1	0	0	0	0	10	0	10	0	0
Phase +b2	0	0	0	30	0	0	0	0	0
Phase -b2	0	0	0	0	30	0	0	0	0

Table 20 Turns per tooth per phase in the 9-slot 8-pole, 6 phase winding

The results of FEM simulation and comparisons to measurement on prototype will be introduced in the following paragraph

7.2. Implementation and testing of a prototype

The main data of the prototype (stator frame and winding are in Fig. 49) are detailed in Table 21.

Number of stator slots, Z	9	Number of phases	6
Number of pole pairs, p	4	Maximum number of turns per coil, N_0	40
Stator bore radius, R_s	55 mm	Stator frequency, f	200 Hz
Rotor core radius R_r	48 mm	Magnet permeability, μ	$4\pi10^{-7}$ H/m
Permanent magnet height, h_m	4 mm	Magnet electrical conductivity, σ	0.667 MS/m
Air gap width, g	3 mm	Magnet to pole span ratio, c_m	0.8
Core length, L	100 mm	Stator and rotor core permeability	$4\pi10^{-2}$ H/m

Table 21 Design data of the 9 slot 8 pole 6 phase SPM prototype

The advantage of using the unconventional configuration is to comply with some specifications relating to the frequency, which dictates the number of poles to be equal to 8, and the fault tolerance that imposes to use the 6 phases configuration. Using a conventional configuration, according to (7-1) the minimum number of slots that it should be used would be 24. If the diameter of the machine is too small Fig. 47, in this case it is in order to 55mm, it is not possible to use 24 slots. Instead with the unconventional configuration it is possible to use 9 slots.

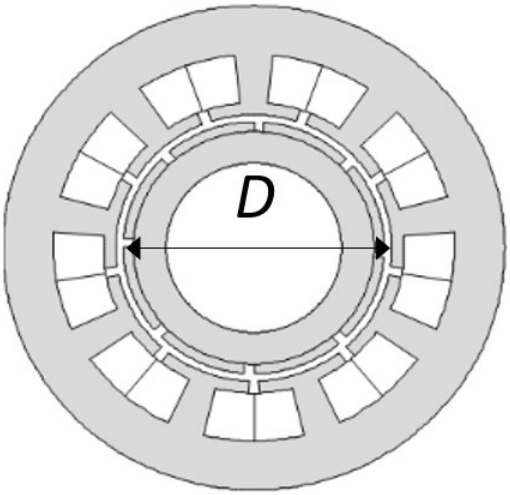

Fig. 47 stator bore dimensions

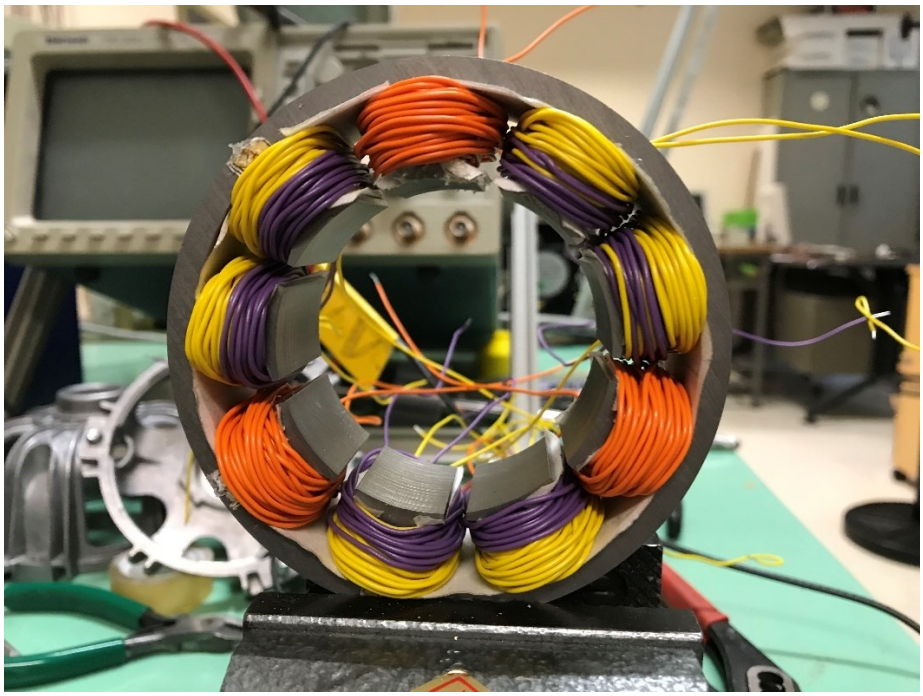

Fig. 48 stator and winding of 9 slot 8 pole 6 phase prototype

In Fig. 48 the prototype stator and the winding are shown. The colors of wires indicate the dimension in terms of turns number of the coil: orange coils have 40 turns, yellow coils have 30 turns, purple coils have 10 turns.

In Fig. 43 the finite element model is given, where colors of coils indicate the phase they belong to.

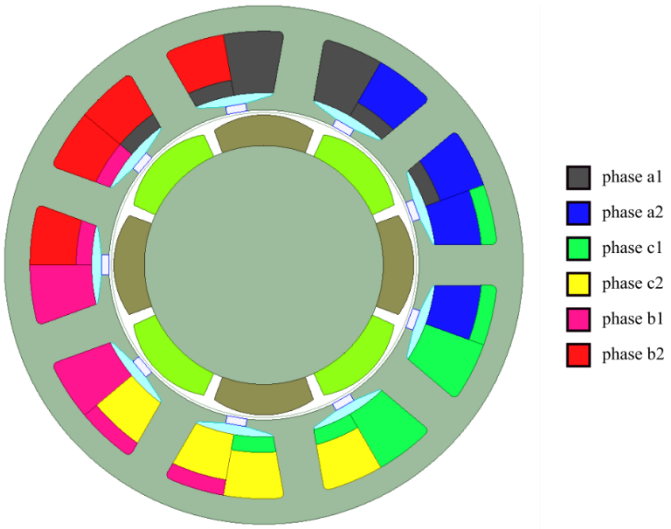

Fig. 49 cross section of 9-slot 8-pole, 6 phase

Fig. 50 shows the test bench: the prototype is used as a generator, driven by the prime mover, an induction motor with 1 pole pair. This prime mover, supplied from 50 Hz mains, rotates at 3000 rpm.

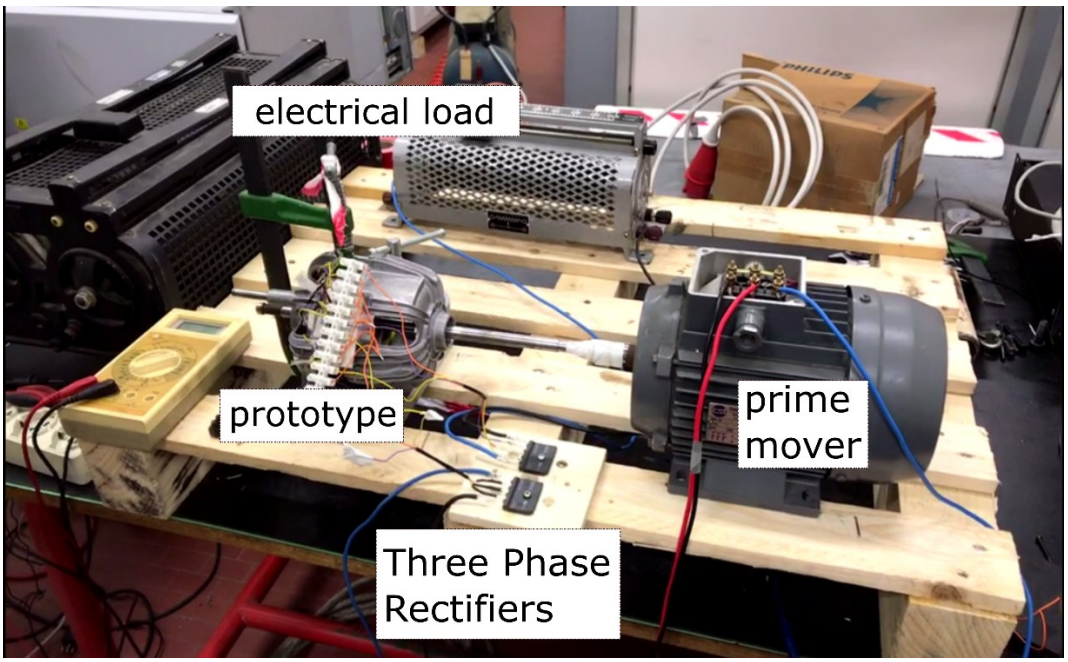

Fig. 50 test bench - 9 slots 4 poles 6 phases prototype

In one case, the prototype is connected to 2 diode rectifiers in series, Fig. 51 (a). The voltage output is a typical 12 pulse rectifier waveform (Fig. 52). Red line is a measured voltage while red one is waveform solution of the simulation. It can be seen that the machine, although being a multilayer unconventional machine, exhibits the same symmetrical behavior that would be expected in case of a conventional FSCW winding.

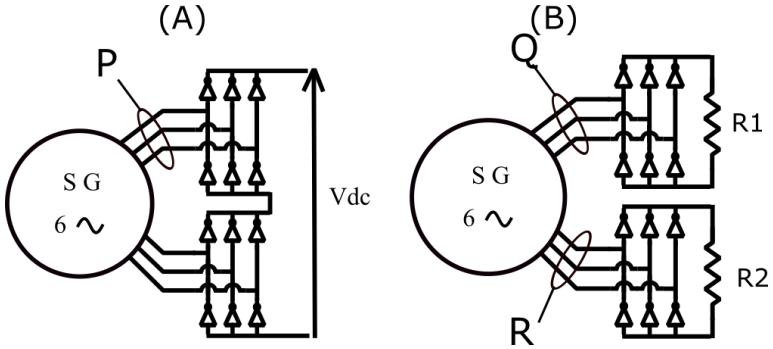

Fig. 51 Prototype test configurations, with (A) 2 diode rectifiers connected in series at open circuit and (B) a separated diode rectifiers feeding resistors R1 and R2

During an electric period (5 ms), the waveform is the typical output of a 12 pulse rectifier (Fig. 52). Instead, measuring three phase voltage (P point of Fig. 51 (A)) we can see three sinusoidal waveforms with the same amplitude a shifted by 120 electric degrees. Fig. 52 shows the comparison between the measurements (E1, E2, E3) and the simulations (a, b, c), exhibiting a satisfactory accordance.

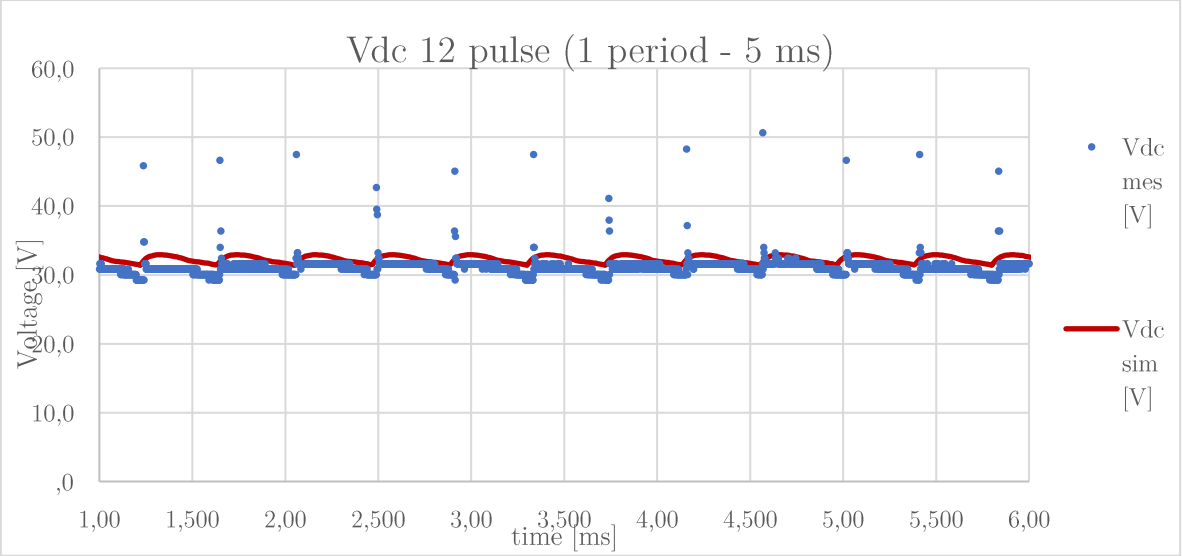

Fig. 52 output voltage rectified from measurement and time-stepping FEA

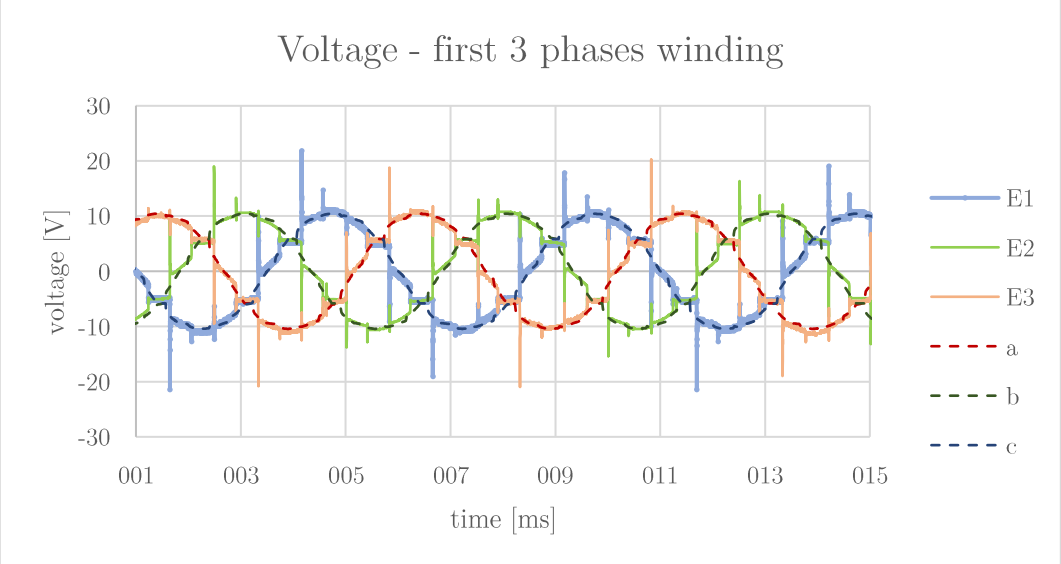

Fig. 53 BackEMF on point (P) (Fig. 51(A))

Some tests have been performed on the loaded machines, loading two windings in two different ways with two different resistors through a rectifier, as per Fig. 51 (B). The results from the measurement and finite element simulations show a good accordance in terms of current flowing in point Q

and R of Fig. 51 (B). Fig. 54 and Fig. 55 show the current waveforms when R1 is equal to 13 Ω and R2 is equal to 33 Ω. Again it is verified that the performance of the machines is exactly the same as it would be expected for a conventional winding.

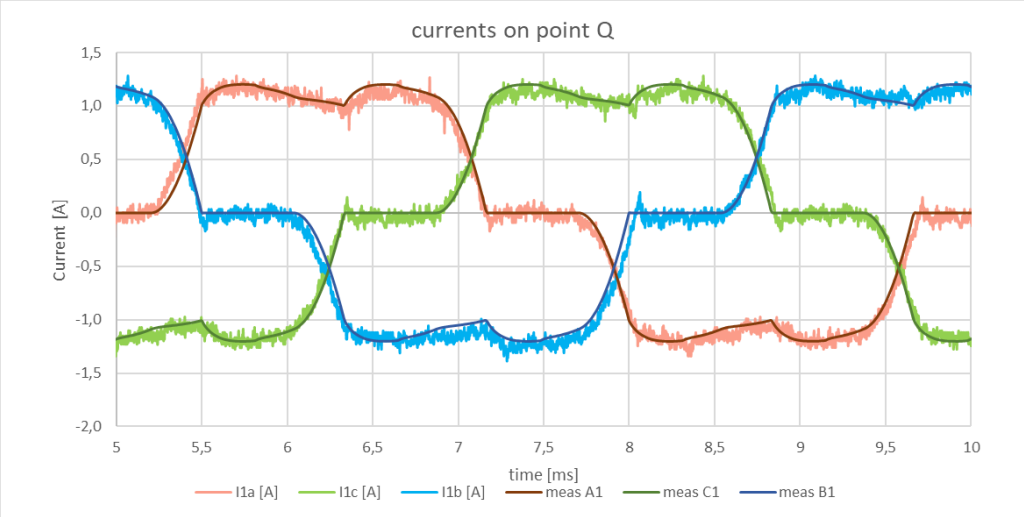

Fig. 54 comparison between the measurements and the simulations: current on point Q Fig. 51 (B)

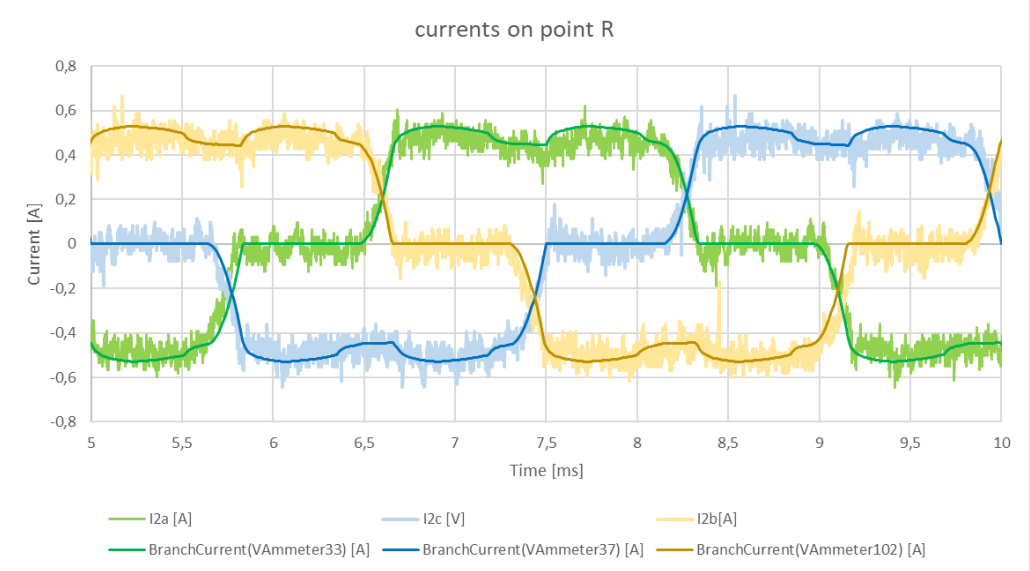

Fig. 55 comparison between the measurements and the simulations: current on point R Fig. 51 (B)

In conclusion, this chapter has presented a prototype with multi-layer concentrated winding structure having an unconventional slot pole configuration. Quadratic optimization is used to design the multi-phase machine, with two three phase windings shifted by 60 electrical degrees apart, 9 slots and 8 poles (while the minimum number of slots that should have been used with conventional winding

is 24). Results of FEM simulations and measurement on prototype are in good accordance and confirm that the machine behaves as a standard dual three-phase one despite the unconventional winding layout when operating as a generator either loaded on pure resistances or on diode bridge rectifiers.

Conclusion

FSCWs in permanent-magnet machines are known to bring important advantages, especially from the manufacturing point of view, but also to have negative impacts on machine performances, due to their richness in air-gap MMF space harmonics. In this thesis new general and systematic methodologies has been proposed to optimize the FSCW of a three and multi-phase SPM machine, through the numerical solution of a quadratic programming problem. At the expense of a reduction in the fundamental MMF amplitude, the proposed optimization can decrease the airgap MMF harmonic content, in order to reduce significantly the losses in the magnets. The intrinsic double-objective optimization problem is explained, the constraints are formulated and the optimal winding performances are represented in the form of pareto fronts. The results in terms of magnet losses for optimized windings are better than for the star of slots winding supplied by decreased current for some well-defined slot-pole combinations, while the optimization is demonstrated to be ineffective (regardless of the method used) for others. In addition, an evolution of the well-known star of slots method has been proposed and the results are compared to the optimal winding performances obtained with quadratic optimization. It has been shown that the modified star of slots method can lead to winding designs which are a subset of those obtainable through the quadratic programming approach. This latter methodology has been also extended to the design of unconventional slot pole configuration, featuring slot-pole combinations which have always been indicated as "unfeasible" by the existing literature for the purpose of obtaining a symmetrically operating machine. A comparison between conventional and unconventional FSCW machines has shown a substantial consistency between their performance under

all respects, in the sense that unconventional combinations cannot be stated, in general, to behave better or worse than conventional ones. The possible practical use of an unconventional FSCW has been illustrated by reporting its application to the design of a 28-slot 24-pole permanent magnet machine prototype, consisting of four independent 7-slot 6-pole winding sections and then to another prototype with 9 slots and 8 poles, equipped with two three-phase windings displaced by 60 electrical degrees. Both of the prototypes have been built and tested, showing a the same behavior that could be expected in conventional winding machines. As an advantage, however, the adoption of an unconventional design has made it possible to comply with design constraints (in terms of restricted number of slots above all) which would have made the machines unfeasible if equipped with conventional FSCWs.

The multilayer structure for concentrated windings allows the designer to obtain a reduction up to 60% of losses in the magnet and to design theoretically all possible combinations, expanding the choices of the designer, as already shown in previous chapters. Obviously wounding more than one coil around the same tooth can slightly complicate the automated manufacturing, although the use of a concentrated winding leads to easier implementation compared to distributed winding.

Appendix A

This appendix provides a justification of the model (described in Fig. 34) which has been used in Paragraph 5.2 to compare different slot-pole combinations in terms of magnet losses and UMP. Using the scaling laws reported in Fig. 34, the slot cross section area changes proportional to

$$\frac{p^2}{Z \text{ x } k_w}$$

(A 1)

Since the number of conductors per slot is maintained constant (2Ntooth=200) as well as the slot fill factor, each conductor cross-section also grows proportional to (A 1). Hence, imposing a phase current equal to

$$3 \text{ x } 4.4 \ \frac{p^2}{(Z \text{ x } k_w)}$$

(A 2)

A results in a constant conductor current density for all slot-pole combinations. Furthermore, both permanent magnet height and air gap width change proportional to p. Therefore, keeping permanent magnet coercive force constant, the flux density amplitude due to permanent magnets is the same regardless of p. Also the fundamental of the flux density due to the armature reaction does not change. In fact, it is given by:

$$B_{s,fund} = \frac{M_{fund}}{g}\mu_0 = \frac{3}{\pi}\frac{k_W}{g\,p}N_s I_0 \mu_0$$

(A 3)

where (5-3) have been used for M_{fund}; considering that (Fig. 34)

$$I_0 = 3\,x\;\; 4.44\,\frac{p^2}{(Z\,k_W)} \quad [A]$$

$$g = 0.5\,p \quad [mm]$$

(A 4)

and being Ns given by (5-5), it is clear from (A 3) that $B_{s,fund}$ is independent of both Z and p. It is therefore demonstrated that the scaling laws given in Fig. 34 guarantee the invariance of the conductor current density, the permanent magnet field and the armature reaction field with respect to Z and p. Of course, the electrical loading A_i, given by:

$$A_i = \frac{6\,N_s\,I_0}{2\,\pi\,R_s}$$

(A 5)

changes proportional to p/k_w as it can be proved by substituting (A 4) and (5-5) into (A 5) and considering that Rs = 20 x p mm Fig. 34 However, choosing an electrical loading which grows with the machine size (hence with the pole count according to the model in Fig. 34) is a common and reasonable practice in the design of electric machines. Regarding the UMP, the radial component of the flux density is usually regarded sufficient for its estimation in FSCW machines. Under this assumption, the total force components along two stationary x and y axes having their origin in the machine center of rotation are given by:

$$F_x(t) = \frac{A_s}{8\,\mu_0}\Re\mathrm{e}\,[\bar{b}(t)]$$

$$F_y(t) = \frac{A_s}{8\,\mu_0}\Im\mathrm{m}\,[\bar{b}(t)]$$

(A 6)

where A_s is the stator bore surface area and $\bar{b}(t)$ is a complex function of time which depends only on the radial flux density harmonics produced by the permanent magnets and by the stator currents. It is therefore clear from (A 6) that, having chosen a dimensioning law (Fig. 34) which preserves the fundamental flux densities produced by both permanent magnets and stator currents regardless of Z and p, it is possible to compare different slot-pole combinations in terms of UMP performance by considering the maximum force divided by the stator bore surface A_s.

Appendix B

In this Appendix the analytical procedure [*17*] explained in Paragraph 1.4.3. is validated, with particular reference to an example focused on the comparison between MMF spectra and losses in the magnets, respectively obtained from analytical method and by FEM. In the following table there are the main data of a 13 slots 14 poles machine. The winding structure is described in Table 23 .

Number of slots, Z	13	N turns per slot, N_0	100
Number of pole pairs, p	7	Current (max), I_0	5.5 A
Stator bore radius, R_s	55 mm	Frequency, f	50 Hz
Rotor radius, R_r	48 mm	Magnetic permeability, μ	$4\pi 10^{-7}$ H/m
Magnet height, h_m	4 mm	Magnet conductivity, σ	0.667 MSm
Airgap, g	3 mm	Magnet / pole ratio, c_m	0.95
Axial length, L	100 mm		

Table 22 13 slots 14 poles machine main data

	Tooth index												
	k=0	*k=1*	*k=3*	*k=3*	*k=4*	*k=5*	*k=6*	*k=7*	*k=8*	*k=9*	*k=10*	*k=11*	*k=12*
Phase a+	33	0	0	0	0	0	0	0	0	88	0	100	0
Phase a-	0	0	0	0	0	0	0	0	11	0	100	0	100
Phase b+	0	0	0	0	33	0	100	0	88	0	0	0	0
Phase b-	0	0	0	0	0	100	0	100	0	11	0	0	0
Phase c+	0	100	0	100	0	0	0	0	0	0	0	0	0
Phase c-	67	0	100	0	67	0	0	0	0	0	0	0	0

Table 23 Winding matrix 13 slots 14 poles machine

The following image describes the cross section of the machine.

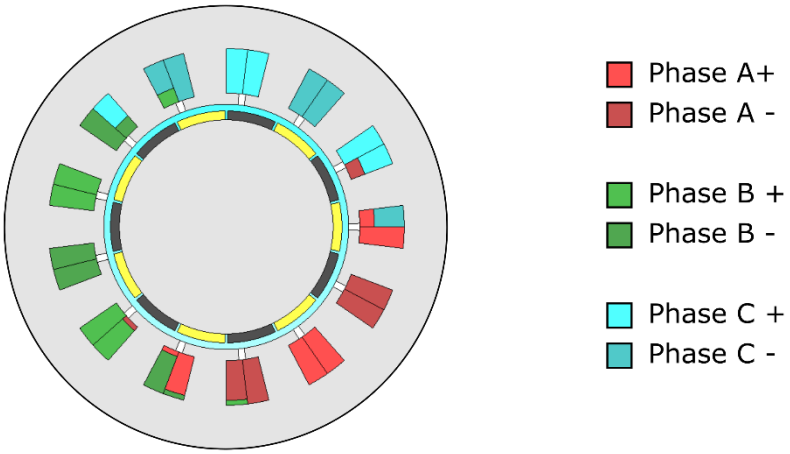

Fig. 56 13 slots 14 poles machines cross section

The waveform of the normal magnetic flux density in the middle of the airgap is represented in the following figure. The red line is extracted from FEM, the green one is the fundamental, the blue one is a sum of harmonics.

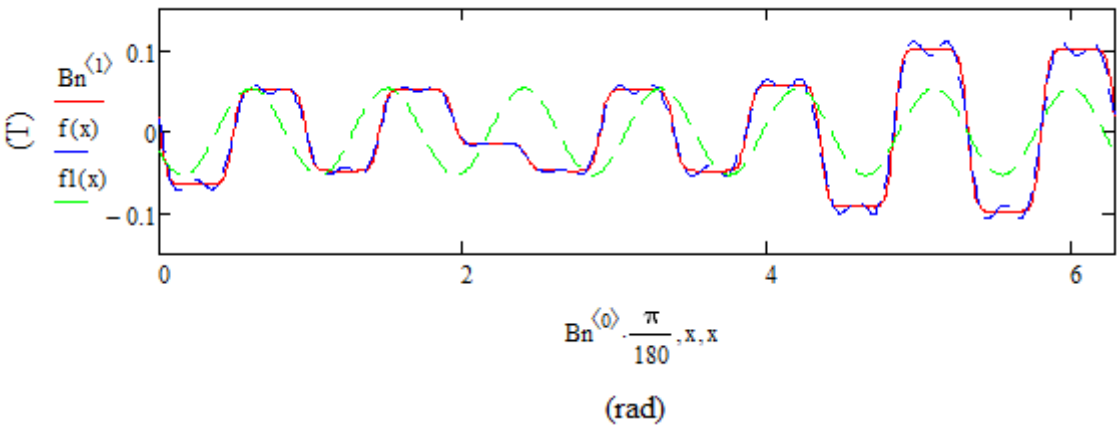

Fig. 57 Normal flux density in the airgap

The coefficients of Fourier series have been compared to the coefficients coming from analytical method (Fig. 58) finding a good accordance.

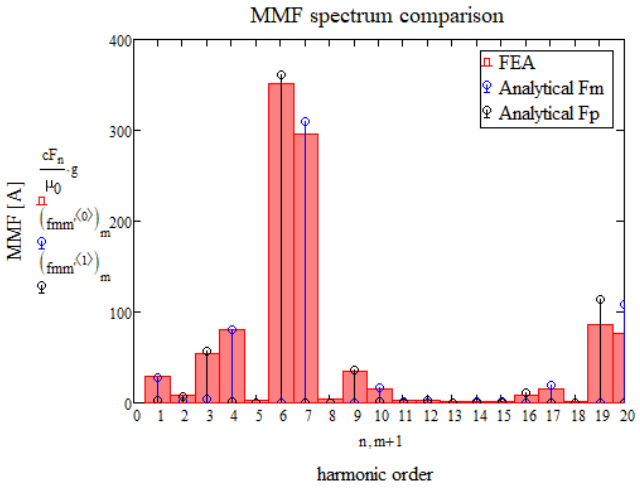

Fig. 58 Fourier spectra comparisons

In order to validate (1-63) it is necessary to compare the values coming from the formula with the values obtained from FEM model (Fig. 59).

The mean value in FEM model is 4.64 W/m while the analytical model gives 4.38 W/m (both results are per unit of machine axial length).

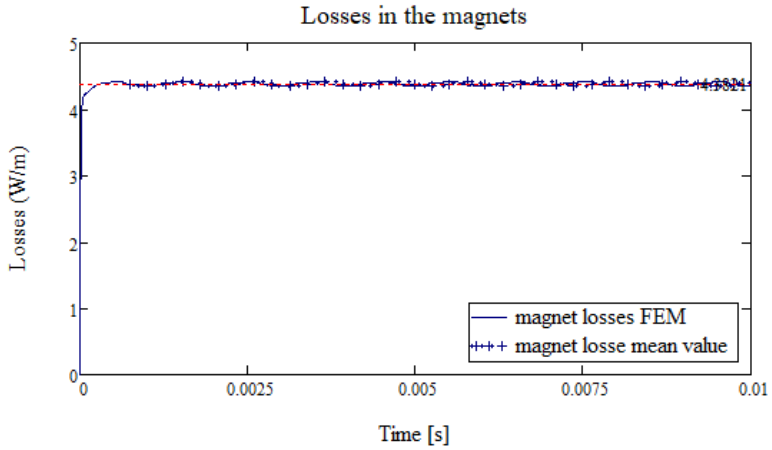

Fig. 59 Losses in the magnets

List of Figures

References

[1] A.M. El-Refaie, Fractional-slot concentrated-windings synchronous permanent magnet machines: Opportunities and challenges, IEEE Trans. Ind., 2010.

[2] A. M. El-Refaie and T. M. Jahns, “Scalability of surface PM Machines with concentrated windings designed to achieve wide speed ranges of constant-power operation,” IEEE Trans. Energy Convers., vol. 21, no. 2,pp. 362–369, Jun. 2006

[3] A. Tessarolo, F. Luise, S. Pieri, A. Benedetti, M. Bortolozzi and M. De Martin, "De-sign for Manufacturability of an Off-Shore Direct Drive Wind Generator: An Insight Into Additional Loss Prediction and Mitigation," IEEE Transactions on Industry

[4] N. Bianchi and E. Fornasiero, “Impact of MMF space harmonic on rotor losses in fractional-slot Permanent-Magnet machines,” IEEE Trans. Energy Convers., vol. 24, no. 2, pp. 323–328, Jun. 2009.

[5] A. Tessarolo, “A survey of state-of-the-art methods to compute rotor eddycurrent losses in synchronous permanent-magnet machines,” in Proc. IEEE Workshop Elect. Mach. Design, Control Diagnosis, Nottingham, United Kingdom, 2017, pp. 12–19.

[6] J.F. Gieras, Electrical Machines: Fundamentals of Electromechanical Energy Conversion, CRC Press, 2016, pp. 402-403.

[7] Y. Yokoi, T. Higuchi and Y. Miyamoto, "General formulation of winding factor for fractional-slot concentrated winding design," IET Electric Power Applications, vol. 10, no. 4, pp. 231-239, April 2016.

[8] S.E. Skaar, O. Krovel, R. Nilssen, "Distribution, coil-span and winding factors for PM machines with concentrated windings," 17th International Conference on Electric Machines, ICEM 2006, Chania, Crete Island, Greece, Sept. 2-5, 2006.

[9] F. Lin, S. Zuo and X. Wu, "Electromagnetic vibration and noise analysis of permanent magnet synchronous motor with different slot-pole combinations," IET Electric Power Applications, vol. 10, no. 9, pp. 900-908, Nov. 2016

[10] Seun Guy Min and B. Sarlioglu, "Investigation of electromagnetic noise on pole and slot number combinations with possible fractional slot concentrated windings," 2017 IEEE Transportation Electrification Conference and Expo (ITEC), Chicago, IL, 2017, pp

[11] M. Valavi, A. Nysveen, R. Nilssen, R. D. Lorenz and T. Rølvåg, "Influence of Pole and Slot Combinations on Magnetic Forces and Vibration in Low-Speed PM Wind Generators," IEEE Transactions on Magnetics, vol. 50, no. 5, pp. 1-11, May 2014

[12] Z. Q. Zhu and D. Howe, "Influence of design parameters on cogging torque in permanent magnet machines," IEEE Transactions on Energy Conversion, vol. 15, no. 4, pp. 407-412, Dec 2000.

[13] L. Zhu, S. Z. Jiang, Z. Q. Zhu and C. C. Chan, "Analytical Methods for Minimizing Cogging Torque in Permanent-Magnet Machines, "IEEE Transactions on Magnetics, vol. 45, no. 4, pp. 2023-2031, April 2009.

[14] S. G. Min and B. Sarlioglu, "Analysis and Comparative Study of Flux Weakening Capability in Fractional-slot Concentrated Windings," IEEE Transactions on Energy Conversion, early access article, DOI 10.1109/TEC.2017.2781718

[15] P. Ponomarev, P. Lindh and J. Pyrhönen, "Effect of Slot-and-Pole Combination on the Leakage Inductance and the Performance of Tooth-Coil Permanent-Magnet Synchronous Machines," IEEE Transactions on Industrial Electronics, vol. 60, no. 10, pp. 4310-4317

[16] L. Alberti and N. Bianchi, "Theory and Design of Fractional-Slot Multilayer Windings," IEEE Transactions on Industry Applications, vol. 49, no. 2, pp. 841-849, March-April 2013

[17] A. Tessarolo, "A Quadratic-Programming Approach to the Design Optimization of Fractional-Slot Concentrated Windings for Surface Permanent-Magnet Machines," IEEE Transactions on Energy Conversion, vol. 33, no. 1, pp. 442-452, March 2018.

[18] A. Tessarolo, C. Ciriani, N. Elloumi and M. Mezzarobba, "Potentials and Limits of Three-Phase Fractional-Slot Concentrated Winding Optimization," 2021 IEEE Workshop on Electrical Machines Design, Control and Diagnosis (WEMDCD), 2021.

[19] A. Tessarolo, C. Ciriani, M. Bortolozzi, M. Mezzarobba and N. Barbini, "Investigation Into Multi-Layer Fractional-Slot Concentrated Windings With Unconventional Slot-Pole Combinations," in IEEE Transactions on Energy Conversion, vol. 34, no. 4, pp. 1985-1996, Dec. 2019.

[20] E. Fornasiero, L. Alberti, N. Bianchi, and S. Bolognani, “Considerations on selecting fractional-slot nonoverlapped coil windings,” IEEE Trans. Ind. Appl., vol. 49, no. 3, pp. 1316–1324, May/Jun. 2013

[21] C. M. Spargo, B. C. Mecrow, J. D. Widmer, C. Morton, and N. J.Baker, “Design and validation of a synchronous reluctance motor with single tooth windings,” IEEE Trans. Energy Convers., vol. 30, no. 2, pp. 795–805, Jun. 2015

[22] A. S. Abdel-Khalik, S. Ahmed, and A. M. Massoud, “Low space harmonics cancelation in Double-Layer fractional slot winding using dual multiphase winding,” IEEE Trans. Magn., vol. 51, no. 5, May 2015, Art. no. 8104710

[23] Y. Wang, R. Qu, and J. Li, “Multilayer windings effect on interior PMmachines for EV applications,” in IEEE Trans. Ind. Appl., vol. 51, no. 3, pp. 2208–2215, May/Jun. 2015.

[24] A. Sun, J. Li, R. Qu, and D. Li, “Effect of multilayer windings on rotor losses of interior permanent magnet generator with Fractional-Slot Concentrated-Windings,” IEEE Trans. Magn., vol. 50, no. 11, Nov. 2014, Art. no. 8105404.

[25] Y. Wang, R. Qu, and J. Li, “Multilayer windings effect on interior PM machines for EV applications,” in IEEE Trans. Ind. Appl., vol. 51, no. 3, pp. 2208–2215, May/Jun. 2015.

[26] D. Gerlando, A. Perini, and M. R. Ubaldini, “High pole number, PM synchronous motors with concentrated coil armature winding,” in Proc. Int. Conf. Electr. Mach., Krakow, Poland, 2004, pp. 307–320.

[27] M. V. Cistelecan, F. J. T. E. Ferreira, and M. Popescu, “Three phasetooth concentrated multiple-layer fractional windings with low space harmonic content,” in Proc. IEEE Energy Convers. Congr. Expo., 2010,pp. 1399–1405.

[28] L. Alberti, M. Barcaro, and N. Bianchi, “Design of a Low-Torque-ripple fractional-slot interior permanent-magnet motor,” IEEE Trans. Ind. Appl.,vol. 50, no. 3, pp. 1801–1808, May/Jun. 2014.

[29] A. Tessarolo, M. Mezzarobba, and N. Barbini, “Improved four-layer winding design for a 12-slot 10-pole permanent magnet machine using unequal tooth coils,” in Proc. IEEE IECON 2016 - 42nd Annual Conf. Ind. Electron. Soc., Florence, 2016, pp. 1686–1691.

[30] T.F. Coleman and Y. Li, “A reflective newton method for minimizing a quadratic function subject to bounds on some of the variables,” SIAM J. Optimization, vol. 6, no. 4, pp. 1040–1058, 1996

[31] F. Luise, S. Pieri, M. Mezzarobba, and A. Tessarolo, “Regenerative testing of a Concentrated-Winding Permanent-Magnet synchronous machine for offshore wind generation—Part I: Test concept and analysis,” IEEE Trans. Ind. Appl., vol. 48, no. 6, pp. 1779–1790, Nov./Dec. 2012

[32] M. Olivo, A. Tessarolo, and M. Bortolozzi, “On the use of conformai mapping in the analysis of electric machines,” in Proc. 2016 XXII Int.Conf. Elect. Mach., Lausanne, 2016, pp. 492–498.

[33] P. Arumugam, T. Hamiti, and C. Gerada, “Estimation of eddy current loss in Semi-Closed slot vertical conductor permanent magnet synchronous machines considering eddy current reaction effect,” IEEE Trans. Magn., vol. 49, no. 10, pp. 5326–5335, Oct. 2013

[34] N. Bianchi, S. Bolognani, and E. Fornasiero, “An overview of rotor losses determination in Three-Phase Fractional-Slot PM machines,” IEEE Trans. Ind. Appl., vol. 46, no. 6, pp. 2338–2345, Nov./Dec. 2010

[35] A. M. Silva, F. J. T. E. Ferreira, M. V. Cistelecan, and C. H. Antunes, "Multiobjective design optimization of generalized multilayer multiphase ac winding," IEEE Transactions on Energy Conversion, vol. 34, no. 4, pp. 2158–2167, 2019

[36] R. F. Burbidge, "A rapid method of analysing the m.m.f. wave of a single or polyphase winding," Proceedings of the IEE - Part C: Monographs, vol. 105, no. 7, pp. 307-311, March 1958.

[37] S. Stipetic, D. Zarko and M. Popescu, "Ultra-fast axial and radial scaling of synchronous permanent magnet machines," IET Electric Power Applications, vol. 10, no. 7, pp. 658-666, 8 2016.

[38] Z. Q. Zhu, D. Ishak, D. Howe and J. Chen, "Unbalanced Magnetic Forces in Permanent-Magnet Brushless Machines With Diametrically Asymmetric Phase Windings," IEEE Transactions on
Industry Applications, vol. 43, no. 6, pp. 1544-1553, Nov.-dec.2007.

[39] G. H. Jang, J. W. Yoon, N. Y. Park and S. M. Jang, "Torque and unbalanced magnetic force in a rotational unsymmetric brushless DC motors," IEEE Transactions on Magnetics, vol. 32, no. 5, pp. 5157-5159, Sept. 1996